

# **A Molecular Dynamics Study of Material Behavior Controlled by Interface**

*by*

Lifeng Ding (MRes)

Department of Engineering

University of Leicester

Leicester, UK

Thesis submitted for the degree of Doctor of Philosophy in August 2010

## Abstract

In this work, the behaviour of nano-structured materials that is controlled by the interface is studied using Molecular Dynamics (MD). Four different types of nano-structured materials were investigated: (1) the sintering behaviour of nanoparticle; (2) the evolution of bamboo-like nanowires; (3) the mechanical property of the interlamellar phase of semicrystalline polymers; and (4) the mechanical property of the interlamellar phase of biodegradable polymers.

In the MD simulation of nanoparticle sintering, it is observed that the particles can reorient themselves to match their crystalline orientations at the beginning of the sintering and thereby form different types of necks between different particles. This leads to different mechanisms of matter redistribution at the different necks. It has also been observed that the particles switch the mechanism of matter transportation halfway through the sintering process. None of these can be handled by the continuum model. However, assuming the right scenario, the continuum theory does agree with the MD simulation for particles consisting of just a few thousand atoms.

In the multi-scale MD simulation of the evolution of bamboo-like nanowires, the microstructure evolution behaviour of the bamboo nanowire is observed very different to the conventional bamboo structure polycrystals. When the materials reduce to the nano-size, different evolution behaviour occurs: the low angle tilt grain boundary (GB) tends to be eliminated by forming a bending crystal form and dislocation slip might occur when raise the temperature; the large tilt GB is found stable at low temperature but the GB diffusion is very sensitive to the temperature; An interesting microstructure evolution behaviour of the nanowire with the small radius starting with the large angle GB is observed. A new hcp grain is nucleated from the triple point of the bamboo structure.

In the multi-scale MD study of the mechanical property of the interlamellar phase of semicrystalline biodegradable polymers, it is found that the mechanical stiffness of interlamellar phase below  $T_g$  is mainly governed by the LJ interaction along the polymer backbone. Therefore, good polymer chain entanglement enhances the LJ interaction and increases the mechanical strength. Although the amorphous interlamellar phase is not the idea elastomer when temperature is above the glass transition temperature, it also shows the elastomer behaviour above  $T_g$  when we examine the number of long chains inside the amorphous interlamellar phase. The results of this study further support Pan's entropy spring theory by showing the Young's modulus drop lags behind the biodegradation process at temperatures above the glass transition temperature. For the amorphous interlamellar phase below the glass transition temperature, the Young's modulus drops quickly as the chain scissions quickly reduce the polymer chain entanglement.

## **Acknowledgements**

It is a pleasure to thank the many people who made this thesis possible.

In particular, I wish to express my gratitude to my supervisors Professor Jingzhe Pan and Dr Ruslan L. Davidchack for their continued guidance, encouragement and the great efforts to explain things clearly and simply throughout the course of this research. They have let me know the joy and fun of learning and researching. I would also like to thank Dr Simon Gill for his invaluable advice.

I also wish to express my acknowledgement to EPSRC funding (Grant S97996) for the first two year of my PhD studentship and University of Leicester PhD studentship for the last year of my PhD study. I am also grateful to my colleagues in the mechanics of materials group for their generous support and friendship.

Last, but most importantly I wish to thank my parents and my fiancée for their support and love.

## Contents

<b>Chapter 1 Overarching Introduction.....</b>	<b>- 1 -</b>
<b>Chapter 2 Molecular Dynamics (MD) Study of Nanoparticles Sintering.....</b>	<b>- 5 -</b>
2.1 Sintering of nanoparticles .....	- 5 -
2.2 Purpose of MD modelling of nanoparticle interaction.....	- 6 -
2.3 An overview of conventional solid-state sintering.....	- 7 -
2.3.1 The driving force for sintering .....	- 7 -
2.3.2 The sintering stages.....	- 10 -
2.3.3 Sintering mass transport mechanisms .....	- 13 -
2.4 Computer Simulation of Sintering Using Molecular Dynamics .....	- 18 -
2.4.1 The fundamentals of Molecular Dynamics simulation .....	- 18 -
2.4.2 Leap frog integration.....	- 20 -
2.4.3 Reduced units .....	- 21 -
2.4.4 Boundary conditions .....	- 22 -
2.5 MD simulation of 2D nanoparticle interactions .....	- 23 -
2.5.1 The models of nanoparticle interaction .....	- 23 -
2.5.2 Subtraction of the rigid motion of the entire system.....	- 26 -
2.5.3 Neck size and centre-to-centre distance .....	- 27 -
2.6 Results and discussion.....	- 28 -
2.6.1 Volume fraction of atoms at the particle surface .....	- 28 -
2.6.2 Effect of the crystalline orientation of the particles .....	- 30 -
2.6.3 Sintering particles.....	- 34 -
2.7 Conclusions .....	- 42 -
<b>Chapter 3 Computer Simulation of Nanoparticle Sintering Using a 2D Continuum Method .....</b>	<b>- 44 -</b>
3.1 Introduction to the continuum model.....	- 44 -
3.2 A Finite difference model for sintering.....	- 45 -
3.3 A Finite difference method scheme for sintering.....	- 52 -
3.4 Coupling between surface and boundary diffusion.....	- 54 -
3.5 Updating the profile of the particle .....	- 56 -
3.6 Results and discussion.....	- 57 -
3.7 Comparison between MD and continuum simulations for 2D nanoparticle sintering ...	- 59 -

3.8	Conclusions of the study of nanoparticle sintering .....	- 62 -
<b>Chapter 4 Multi-scale MD Simulations of Behaviour of Bamboo-like Nanowires at Elevated Temperatures.....- 63 -</b>		
4.1	Introduction to Nanowires.....	- 63 -
4.2	Understanding the evolution of conventional bamboo-like polycrystalline fibres via the continuum model.....	- 64 -
4.3	A Multi-scale MD scheme .....	- 68 -
4.3.1	The details of the multi-scale MD scheme .....	- 70 -
4.4	Modelling bamboo-like nanowires.....	- 74 -
4.5	The potential energy distribution and potential reduction .....	- 77 -
4.6	Computer simulation results and discussions.....	- 79 -
4.6.1	Elimination of small angle tilt GBs.....	- 79 -
4.6.2	Formation of the stable large angle tilt GB .....	- 82 -
4.6.3	Temperature effect .....	- 85 -
4.6.4	Size effect.....	- 88 -
4.7	Conclusions .....	- 94 -
<b>Chapter 5 A MD Study of the Mechanical Behaviour of Semi-crystalline Polymers.....- 96 -</b>		
5.1	Introduction to semicrystalline polymers .....	- 96 -
5.1.1	The structure of crystal lamellars .....	- 98 -
5.1.2	The nature of the interlamellar phase .....	- 100 -
5.2	Glass transition temperature and mechanical properties of polymers.....	- 103 -
5.3	The thermodynamics of the deformation of amorphous polymers .....	- 105 -
5.4	Molecular dynamics simulation of the semicrystalline polymers .....	- 111 -
5.4.1	The force field.....	- 111 -
5.4.2	Coupling between the rigid crystal lamellar and flexible atomistic interlamellar phase at a constant temperature.....	- 114 -
5.4.3	Neighbour list.....	- 115 -
5.4.4	Boundary conditions .....	- 116 -
5.4.5	Generation of the initial semicrystalline polymer structure .....	- 119 -
5.4.6	Computer simulation results for interlamellar phase amorphization .....	- 125 -
5.5	Mechanical properties of the interlamellar phase in semicrystalline polymers .....	- 132 -
5.5.1	Deformation in the MD model .....	- 132 -
5.5.2	Determination of the glass transition temperature .....	- 135 -
5.5.3	Mechanical properties of semicrystalline polymers under $T_g$ .....	- 137 -
5.5.4	The mechanical property of semicrystalline polymers above $T_g$ .....	- 145 -

5.5.5	Mechanical deformation tests of the crystal lamellars using MD .....	- 147 -
5.6	Conclusions .....	- 149 -
<b>Chapter 6 A Molecular Model for Mechanical Behaviour of a Degrading Polymer Undergoing Chain Cleavage.....</b>		<b>- 151 -</b>
6.1	Introduction to semicrystalline biodegradable polymers .....	- 151 -
6.2	A molecular model for the mechanical behaviour of a degrading polymer .....	- 155 -
6.3	Results and discussions .....	- 160 -
6.3.1	Morphology change in the interlamellar phase during degradation .....	- 160 -
6.3.2	Mass loss .....	- 162 -
6.3.3	Mechanical property change of interlamellar region during degradation above $T_g$ ...	- 164 -
6.3.4	Mechanical property change of interlamellar region during degradation below $T_g$	- 167 -
6.4	Conclusions .....	- 169 -
<b>Chapter 7 Conclusions.....</b>		<b>- 170 -</b>
<b>Appendix .....</b>		<b>- 177 -</b>
Appendix A - End-bridging (EB) MC move algorithm .....		- 178 -
Appendix B - End-reptation (EP) algorithm .....		- 188 -
Appendix C – Linear regression method .....		- 190 -

## Figures list.

Figure 2.1 Figure 2.1 Sphere and plate as a basis for examining the energy difference associated with a curved surface. ....	8 -
Figure 2.2 Figure 2.2 Two-sphere model used for initial stage sintering for (a) non-densifying mechanisms and (b) densifying mechanisms. $r$ and $X$ are the principle radii of the curvature of the neck surface, $R$ is the radius of the sphere[6].....	11 -
Figure 2.3 The tetrakaidecahedron model used in intermediate stage sintering[9].....	12 -
Figure 2.4 The middle velocity used in the leap frog method.....	<b>Error! Bookmark not defined.</b>
Figure 2.5 The initial configuration of the MD model of three particles in contact with each other. ....	24 -
Figure 2.6 The three different configurations of particles: I, two particles of different sizes; II, two same sized particles; III, one small particle in the middle of two larger particles. ....	25 -
Figure 2.7 Mathematical subtraction of rigid rotation during post processing. ....	26 -
Figure 2.8 Number of atoms as a function of their potential energy, indicating their locations at different parts of the particle during sintering.....	28 -
Figure 2.9 Volume fraction of surface atoms as a function of sintering time. ....	30 -
Figure 2.10 Particles with initially aligned crystal orientations maintain their alignment during sintering; only half of the particles are shown to reveal their relative rotation. ....	32 -
Figure 2.11 Particles with initially misaligned crystal orientations. The small particle reorients itself at the very beginning of the sintering process; only half of the particles are shown to reveal their relative rotation. ....	32 -
Figure 2.12 Two nanoparticles sinter together to form a single crystal; the red lines mark the crystalline orientations before and after the reorientation. ....	33 -
Figure 2.13 Two nanoparticles sinter together to form a GB; the red lines mark the crystalline orientations before and after the reorientation. ....	33 -
Figure 2.14 MD simulation of one small and two large particles sintering at $T = 0.26 \epsilon/k_B$ . (a) $t = 500t^*$ ; (b) $t = 50000t^*$ ; (c) $t = 200000t^*$ ; (d) $t = 500000t^*$ . See text for the explanation of the colour scheme. ....	36 -
Figure 2.15 MD simulation of a small and a large particle sintering at $T = 0.26 \epsilon/k_B$ . (a) $t = 500t^*$ ; (b) $t = 50000t^*$ ; (c) $t = 200000t^*$ ; (d) $t = 500000t^*$ . See text for the explanation of the colour scheme. ....	36 -

Figure 2.16 MD simulation of two large particles sintering at  $T = 0.26 \epsilon/k_B$ . (a)  $t = 500t^*$ ; (b)  $t = 50000t^*$ ; (c)  $t = 200000t^*$ ; (d)  $t = 500000t^*$ . See text for the explanation of the colour scheme. ... - 37 -

Figure 2.17 MD simulation of one small and two large particles sintering at  $T = 0.19 \epsilon/k_B$ . (a)  $t = 500t^*$ ; (b)  $t = 50000t^*$ ; (c)  $t = 200000t^*$ ; (d)  $t = 500000t^*$ . See text for the explanation of the colour scheme. .... - 38 -

Figure 2.18 MD simulation of a small and a large particle sintering at  $T = 0.19 \epsilon/k_B$ . (a)  $t = 500t^*$ ; (b)  $t = 50000t^*$ ; (c)  $t = 200000t^*$ ; (d)  $t = 500000t^*$ . See text for the explanation of the colour scheme. .... - 38 -

Figure 2.19 MD simulation of two large particles sintering at  $T = 0.19 \epsilon/k_B$ . (a)  $t = 500t^*$ ; (b)  $t = 50000t^*$ ; (c)  $t = 200000t^*$ ; (d)  $t = 500000t^*$ . See text for the explanation of the colour scheme. ... - 39 -

Figure 2.20 MD simulation of two large particles sintering with the GB at  $T = 0.26 \epsilon/k_B$ . (a)  $t = 500t^*$ ; (b)  $t = 50000t^*$ ; (c)  $t = 200000t^*$ ; (d)  $t = 500000t^*$ . See text for the explanation of the colour scheme. .... - 40 -

Figure 2.21 Centre-to-centre distance as a function of time for the case shown in Figure 18. .... - 40 -

Figure 2.22 Comparison of neck size growth as a function of time for the cases shown in Figures 2.16, 2.19 and 2.20. .... - 41 -

Figure 2.23 MD simulation of one small and two large particles sintering at  $T = 0.26 \epsilon/k_B$ . (a)  $t = 500t^*$ ; (b)  $t = 50000t^*$ ; (c)  $t = 200000t^*$ ; (d)  $t = 500000t^*$ . See text for the explanation of the colour scheme. .... - 42 -

Figure 3.1 The two-dimensional coupled diffusion model for two particles sintering ..... - 46 -

Figure 3.2 Diffusion fluxes and surface and GB tension equilibrium in the 2D coupled diffusion model of two-particle sintering. .... - 49 -

Figure 3.3 Initial configuration of finite difference model of two particles sintering..... - 53 -

Figure 3.4 Coupling between surface diffusion and GB diffusion..... - 55 -

Figure 3.5 Sintering of two identical particles dominated by GB diffusion. .... - 58 -

Figure 3.6 Sintering of two identical particles dominated by surface diffusion. .... - 59 -

Figure 3.7 Neck size divided by initial particle radius as a function of time predicted by the MD model (discrete dots) and continuum model (solid line) for the sintering of two particles of the same size, each consisting of 5000 atoms at  $T = 0.19\epsilon/k_B$ . Surface diffusion is the dominant mechanism for matter redistribution. Logarithmic scales are used for both axes. .... - 61 -

Figure 3.8 Neck size divided by initial particle radius as a function of time predicted by the MD model (discrete dots) and continuum model (solid line) for the sintering of two particles of the same size, each consisting of 5000 atoms, at  $T = 0.26\epsilon/k_B$ . Grain-boundary diffusion is the dominant mechanism for matter redistribution. Logarithmic scales are used for both axes. .... - 61 -

Figure 4.1 (a) The initial array of cylinder-shaped grains. (b) An array of barrel-shaped grains approximates an intermediate, non-equilibrium state. (c) Grains pinch off and spheroidise, approaching an equilibrium state, a row of isolated spheres. (d) The array shrinks as atoms

diffuse out from the GBs and plate onto the free surfaces, approaching another equilibrium state, a touching array of truncated spheres. Taken from Suo[31]. ..... - 64 -

Figure 4.2 Energy landscape. The free energy is a function of the generalised coordinates, represented as a surface in the thermodynamic space. A point on the surface represents a state, generally not in equilibrium. Three special states are indicated on the surface: the initial cylinders, isolated spheres and truncated spheres. Taken from Suo[31]. ..... - 66 -

Figure 4.3 The solid lines are the energy contours and the dotted lines are the evolution path when the grains are connected. The dashed line is the evolution path after the grains pinch off. Taken from Suo[31]. ..... - 67 -

Figure 4.4 The initial configuration of the MD model of the bamboo-like nanowire. .... - 71 -

Figure 4.5 Schematic of the finite temperature dynamic coupled atomistic/continuum simulation model for a single grain, which is the upper half of a bamboo model. The lower half is symmetrical to this one. .... - 74 -

Figure 4.6 Four different models of bamboo-like nanowires. .... - 76 -

Figure 4.7 The z-x and z-y planes of the nanowire column. .... - 77 -

Figure 4.8 The colouring method of surface boundary, GB and bulk atoms based on their potential energy differences. .... - 78 -

Figure 4.9 Initial reorientation of two free bamboo grains (with no fixed top and bottom continuum regions): (a) represents the nanowire structure at time  $t = 100t^*$ ; (b) represents the nanowire structure at time  $t = 500t^*$ ; (c) represents the nanowire structure at time  $t = 1000t^*$ . .... - 79 -

Figure 4.10 The initial low angle GB is eliminated by forming a stable bending structure without any defects for model I at low temperatures: (a) represents the nanowire structure at time  $t = 100t^*$ ; (b) represents the nanowire structure at time  $t = 1000t^*$ . .... - 80 -

Figure 4.11 The dislocation wall in the conventional low angle tilt GB. .... - 81 -

Figure 4.12 The formation of the stable large angle tilt GB for model III at low temperatures. .... - 82 -

Figure 4.13 The average potential energy and bulk length in the z-direction as a function of evolution time for model III under low temperatures. .... - 83 -

Figure 4.14 The neck size evolution as a function of evolution time for model III under low temperatures. .... - 84 -

Figure 4.15 Multiple dislocation slip plane was found in model I under high temperatures: (a) represents the nanowire structure at time  $t = 100t^*$ ; (b) represents the nanowire structure at time  $t = 10000t^*$ ; (c) represents the nanowire structure at time  $t = 30000t^*$ . .... - 86 -

Figure 4.16 Average potential energy and bulk length in the z-direction as a function of evolution time for model I under high temperatures. .... - 86 -

Figure 4.17 The apparent grain growth and GB migration were found using model III under high temperatures: (a) represents the nanowire structure at time  $t = 100t^*$ ; (b) represents the nanowire structure at time  $t = 10000t^*$ ; (c) represents the nanowire structure at time  $t = 30000t^*$ . - 87 -

Figure 4.18 The comparison of bulk length shrinkage in the z-direction for model III between low and high temperatures. The green crossed line represents the length shrinkage under low temperatures. The blue triangle line represents the length shrinkage under high temperatures..... - 87 -

Figure 4.19 Multiple dislocation slip plane was found in model II under high temperatures: (a) represents the nanowire structure at time  $t = 100t^*$ ; (b) represents the nanowire structure at time  $t = 10000t^*$ ; (c) represents the nanowire structure at time  $t = 30000t^*$ . ..... - 89 -

Figure 4.20 The comparison of bulk length shrinkage in the z-direction between models I and II under high temperatures. The blue crossed line represents the length shrinkage of model I. The green triangle line represents the length shrinkage of model II. .... - 89 -

Figure 4.21 One new hcp(hexagonal close-packed) grain was found growing from the triple point in model IV under low temperatures: (a) represents the nanowire structure at time  $t = 100t^*$ ; (b) represents the nanowire structure at time  $t = 10000t^*$ ; (c) represents the nanowire structure at time  $t = 30000t^*$ . ..... - 90 -

Figure 4.22 Three hexagonal planes (used to be  $\langle 111 \rangle$  at the fcc crystal) sitting on top of each other were plotted with star, diamond and circle shapes (layers A, B and C) from the positions of the newly formed grains. Layer A is obviously overlapped with layer C, which proves that this new grain is an hcp crystal structure. .... - 91 -

Figure 4.23 The average potential energy and bulk length in the z-direction as a function of evolution time for model IV under low temperatures. .... - 91 -

Figure 4.24 Apart from the apparent grain growth and GB migration found in model IV under high temperatures, the dislocation slip is also observed: (a) represents the nanowire structure at time  $t = 100t^*$ ; (b) represents the nanowire structure at time  $t = 10000t^*$ ; (c) represents the nanowire structure at time  $t = 30000t^*$ . .... - 93 -

Figure 4.25 The comparison of bulk length shrinkage in the z-direction between models III and IV under high temperatures. The blue crossed line represents the length shrinkage of model III. The green triangle line represents the length shrinkage of model IV. .... - 94 -

Figure 5.1 Spherulitic structure in a semicrystalline polymer as observed under an optical polarising microscope: single spherulite (left) and spherulitic impingement (right). Taken from[41] ..... - 98 -

Figure 5.2 Schematic representation of the structure of polymer spherulites. The branches of the spherulites are made of crystal lamellar stacks and all the lamellars are connected via interlamellar amorphous polymers. Taken from [41] ..... - 98 -

Figure 5.3 Structure of polyethylene crystal, showing the position of the chain in the unit cell. (a) Side view. (b) Projection along the direction of the chain axes [45]. .... - 99 -

Figure 5.4 An illustration of the crystal lamellar and the interlamellar amorphous region in semicrystalline polymers. The conformations of chains are shown: (a) bridges; (b) chain ends; (c) loose chain folds and (d) tight chain folds. .... - 100 -

Figure 5.5 The effect of temperature on the total volume of a polymer. Taken from[58] ..... - 104 -

Figure 5.6 A single polymer chain, ..... - 107 -

Figure 5.7 Entropy change of a single chain as the polymer deforms. .... - 107 -

Figure 5.8 The MD configuration of interlamellar phase. .... - 115 -

Figure 5.9 The neighbour list method used in a polymer chain. .... - 115 -

Figure 5.10 A schematic illustration of PBCs, which explains that the polymer chain can leave the left boundary and re-enter from the right boundary (solid lines are the polymer chains in the predefined MD cell and dashed lines are the polymer chains in its adjacent image cells). .... - 117 -

Figure 5.11 The construction of the amorphous interlamellar using the MC method. .... - 120 -

Figure 5.12 End-bridging MC move (a three-atom segment of a bridge or loop chain is excised by cutting the two bonds connecting them, and then reconfigured to connect another nearby tail branch by creating two new bonds). .... - 122 -

Figure 5.13 End-reptation move (one chain end bead  $m$  is excised from chain 1 and joined to another chain end, chain 2). .... - 124 -

Figure 5.14 The atomistic picture of the semicrystalline polymer interlamellar domain (the amorphous chains between two small polymer crystal lamellars). .... - 126 -

Figure 5.15 One bridge chain starts from one crystal, passes through the amorphous region and ends in another crystal..... - 127 -

Figure 5.16 One tight loop starts from one crystal and immediately folds back to the same crystal..... - 127 -

Figure 5.17 One loose loop starts from one polymer crystal, passes through the amorphous interlamellar domain and folds back to the original polymer crystal..... - 128 -

Figure 5.18 One chain tail starts from one polymer crystal, goes into the amorphous interlamellar domain before the chain ends in the amorphous region. .... - 128 -

Figure 5.19 Chain length distribution map in the amorphous interlamellar region. .... - 129 -

Figure 5.20 Density distribution profile along the Z axis at T = 300K..... - 131 -

Figure 5.21 Bond orientation Order parameter distribution profile along the Z axis at T = 300K - 132 -

Figure 5.22 Schematic details of Molecular Dynamics modelling of tensile pulling test of semi-crystalline polymer..... - 134 -

Figure 5.23 The stress in the interlamellar region as a function of the strain applied to it by the pulling deformation. The straight red line is calculated using linear regression. Its slope determines Young's modulus of the interlamellar region. .... - 134 -

Figure 5.24 Young's modulus and volume change of semicrystalline polymer as a function of the temperature..... - 137 -

Figure 5.25 Kinetic and potential energy change during the tensile pulling simulation at temperature T = 300 K which is below the estimated glass transition temperature  $T_g$  ..... - 139 -

Figure 5.26 Kinetic and potential energy change during the tensile pulling simulation at temperature  $T = 390$  K, which is above  $T_g$ ..... - 139 -

Figure 5.27 Separate contributions of different interatomic potentials to the total potential energy change during the tensile pulling test of the interlamellar region at  $T = 300$ K..... - 140 -

Figure 5.28 The interlamellar density of semicrystalline polymers as a function of the chain ends density (the solid line is presented as a guide line)..... - 141 -

Figure 5.29 Young's modulus of semicrystalline polymers as a function of the interlamellar density under  $T_g$ . .... - 142 -

Figure 5.30 A schematic illustration of the entanglement of chains within the interlamellar region. The chains connected to the top lamella ("top chains") are coloured blue, while the remaining chains are coloured black. The number of LJ bonds is counted between the top chains and the remaining chains ..... - 143 -

Figure 5.31 Young's modulus of interlamellar phase as a function of the density of LJ bonds between top chain beads and the rest of chain beads at  $T = 300$ K. Different symbols represent results for systems with different sizes,  $d$ , of the interlamellar region: circles for  $d = 10$  nm, squares for  $d = 8$  nm and triangles for  $d = 6$  nm. .... - 145 -

Figure 5.32 Chain length distribution (including all types of chains: loops, bridges, and tails). Chains in the interval  $a$  are recognized as short, while chains in the interval  $b$  are recognized as long. The temperature of the system is  $T = 390$ K..... - 146 -

Figure 5.33 Young's modulus of the interlamellar region as a function of the number of long chains per unit volume at  $T = 390$  K, which is above the glass transition temperature..... - 147 -

Figure 5.34 Separate contributions of different interatomic potentials to the total potential energy change during the tensile pulling test of the a crystal lamella at  $T = 300$ K ..... - 148 -

Figure 5.35 Young's modulus of crystal lamellae as a function of the number of crystal chains at temperature  $T = 300$ K. The crystal thickness is  $d = 10$  nm. .... - 149 -

Figure 6.1 Schematic demonstration of the entropy spring model showing an initially intact polymer chain embedded in many other polymer chains, which are represented by the shaded background. (a) The entropy of the polymer chains is reduced during deformation as the long molecules become more ordered, giving an elastic resistance to the deformation. (b) Neither an isolated cleavage nor very short chains affect the entropy resistance to deformation. (c) Sufficient chain cleavages break down the polymer chain, which no longer contributes entropy resistance to deformation [85]..... - 155 -

Figure 6.2 shows that both PE and PGA chains have zig-zag formation, and both of them could be simplified into a very similar zig-zag structure of united atom model, if we consider the C=O group in the PGA and the CH<sub>2</sub> group in the PGA and PE as a single "united atom"..... - 156 -

Figure 6.3 The atomistic picture of the semicrystalline polymer interlamellar domain (the amorphous chains between two small polymer crystals). .... - 157 -

Figure 6.4 Random chain scission is carried out by removing a three-bead segment..... - 159 -

Figure 6.5 The interlamellar chain composition at nine different degradation stages. Stages are numbered from 1 to 9, with larger numbers corresponding to larger degrees of polymer degradation at  $T = 390\text{K}$ . ..... - 162 -

Figure 6.6 Mass loss during polymer degradation. .... - 163 -

Figure 6.7 Thickness change of the interlamellar space as a function of the degradation process. - 163 -

Figure 6.8 Young's modulus of biodegradable polymer as a function of the number of chain scissions at  $T = 390\text{K}$ : (a) the interlamellar thickness  $d = 6\text{ nm}$ . (b) the interlamellar thickness  $d = 8\text{nm}$ . ..... - 166 -

Figure 6.9 One long polymer chain embedded inside the interlamellar phase after it degraded into two new chains (all other chains are represented by shadow area, Those small chain fragments is connected with the same colour chain, this happens because of the PBC condition.) Two newly generated chain ends (inside the yellow circles) still stay close to each other after 5 ns equilibration process..... - 166 -

Figure 6.10 Young's modulus of biodegradable polymer with the interlamellar thickness  $d = 8\text{ nm}$  as a function of the number of chain scissions at temperature  $T = 300\text{K}$  which is below the glass transition temperature..... - 168 -

## Nomenclature

$A$	Area
$D$	Diffusivity
$d$	Distance
$F$	Vector force acting on the particles
$f$	Force
GB	Grain boundary
$G$	Free energy
$H$	Hamiltonian of the system
$h$	The MD time step
$j$	Flux
$K$	The kinetic energy of the system
$k$	Boltzmann's constant or curvature
LJ	Lenard Jones Potential
$m$	Mass
$M_b$	GB diffusion mobility
MC	Monte Carlo
MD	Molecular Dynamics simulation
$M_s$	The surface diffusion mobility
$n$	Number of atoms
$P$	Pressure
PE	polyethylene
PGA	poly(glycolic acid)
PLA	poly (lactic acid)

$r$	Position of atoms or the distance between atoms
$r_c$	The LJ cut-off limit distance
$s$	Local coordinate along the diffusion path
$t$	Time
$T$	Temperature
$T_g$	Glass transition temperature
$T_m$	Melting temperature
$U$	Potential energy
$V$	Volume
$v$	Velocity
$W$	The Wall potential used in multi-scale model
$\varepsilon$	The unit energy of MD simulation
$\mu$	Chemical potential
$\sigma$	Stress or the equilibrium length of the LJ interaction
$\Omega$	Atomic volume

## **Chapter 1      Overarching Introduction**

Nanostructured materials can be designed to exhibit novel and significantly improved physical and chemical phenomena and processes due to increase in surface-to-volume ratio. The properties of condensed phases at the nano-scale are rather different from those of more coarse-grained materials. The interfaces existing inside the nano-scale materials play an important role that makes these nano-scale materials different. For example, the Hall–Petch effect states that an excessive amount of grain boundaries (GBs) in nanostructured materials could impede the dislocation propagation. The interfaces usually act as a boundary that separates as well as connects two different crystals or phases. In polycrystalline solids, GB and surface boundary are common interfaces. In crystalline polymers, the amorphous interlamellar phases between polymer crystals are the interfaces. Most of the time, the mechanical properties of nanostructures are governed by the interfaces rather than bulk crystal materials. Therefore, understanding the behaviour of interfaces is the key factor for developing and using novel nanostructured materials.

Most theories of material behaviour are based on macroscopic experimental evidence or conventional mathematical models. Although experimental observations and conventional models are of great importance, it is highly desirable to develop models that can accurately describe a material at the nano-scale level. As computational capability and resources have increased, the molecular dynamics (MD) simulation has become a powerful tool in the field of nanomechanics. By modelling each molecule of a nanostructured material, the understanding of behaviour and structure–property relationships of the nanostructured material can be obtained.

The purpose of this research is to develop atomistic simulation models to investigate the behaviour and effect of interfaces in nanostructured materials. The codes of atomistic simulation were developed mainly based on the book *The Art of Molecular Dynamics Simulation*. [1] There are four main objectives to this thesis: (1) to investigate nanoparticle sintering evolution behaviour; (2) to investigate the behaviour of bamboo-like nanowire at elevated temperatures; (3) to study the mechanical property of the interlamellar phase of semicrystalline polymers; and (4) to study the mechanical property of the interlamellar phase of biodegradable polymers. All of these behaviours on properties are controlled by the interface within the materials. Molecular dynamics simulation is the methodology that is adopted in this work to study the interface controlled behaviour and properties. However the origins and the literature context of these problems are very different. For example, the Sintering is mostly relevant to the processing of ceramics while the degradation of polymers belongs to the field of biomaterials and tissue engineering. This thesis is therefore presented in a slightly unusual format. Background introduction and literature review are presented separately in separate chapters rather at the beginning of the thesis.

Chapter 2 studies the nanoparticle sintering evolution process via MD simulation in 2-Dimensions (2D). The nanoparticles with different sizes and different crystallographic orientations are selected as the initial configuration. All sintering evolution cases are carried out under different temperatures. The evolution process is then analysed by looking into all atoms' positions, potential energies and kinetic energies.

In order to compare the MD simulation with continuum model for nanoparticle sintering evolution, a 2D numerical continuum model is also created to model the interaction of two particles based on Pan's work in Chapter 3 [2]. This 2D continuum model of the sintering evolution of two particles is controlled by coupled surface diffusion and GB

diffusion. Therefore, by altering the diffusion coefficient of surface diffusion and GB diffusion, the sintering process dominated by either surface diffusion or GB diffusion can be modelled. The comparison between MD simulation and the continuum model is presented.

Chapter 4 further extends the MD simulation to 3D by studying the evolution of bamboo-like nanowires. Bamboo-like here refers to the nanowires composed of a row of long nanocrystals connected at the GBs. To reduce the computational burden in 3D, a multi-scale MD simulation is developed to address the evolution of bamboo-like nanowires. This multi-scale MD simulation treats the majority of nanocrystal bulk as an inert continuum phase and follows only the GB and the area around it in the full atomistic model.

Chapter 5 uses this multi-scale MD model to study the amorphous interlamellar phase in semicrystalline polymers. It is commonly known that the mechanical property of semicrystalline polymers is mainly dominated by the amorphous interlamellar phase. Therefore the amorphous interlamellar phase is modelled in a full atomistic fashion. The two crystal lamellars around it are regarded as inert and rigid, but the atoms in the crystal lamellar surface still have a realistic atomic interaction with the amorphous phase. The amorphous interlamellar phase is constructed via the Monte Carlo (MC) method developed by Rutledge [3]. After equilibration of the amorphous interlamellar phase, the mechanical property of the interlamellar phase is then investigated by introducing strain into the model.

Chapter 6 introduces the biodegradation concept into the amorphous interlamellar phase. Degradation is achieved by breaking the covalent bonds in the polymer chain. After the chain breakage the interlamellar phase is re-equilibrated and re-analysed. The

mechanical property of the equilibrated degradation result is also investigated. By studying the structure and the mechanical property of degraded semicrystalline polymers, the biodegradation process of semicrystalline polymers is then analysed. Finally, Chapter 7 outlines the major achievements of this work.

The work presented in this thesis did not use any commercial or open resource codes. All the MD codes including the pre- and post- processing codes were developed by the author. This is because most of the objectives in this project cannot be achieved by using existing codes. The multi-scale MD scheme was developed in this project and simply did not exist in any commercial or open resource code.

## **Chapter 2      Molecular Dynamics (MD) Study of Nanoparticles Sintering**

### ***2.1 Sintering of nanoparticles***

Nanostructured materials are a new class of materials that provide one of the greatest potentials for improving performance and extended capabilities of products in a number of industrial sectors including the aerospace, tooling, automotive, recording, cosmetics, electric motor, duplication and refrigeration industries[4]. Nanostructured materials can be defined as those materials whose structural elements—clusters, crystallites or molecules—have dimensions in the 1 to 100 nm range. The explosion in both academic and industrial interest in these materials over the past decade has arisen from the remarkable variations in their fundamental electrical, optical and magnetic properties. Encompassed by this class of materials are multilayers, nanocrystalline materials and nanocomposites. Their uniqueness is because of the very large percentage of atoms at their interfaces. Goncalves[5] summarised four methods that are commonly used in the synthesis and assembly of nanostructured materials. The most practical and important one is the production of isolated, ultrafine crystallites with uncontaminated free surfaces, followed by a sintering, consolidation process at a range of different temperatures. Nanostructured materials are isolated using methods such as precipitation from original solutions, inert gas condensation and the decomposition of the chemical precursors. Sintering is a thermal treatment for bonding particles together into a coherent, predominantly solid structure via mass transport events that occur largely at the atomic level. This bonding leads to improved strength and a lower system energy. Typically, surface energy is assessed by the surface area; smaller particles have high surface areas and more energy per unit volume, which promotes faster sintering. If the surface area is

very high, the expectation is for controlled sintering through surface diffusion with reduced densification. Yet, the contrary trend is observed, nanoparticles sintered with rapid densification[6]. The main challenge for nanoparticles sintering so far is to avoid coarsening during powder or material processing so that the nanostructure can be maintained. Therefore, for nanoparticle sintering, it is very important to investigate the very detail of mass transport mechanism involved to prove or disprove the conventional sintering mechanism in nanoparticle regions.

## ***2.2 Purpose of MD modelling of nanoparticle interaction***

Recently, Pan and co-workers[7] observed some interesting phenomena about nanoparticle sintering by using a continuum model to compare sintering behaviour between nanoparticles and microparticles. They found that during nanoparticle sintering if one small particle is placed between two large particles and the surface diffusion dominates the process, the small nanoparticle shows some resistance to the invasion of large particles, which does not happen in microparticle sintering. However it may be argued that the continuum model used by Ch'ng and Pan is invalid for nanoparticles because such particles should be considered as discrete assemblies of atoms. The purpose of this project is to provide a careful comparison between the molecular dynamics model and the continuum model for nanoparticle sintering in order to gain an insight into the difference between the two models. In this chapter, we apply MD simulation to conduct various nanoparticle sintering models. Until now, only a few kinds of materials have been investigated by MD simulation. Zhu and Averbach[8] performed MD simulation on copper nanoparticles and suggested that the high shear stresses in the neck could lead to rapid nanoparticle sintering. Therefore, the mechanism

responsible for sintering should be of plastic deformation. Zeng[9] also looked into copper nanoparticle sintering via MD simulation and noticed that surface and GB diffusion are the two main mechanisms, although there are early stage dislocations. Raut and Bhagat[10] studied both plastic deformation and surface diffusion during nanoparticle sintering. Tsuruta[11] carried out parallel MD simulation on both silicon nitride crystals and amorphous nanocluster sintering, observing the relative rotation at an early sintering stage and noting that the sintering was driven by surface diffusion. Overall, although the sintering mechanism varies for different nanoparticles, understanding of the nanoparticle sintering mechanism remains poor.

## ***2.3 An overview of conventional solid-state sintering***

### **2.3.1 The driving force for sintering**

Humans have known about sintering for thousands of years. It is a universal technique of forming material parts from powders. Many everyday items such as pots and bricks were produced by firing clays in many countries. Nowadays, sintering remains a primary operation in the production of ceramics. Modern sintering theory is based on the classic works of well-known scientists such as Herring[12], Kingery[13], Coble[14] and Ashby[15].

In conventional solid-state sintering, sintering forms solid bonds between particles when they are heated. Powders are compacted and then heat-treated in a furnace to an elevated temperature (but below melting point, about 50–90% of the melting temperature). Densification and particle coalescence occur during the process.

Compacts of 60–70% density can be sintered to about 100% density. Both metallic and ceramic powders can be used in solid-state sintering.

The energy difference between loosely packed powder and a fully dense body is the excess energy due to the broken bonds at the surfaces. Moreover, grain growth can bring about the secondary elimination of the GB area. The GB is also a defective region that is the source of GB energy. Apparently, the driving force for sintering is the reduction of the total interfacial energy, both surface energy, which happens mostly in the first stage of sintering, and GB energy, which takes place in the middle and later stages.

The model geometry sketched in Figure 2.1 explains how the reduction of surface area generates the driving force[6]. This model consists of a spherical particle and a flat surface of the same material.

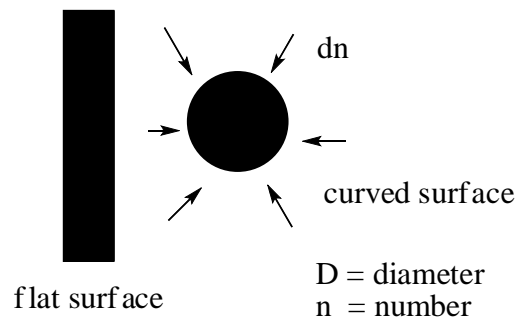


Figure 2.1 Sphere and plate as a basis for examining the energy difference associated with a curved surface.

The volume and surface area of the particle are given by

$$V = \frac{\pi}{6} D^3 \quad (2.1)$$

$$A = \pi D^2 \quad (2.2)$$

The volume of the sphere represents a collection of  $n$  atoms, each with a volume of  $\Omega$ , known as the atomic volume ( $V = n\Omega$ ). If the sphere undergoes a change in the number of atoms  $dn$ , there is a corresponding change in diameter  $dD$  and volume  $dV$ :

$$dV = \Omega dn = \frac{\pi D^2 dD}{2} \quad (2.3)$$

There is a chemical potential difference between the flat surface and sphere,  $\Delta U$ , because of the higher surface area per unit volume of the sphere. The chemical potential difference relates to the change in surface energy with an addition of new atoms to the sphere and the surface energy is proportional to the total surface area:

$$\Delta U = \gamma \frac{dA}{dn} = \gamma 2\pi D \frac{dD}{dn} \quad (2.4)$$

$\gamma$  is the energy unit of chemical potential. Inserting equation 2.3 here leads to a difference in chemical potential between the spherical surface and flat surface as follows:

$$\Delta U = \frac{4\gamma\Omega}{D} \quad (2.5)$$

The addition of atoms to the sphere leads to an energy increase that is effectively the same as a stress  $\sigma$  working against the growth of the volume:

$$\sigma dV = \Delta U dn \quad (2.6)$$

By substituting equation 2.3 and 2.5, the effective stress on the sphere is given as:

$$\sigma = \frac{4\gamma}{D} \quad (2.7)$$

which represents the stress associated with a curved surface. The flat surface corresponds to  $D = \infty$ ; thus, stress  $\sigma = 0$ . For smaller particles, the surface stress is higher and more energetic. In sintering, this stress directs mass flow to give particle bonding and other actions that remove the surface curvature in the sintering system. For example, the concave solid surface tends to fill and the convex surface tends to flatten. Typically, the smaller the particle size, the greater the driving force. When the temperature is raised, the atoms have sufficient mobility. The sintering process is then expected to start. Although the sintering driving force is universal to all sintering events, the mass transport mechanisms are very different and correspond to different sintering situations, which will be discussed in detail later.

### **2.3.2 The sintering stages**

To understand the complete sintering process, it is necessary to know the classical model of sintering, which postulates three different stages of the process.

#### **First stage: initial stage neck growth**

The growth of the sinter bond from an initial loose powder contact is recognised as the initial stage of sintering. It is characterised by the rapid growth of the interparticle neck. Although there is considerable neck growth, the actual volume of the neck is small; it takes a small mass to form a neck. The initial stage ends when the necks begin to increase at approximately a neck size ratio  $X/D$  of 0.3. Various laws link the neck size ratio to other useful sintering parameters, including shrinkage, surface area and density. Neck growth is the primary concern of initial stage sintering research. There have been many mature theories regarding the neck growth problem. Most famous is the virtue

power principle, which provides an estimate of the relative rate of neck growth from any transport mechanism.

The simplified two-sphere model for sintering illustrated in Figure 2.2 is used to introduce the neck growth concepts. The situation consists of two spheres of radii  $D$  with a neck of radius  $x$ . Associated with the neck is a volume  $V$  and an area  $A$ .

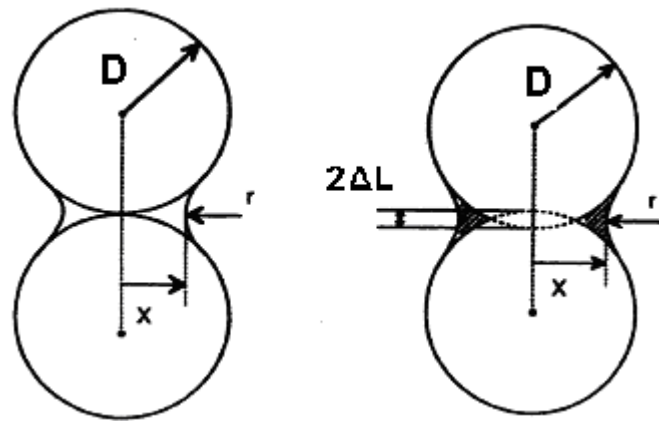


Figure 2.2 Two-sphere model used for initial stage sintering for (a) non-densifying mechanisms and (b) densifying mechanisms.  $r$  and  $X$  are the principle radii of the curvature of the neck surface,  $D$  is the radius of the sphere[6].

For non-densifying sintering, the interparticle distance doesn't decrease. The neck growth is filled via surface diffusion or vapour deposition. For the densifying sintering process, bulk transport processes decrease the interparticle spacing as neck growth proceeds, resulting in compact shrinkage and the formation of additional, new necks. Shrinkage is approximately related to the neck size by a simple model as follows[14]:

$$\frac{\Delta L}{L_0} = \left(\frac{X}{2D}\right)^2 \quad (2.8)$$

where the shrinkage  $\Delta L/L_0$  is the compact length change divided by the initial length.  $D$  is the radius of the sphere. For most MD simulation on sintering, the first stage of sintering is the most frequently investigated because of its significance and also because of the time limitation and accuracy of MD.

### **Intermediate stage**

The intermediate stage is characterised by simultaneous pore rounding, densification and grain growth. This stage is most important for densification and determining the properties of the sintered compact. The driving force is the elimination of the remaining surface energy and the reduction of GB area. In this stage, significant grain growth and pores form channels along the edges of the particles, as shown in Figure 2.3.

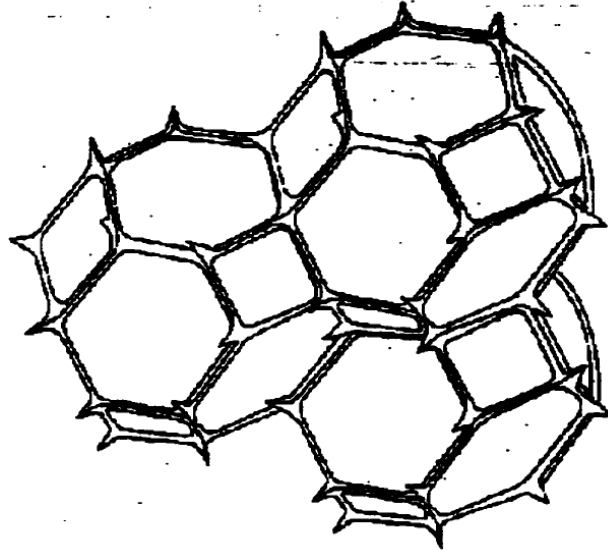


Figure 2.3 The tetrakaidecahedron model used in intermediate stage sintering[9].

Densification in the intermediate stage is accomplished by volume and GB diffusion. The coarsening of the large pores and elimination of the small pores are also promoted

via GB diffusion. Surface transport helps pore rounding and pore migration during grain growth.

### **Final stage**

During the final stage of sintering, pore channels shrink to some isolated quasi-spherical zones on the GBs or triple junctions. Depending on their sizes and geometries, the pores can become stable and cannot shrink further. The rate of pore shrinking does not depend on the pore size but only on how far apart the pores are.

### **2.3.3 Sintering mass transport mechanisms**

Transport mechanisms determine how mass flows in response to the driving force provided by the driving force for sintering. In general, there are two classes of mechanisms involved in the sintering process: surface transport and bulk transport. Each class is composed of several actual atomistic mechanisms contributing to mass flow. Surface transport processes produce neck growth without shrinkage or densification because mass flow is limited to the particle surface. Surface diffusion and evaporation condensation are recognised as two important surface transport mechanisms. Bulk transport mechanisms include volume diffusion, GB diffusion, plastic flow and viscous flow. They not only promote neck growth but also bring about shrinkage during sintering because the mass flow happens inside the bulk. Almost every mechanism for matter redistribution has been reported to form the neck; as mentioned above, neck growth is vital for sintering research. The neck size can be related to time and the size of the particles by[6]:

$$\left(\frac{X}{D}\right)^n = \frac{Bt}{D^m} \quad (2.9)$$

where X is the neck diameter, D is the particle diameter, t is the isothermal sintering time and B is a term that collects material and geometric constants. The values of n and m change with the time and degree of sintering, but for many analyses they have been assumed to be constant with the mechanism of mass transport (Table 2.1). Many experiments have been analysed using the exponent n to identify the sintering mechanism.

Table 2.1 The constants n in equation 2.9

Mechanism	n
1. Surface diffusion	7
2. Volume diffusion	5
3. Vapour diffusion	3
4. GB diffusion	6
5. Viscous flow	2

### Surface diffusion

The surfaces of crystalline solids usually consist of defects that include ledges, kinks and vacancies. Surface diffusion involves the motion of atoms between these sites. Surface diffusion becomes an active process during heating to the sintering temperature. Usually, the activation energy for surface diffusion is less than that for other mass transport processes. Consequently, it initiates at lower temperatures compared with

other sintering mechanisms. Moreover, because surface diffusion does not bring about densification, rapid heating can be applied to sintering to reduce low temperature surface diffusion when densification is desired, particularly for nanoparticle sintering (because of the huge surface area nanoparticles contain, surface diffusion is extremely active). Rapid heating has been applied to overcome fast surface diffusion[16]. However, it is not that successful.

### **Vapour evaporation and condensation**

Vapour transport during sintering leads to the repositioning of atoms located on the particle surface, without densification. Evaporation occurs from a surface and transport occurs across pore space, leading to condensation on a nearby surface. The net result over time is a reduction in the total surface area as bonds grow between touching particles, but there is no change in the distance between particle centres. In other words, the fraction of atoms on surface sites decreases as layers of surface atoms build up on concave surfaces at the expense of convex surfaces. Typically, evaporation occurs preferentially from flat or convex particle surfaces. Preferential deposition occurs at concave necks between particles where the vapour pressure is slightly below the equilibrium. For many materials evaporation–condensation transport is slow at typical sintering temperatures, so it is often ignored. Alternatively, sintering can be dominated by vapour transport for small powders with high surface areas and high vapour pressures. Moreover, there are many cases where the sintering atmosphere can induce vapour transport even when the apparent vapour pressure of the material being sintered is low.

### **GB diffusion**

GB diffusion is perhaps the most important mechanism for the sintering densification of most metals and ceramic powders. GBs form in the sinter bond between individual particles because of misaligned crystals. This defective characteristic of the GB allows mass flow with an activation energy that is usually intermediate between that for the surface diffusion and volume diffusion. The GB is narrow, but it is still an active transport path. Mass is removed along the GB and redeposited at the sinter bond. GB energy has a significant effect on GB diffusion. High GB energy is a prime cause of simultaneous grain growth during sintering, leading to difficulties attaining full density in many systems. Low GB energy makes continued sintering favourable.

### **Volume diffusion**

Volume diffusion, or lattice diffusion, involves the motion of vacancies through a crystalline structure. There are three main vacancy diffusion paths that contribute to sintering. One path is from the neck surface through the particle interior, with the subsequent emergence at the particle surface. The net result is the deposition of mass at the neck surface. This is termed volume diffusion adhesion because there is no densification. The second path, termed volume diffusion densification, involves vacancy flow to the interparticle GB from the neck surface, which produces shrinkage. Finally, the vacancies can be emitted or annihilated by dislocations via a process termed dislocation climb. This involves cooperative action by both dislocations and vacancies.

Although volume diffusion is active in most materials at high temperatures, it is often not the dominant mass transport process during sintering, especially for small powders. The activation energy for surface diffusion is typically lower and, in many cases, GB

diffusion has an activation energy intermediate between surface and volume diffusion. Consequently, interfacial diffusion processes (surface and boundary diffusion) are generally more active. If the material has a small grain size or small particle size, the effective transport via interfacial paths dominates sintering.

### **Viscous flow**

Amorphous materials exhibit a decreasing viscosity (increased flow) as temperature increases. Under applied stress, a viscous material will flow. Thus, at high temperatures glass and polymer powders densify in response to sintering stress. This process has been observed in the sintering of many silicate glasses as well as common polymers, that is the lower the viscosity, the more rapid the sintering process. If external stress is applied, the rate of sintering increases in proportion to the applied stress. The two-particle sintering situation is different for amorphous materials than for crystalline solids since the former lack a GB at the neck region. Consequently, as neck growth proceeds, amorphous materials can readily achieve a zero curvature condition where the convex and concave radii are equal but opposite in sign. As a practical consequence, low-packing density structures cannot fully densify by viscous flow.

## 2.4 Computer Simulation of Sintering Using Molecular Dynamics

### 2.4.1 The fundamentals of Molecular Dynamics simulation

The MD simulation consists of the stepwise time integration of Newton's equation of motion for a set of  $N$  particles:

$$m_i \frac{d^2 r_i}{dt^2} = F_i(r_1, r_2, \dots, r_N) \quad (2.10)$$

where

$$F_i(r_1, r_2, \dots, r_N) = -\nabla_{r_i} U(r_1, r_2, \dots, r_N) \quad (2.11)$$

Here  $r_i$  is the position vector of particle  $i$  and  $F_i$  is the force vector acting on the particle  $i$ .  $U_i$  is the total potential energy generated by all the  $N$  particles involved. The Hamiltonian  $H$  of this system can be written as the sum of kinetic energy ( $K$ ) and potential energy ( $U$ ) functions of each atom's coordinates  $X_i$  and momentum  $p_i$ .

$$H = K + U \quad (2.12)$$

where

$$K = \sum_{i=1}^N \frac{1}{2} m_i \left( \frac{d(r_i(t))}{dt} \right)^2 \quad (2.13)$$

and

$$U = \sum_i \sum_{i \neq j} U(r_{ij}) \quad (2.14)$$

Most familiar states of matter (solid, liquid and gas) are based on spherical particles (atoms or molecules) that interact with one another. The interactions at the simplest level occur between pairs of atoms and are responsible for providing the two principal features of an interatomic force. The first is a resistance to compression, which means that the interaction repels at close range. The second is to bind the atoms together in the solid and liquid states, and for this the atoms must attract each other over a range of separations. Potential functions exhibiting these characteristics can adopt a variety of forms and, when chosen carefully, actually provide useful models for real substances. This project starts with the well-known Lennard-Jones (LJ) potential, which is the equation 2.15.

$$U = 4\varepsilon\left[\left(\frac{\sigma}{r}\right)^{12} - \left(\frac{\sigma}{r}\right)^6\right] \quad (2.15)$$

where  $\varepsilon$  is the unit energy,  $r$  is the distance between two particles,  $\sigma$  is the equilibrium distance. The total potential energy  $U$ , which contains the interatomic interactions, is calculated according to 2.14.

The left side of the above equation expresses the Newton's equations of motion for a multi-body system. The evaluation of the right-hand side of Equation 2.16 is the key step that usually consumes most of the computational time in an MD simulation, so its efficiency is crucial. Usually a smooth interaction cut-off limit  $r_c$  will be used. Moreover, in this project the cell-assisted neighbour list method is employed and a list of atom pairs within the range  $r_n$  is constructed.

$$U = 4\varepsilon\left[\left(\frac{\sigma}{r}\right)^{12} - \left(\frac{\sigma}{r}\right)^6\right] \quad , \quad r < r_c \quad \text{and} \quad U = 0, r \geq r_c \quad (2.16)$$

To allow this list to be useful over several successive time steps  $r_c$  is replaced by  $r_n$

$$r_n = r_c + \Delta r \quad (2.17)$$

If any pair's distance change becomes larger than  $\Delta r$ , the neighbour list should be rebuilt. As a result, the amount of computation can be massively reduced.

## 2.4.2 Leap frog integration

The integration of the equations of motion uses the simplest of numerical techniques, namely the leap frog method[17]. This method has excellent energy conservation properties, is widely used and its storage requirement is also minimal. The derivation of leap frog methods follows immediately from the Taylor expansion of the coordinate variable, typically  $r(t)$ :

$$r(t+h) = r(t) + h\dot{r}(t) + (h^2/2)\ddot{r}(t) + O(h^3) \quad (2.18)$$

where  $t$  is the current time and  $h = \Delta t$ .

$$r(t+h) = r(t) + h[\dot{r}(t) + (h/2)\ddot{r}(t)] + O(h^3)$$

$$r(t+h) = r(t) + h\dot{r}(t+h/2) \quad (2.19)$$

The term multiplying  $h$  is  $\dot{r}(t+h/2)$ , which is to the same as picking the middle velocity as the following pictures describe.

### 2.4.3 Reduced units

Reduced units or dimensionless units are commonly used in MD simulations. There are several reasons for doing this, not least the ability to work with numerical values that are not too distant from unity instead of the extremely small values normally associated with the atomic scale. Another benefit of dimensionless units is that the equations of motion are simplified because some, if not all, of the parameters defining the model are absorbed into the units. The most familiar reason for using such units is related to the general notion of scaling, namely, that a single model can describe a whole class of problems, and once the properties have been measured in dimensionless units they can easily be scaled to the appropriate physical units for each problem of interest.

In this project,  $\sigma$ ,  $\epsilon$  and  $m$  are chosen as the units of length, energy and mass, respectively. All other units in the simulation are then expressed in terms of these three basic units.

Table 2.2 The reduced unit, SI and the transformation equations

Reduced unit	Unit transformation equation
Mass ( $m$ )	$m$
Length ( $\sigma$ )	$\sigma$
Energy ( $\varepsilon$ )	$\varepsilon$
Velocity ( $v$ )	$\varepsilon = \frac{v^2}{m}; \rightarrow v = \sqrt{\frac{m}{\varepsilon}}$
Time ( $t$ )	$v = \frac{\sigma}{t}; \rightarrow t = \frac{\sigma}{v} = \sigma \sqrt{\frac{m}{\varepsilon}}$
Force ( $f$ )	$f = ma = m \frac{v}{t} = m \frac{\sqrt{\varepsilon/m}}{\sigma \sqrt{m/\varepsilon}} = \frac{\varepsilon}{\sigma}$
Pressure ( $P$ )	$P = \frac{f}{\sigma^2} = \frac{\varepsilon}{\sigma^3}$
Temperature ( $T$ )	$T = \frac{\varepsilon}{k_B}$
Density ( $\rho$ )	$\rho = \frac{m}{\sigma^3}$

#### 2.4.4 Boundary conditions

There are two major types of boundary conditions: isolated boundary condition (IBC, sometimes being called free surface condition) and periodic boundary condition (PBC). These are both employed in the simulation. In IBC, the  $N$  particle system is surrounded by a vacuum. These particles interact among themselves, but are presumed to be so far away from everything else in the universe that no interactions with the outside occur except perhaps when responding to some well-defined “external forcing”. In PBC, one

explicitly keeps track of the motion of  $N$  particles in the so-called supercell, but the supercell is surrounded by infinitely replicated, periodic images of itself. Therefore a particle can interact not only with particles in the same supercell but also with particles in adjacent image supercells.

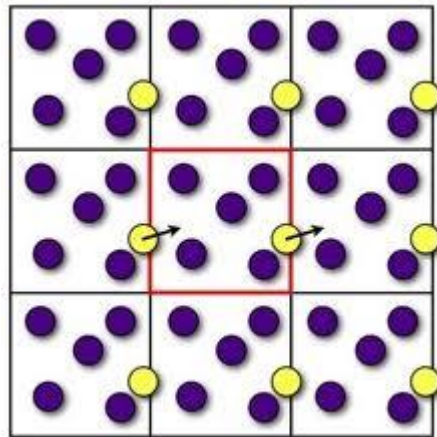


Figure 2.4 The illustration of the Periodic Boundary Condition (PBC)

## 2.5 MD simulation of 2D nanoparticle interactions

### 2.5.1 The models of nanoparticle interaction

We used MD with a simple 2D LJ model. The pairwise LJ potential[18] between two atoms at a distance  $r$  from each other is defined as equation 2.15. All measurements are expressed in units derived from the three basic units of energy  $\varepsilon$ , length  $\sigma$  and mass of an atom  $m$ . For example, the unit of time is  $t^* = \sigma(m/\varepsilon)^{1/2}$ , the unit of temperature is  $\varepsilon/k_B$ , where  $k_B$  is the Boltzmann constant, and so on.

The time step of  $0.02t^*$  is used to guarantee the stable numerical integration of the equations of motion. An example of the starting configurations is shown in Figure 2.5.

Each bulk atom has six nearest neighbour atoms. This 2D configuration corresponds to the (111) oriented layer of a 3D face-centred cubic (fcc) crystal.

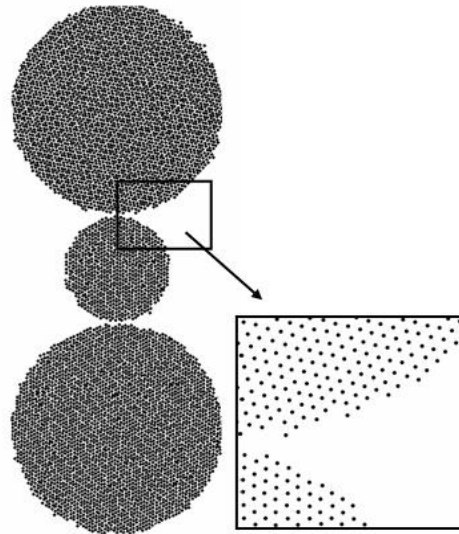


Figure 2.5 The initial configuration of the MD model of three particles in contact with each other.

Before the three particles are placed in contact with each other, each particle is equilibrated for  $10000t^*$  at a constant temperature. The constant temperature is realised by rescaling the average velocity of each atom to keep the kinetic energy constant[19]. The equilibrated particles are rotated with respect to each other to investigate the effect of crystallographic orientation on the process of neck formation. The particles are then placed next to each other such that the distance between the nearest atoms from two contacting particles is about  $1.7\sigma$ . To prevent the loss of any vapour atoms from the system, PBCs are employed, so that a vapour atom leaving the simulation cell through the boundary is reintroduced into the cell with the same velocity at the opposite boundary. The size of the simulation cell is large enough to prevent atoms on the particles from interacting with their neighbour images except for vapour atoms.

Following Ch'ng and Pan,[7] three different particle arrangements are used to study the particle interactions. In configuration I, a small particle whose radius is  $16\sigma$  is placed next to a particle twice the size. In configuration II, two same sized particles (radius =  $32\sigma$ ) are placed in contact. In configuration III, one small particle is placed along a straight line between two larger particles (Figure 2). The larger particles consist of around 3000 atoms, whereas the smaller one consists of around 1000 atoms.

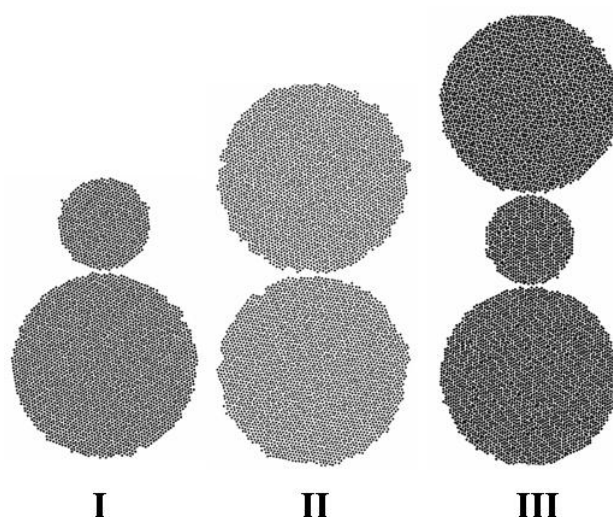


Figure 2.6 The three different configurations of particles: I, two particles of different sizes; II, two same sized particles; III, one small particle in the middle of two larger particles.

The simulation results, including atom coordinates, velocities and potential energy, are recorded every 500 time steps. Thus, the simulation progress can be observed directly from a dynamic movie obtained by plotting all atom coordinates. When two particles join together they create a “neck”. We monitor neck growth over time by measuring its width, defined as the distance between the outer atoms at the narrowest place. We also measure the particle centre-to-centre distance, as determined by measuring the distance

between mass centres of the core parts of the particles with a radius about  $10\sigma$ , which remain crystalline throughout the simulation and thereby provide an accurate measure of relative particle displacement during sintering.

## 2.5.2 Subtraction of the rigid motion of the entire system

In an MD simulation, it is inevitable that a certain amount of vapour atoms will exist. When a vapour atom flies across the periodic boundary the angular momentum of the system changes, causing the system to move and rotate rigidly. Sintering occurs by atoms migrating mainly along the particle surfaces. Atoms at the core of a particle only vibrate thermally and move rigidly. The translational and rotational rigid motions have to be eliminated (Figure 4) during post-processing to filter out information such as atoms diffusion path, neck size and centre-to-centre distance. This numerical detail is presented here to demonstrate the feature of the MD model that does not exist in the continuum model. Considering a rigid core of a particle that contains  $n$  atoms, after certain time  $t$ , the rigid core rotates by an angle  $\alpha$  about its mass centre. Inside the rigid core, the atom coordinates before and after rotation are denoted by  $r_i$  and  $r'_i$ .

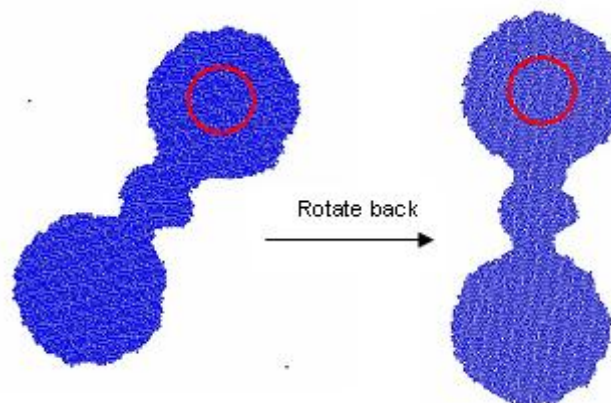


Figure 2.7 Mathematical subtraction of rigid rotation during post processing.

The angle  $\alpha$  of the rigid rotation of the particle core can be calculated as:

$$\sin \alpha = \frac{\sum_i |d_i \times d'_i|}{\sum_i |d_i \parallel d'_i|}, \quad (2.20)$$

where  $d_i = r_i - r_{\text{cm}}$  is the atomic coordinates with respect to the mass centre of the particle core. The rigid motion can then be subtracted from the atomic coordinates according to the following coordinate transformation equations:

$$x''_i = (x'_i - x_{\text{cm}}) \cos \alpha + (y'_i - y_{\text{cm}}) \sin \alpha + x_{\text{cm}}, \quad (2.21)$$

$$y''_i = -(y'_i - y_{\text{cm}}) \sin \alpha + (x'_i - x_{\text{cm}}) \cos \alpha + y_{\text{cm}}, \quad (2.22)$$

where  $r'_i = (x'_i, y'_i)$  and  $r''_i = (x''_i, y''_i)$  denote the atomic coordinates before and after rotation subtraction.

### 2.5.3 Neck size and centre-to-centre distance

The simulation result including coordinates, velocities and potential was recorded at every 5000 time steps. The direct simulation's progress could be observed from the dynamic movie made by plotting all the coordinates. After the system rotation subtraction, the neck size was recorded by scanning the neck part during a sintering experiment. The detailed scanning is as follows. The neck part is divided into several thin layers. Each layer is about 2 Å thick. The size of each layer is measured and the smallest neck size is selected. For those necks with a migrating GB, the neck size is determined manually.

The centre-to-centre distance is determined by measuring the distance between the mass centres of the very core parts of the particles. Since the very core parts of the particles

almost always remain crystalline during the whole sintering process, the distance of the mass centre of the core part could somehow provide information on the approaching of two particles, although this distance cannot be treated as the centre-to-centre distance of two particles during sintering.

## 2.6 Results and discussion

### 2.6.1 Volume fraction of atoms at the particle surface

From the point of view of the continuum model, the driving force for particle sintering is the reduction in the free energy associated with the particle surface. In a continuum model, the surface energy is simply proportional to the total surface area. It is therefore instructive to monitor the volume fraction of atoms on the particle surface in the MD simulation to check against the continuum concept.

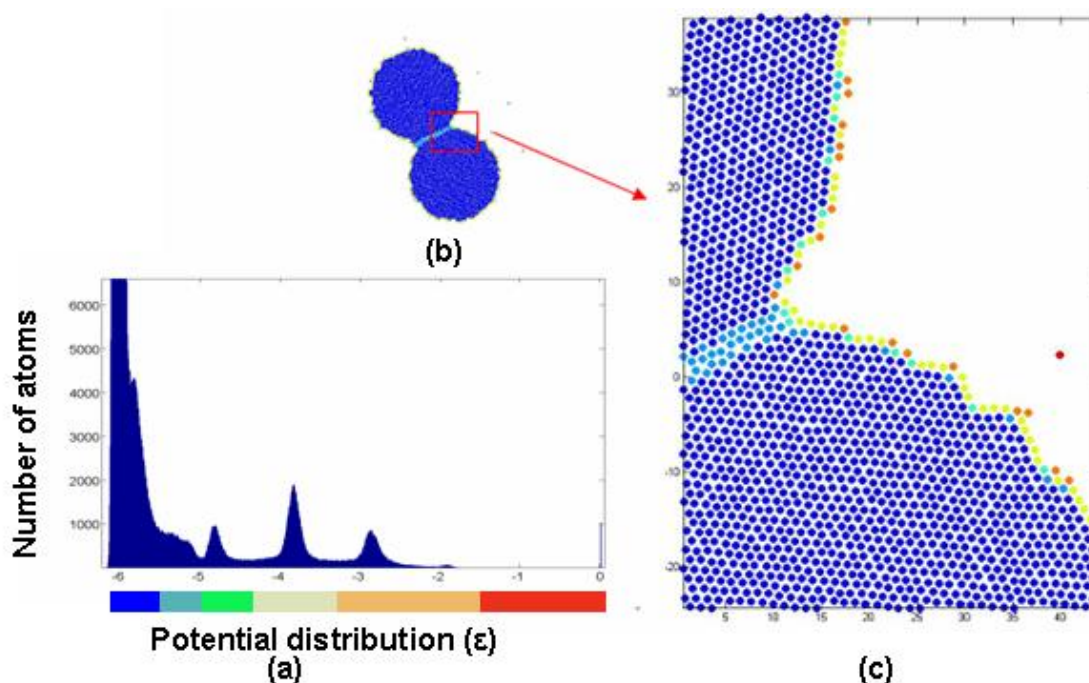


Figure 2.8 Number of atoms as a function of their potential energy, indicating their locations at different parts of the particle during sintering.

To do this, it is necessary to distinguish atoms from different parts of the system, i.e. on the surface, in the bulk, on the GB or in the vapour. This can be achieved by examining the potential energy of the interaction of an atom with other atoms. We record the average potential energy of each atom over 500 time steps. The histogram in Figure 6(a) shows the number of atoms as a function of their potential energy. It can be clearly observed that the number of atoms peaks around several values of the potential energy, each representing a group of atoms with a particular number of nearest neighbour atoms. The numbers of neighbouring atoms are indicated by colours as shown in the Figure 2.8. The peaks from left to right represent atoms with six, five, four, three and zero neighbours, respectively. The left prime peak represents the majority of atoms in the bulk, which have all six neighbours arranged in a correct crystal configuration. The sub-peak under the prime peak represents atoms on the GB (i.e. distorted crystal configuration). All the other peaks except for the vapour atoms represent atoms on the particle surface. This identification of different atoms can be used to monitor mass transport during the sintering process. Figure 2.9 shows the volume fraction of the surface atoms (with a potential energy larger than  $-5.0$ ) as a function of time for the two particles sintering in configuration II. It can be clearly seen that the total number of surface atoms decreases as sintering proceeds, which is consistent with the continuum concept that the driving force for sintering is a reduction in total surface energy.

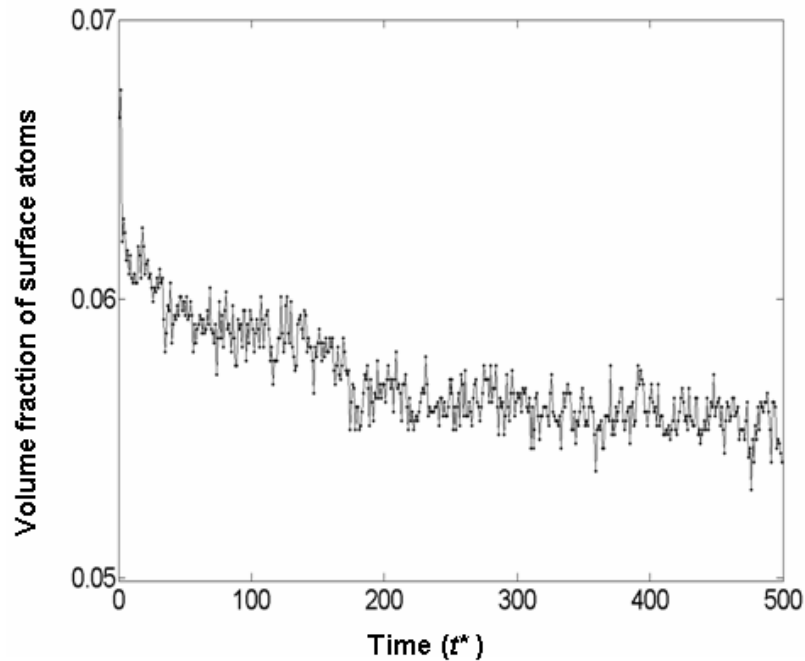


Figure 2.9 Volume fraction of surface atoms as a function of sintering time.

### 2.6.2 Effect of the crystalline orientation of the particles

The continuum model does not contain the crystalline orientation of the particles. This information in the MD model leads to a sintering behaviour that the continuum model is unable to capture. Figure 2.10 shows two particles with perfectly aligned initial crystalline orientation and Figure 2.11 shows three particles of different initial crystalline orientations. Only half of the particles are shown to reveal the relative rotation between the particles during sintering. The MD simulation shows that the particles with perfectly aligned initial crystalline orientation stay aligned during sintering. For particles of different initial crystalline orientations, a quick adjustment

occurs in the crystalline orientations at the very beginning of the sintering progress. The particles then remain in the adjusted orientations throughout the rest of the sintering process. This phenomenon has been observed by other researchers both experimentally[20] and in MD simulations[9]. The reorientation is believed to be driven by the minimisation of GB energy. However, the consequence of this reorientation on sintering has not been fully realised in previous studies. The MD simulation shows that the reorientation can eliminate a GB from the system and significantly retard the sintering process (Figure 2.12). In other cases, a stable GB is formed after the initial adjustment, as shown in Figure 2.13. Our simulations show that three factors can help the formation of a stable GB: (a) a large angle of initial misalignment between the particles, (b) large particle size and (c) high sintering temperature. In the 2D MD model, the maximum misalignment angle is 30 degrees because of the sixfold symmetry of the crystalline structure. The initial misalignment has to be large enough to resist the elimination of the GB by particle reorientation. Our simulation suggests that GBs are more likely to form between two large nanoparticles if the initial misalignment angle is larger than 20 degrees. Furthermore, the MD simulation shows that a GB is more likely to form between the two large nanoparticles in configuration II (Figure 2.6), but rarely forms between two smaller nanoparticles. The smaller particles are relatively easy to reorient themselves to eliminate the GB. A typical evolution of the system in configuration III is that the small particle quickly aligns with one of the large particles to form a single crystal, whereas a GB is formed between the small particle and the other large one.

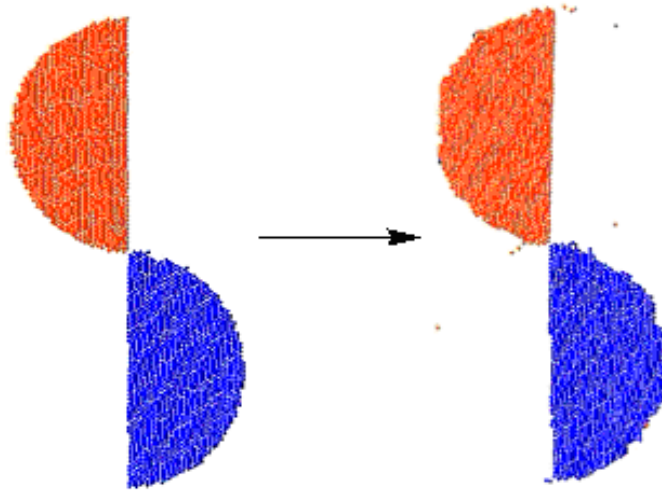


Figure 2.10 Particles with initially aligned crystal orientations maintain their alignment during sintering; only half of the particles are shown to reveal their relative rotation.

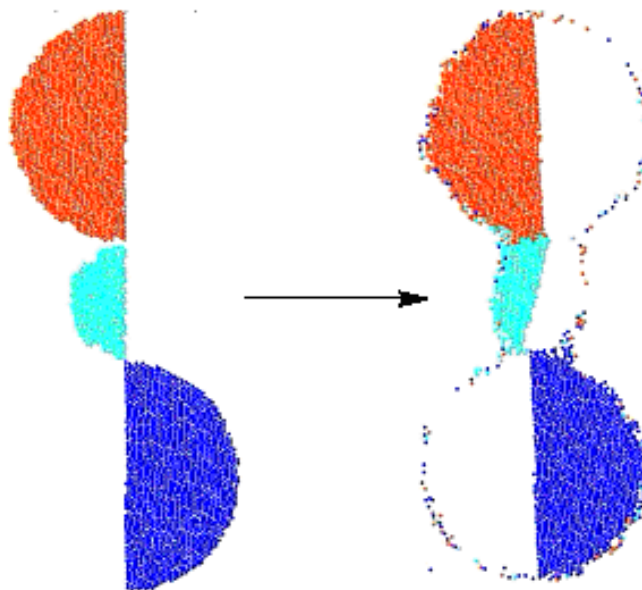


Figure 2.11 Particles with initially misaligned crystal orientations. The small particle reorients itself at the very beginning of the sintering process; only half of the particles are shown to reveal their relative rotation.

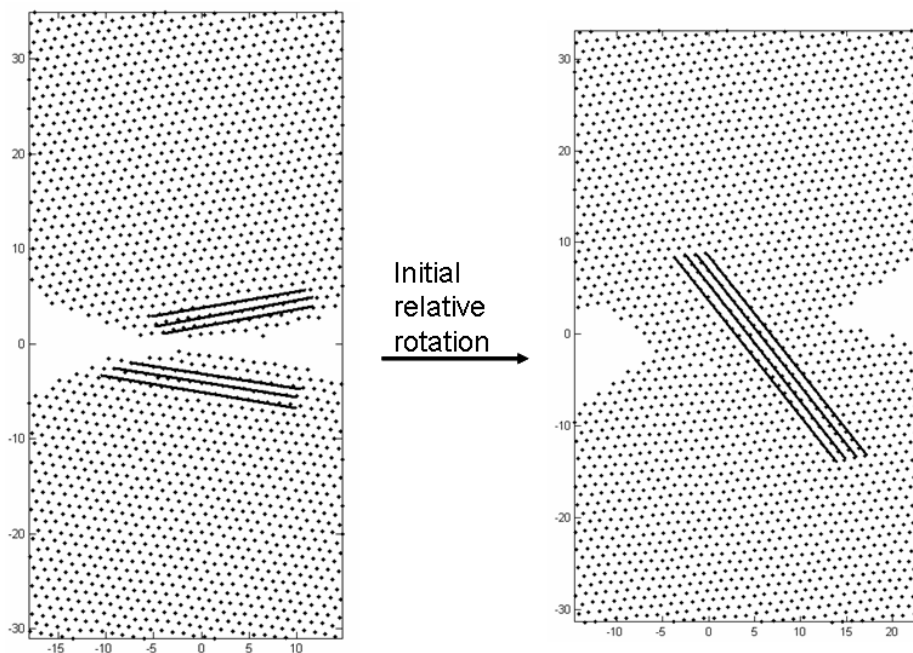


Figure 2.12 Two nanoparticles sinter together to form a single crystal; the red lines mark the crystalline orientations before and after the reorientation.

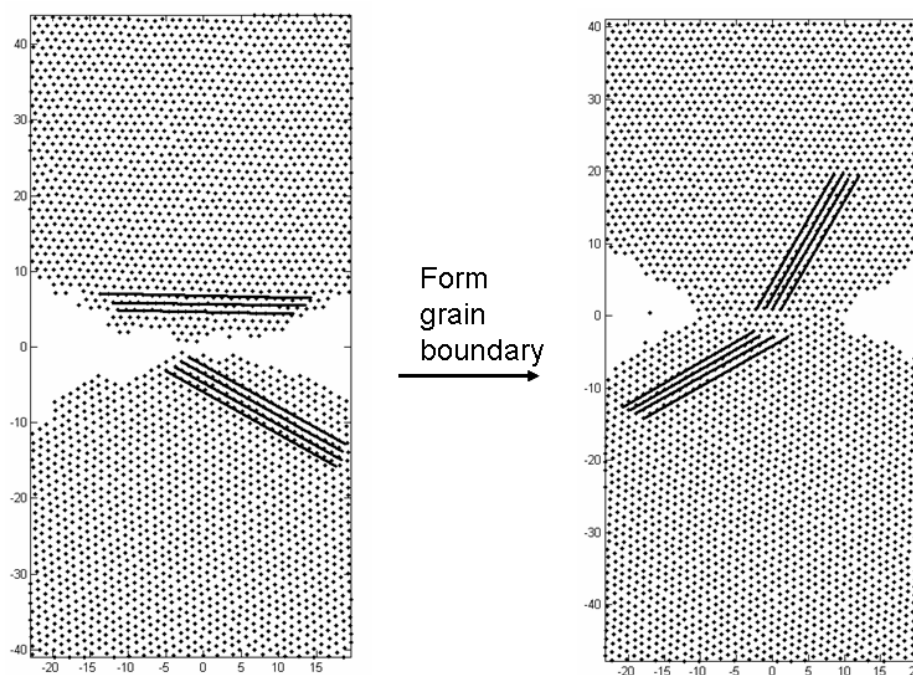


Figure 2.13 Two nanoparticles sinter together to form a GB; the red lines mark the crystalline orientations before and after the reorientation.

### 2.6.3 Sintering particles

The primary conclusion of the continuum modelling by Ch'ng and Pan[7] is that nanoparticles arranged in configuration III shown in Figure 2.6 seem to possess certain resistance to particle coarsening, whereas configuration I does not show such resistance. However, using the continuum model for particles consisting of only a few thousand atoms pushes its validity to the limit. One major feature that the continuum model is unable to capture is the elimination of the GB as shown in Section 2.6.2. If a GB is eliminated, the GB diffusion process ceases to exist, leaving only surface diffusion and vapour evaporation and condensation as the mechanisms for matter redistribution. This phenomenon has a profound effect on the sintering behaviour of the particles.

The melting temperature of the 2D LJ crystal is  $T_m=0.415 \text{ } \varepsilon/k_B$ . [21] We performed MD simulations at two different temperatures:  $T=0.19 \text{ } \varepsilon/k_B$  and  $T=0.26 \text{ } \varepsilon/k_B$ , which are 46% and 63% of the melting temperature, respectively. It is clear that sintering occurs much faster at the higher temperature. For the two identical particles of initial diameter  $70\sigma$  (configuration II in Figure 2.6) without a GB, the neck size reached  $30\sigma$  at  $T=0.26 \text{ } \varepsilon/k_B$  after  $25000t^*$ , but only reached  $20\sigma$  at  $T=0.19 \text{ } \varepsilon/k_B$  in the same time. If a GB was formed, then the neck size reached  $45\sigma$  at  $T=0.26 \text{ } \varepsilon/k_B$  after  $25000t^*$ . Figures 2.14–2.16 show the MD simulations for the three particle configurations sintering at  $T=0.26 \text{ } \varepsilon/k_B$ . We have picked three cases for which the GBs were eliminated at the beginning of the simulation. In all figures showing MD simulations, the following colouring scheme is used: the bulk atoms are always coloured blue, any atom that has been on the surface and GB of the particle is coloured red and any atom that has been in the vapour is coloured cyan. The colouring scheme, therefore, traces the history rather than the current state of the atoms, providing a rough picture of the matter redistribution during

the simulation run. In Figure 2.14, one small particle is placed between two larger particles. At the very beginning, the particles quickly joined together and formed two necks. Although there was a time lag between the formations of the two necks, by  $100\tau^*$  both necks were fully filled by surface atoms (shown in red) and the blue bulk part of the small particle had reduced in size. At the later stage, both surface diffusion and vapour condensation contributed to the growth of the neck. Figure 2.15 shows one small particle and one large particle in contact with each other. Initially, the quick neck formation was similar to the case in Figure 2.14. The neck was filled by atoms mostly coming from the small particle through surface diffusion. In the later stage of sintering, evaporation and condensation dominated matter redistribution. After the neck had been filled to the top, the small particle started to collapse and the whole system evolved towards a circular shape. Figure 2.16 shows two large particles of the same size in contact with each other. Again, the sintering process started with a quick neck formation followed by neck growth first by surface diffusion and then by vapour condensation. If one uses the continuum model, such behaviour of switching from one mechanism of matter transportation to another halfway through the sintering process would be very difficult, if not impossible, to handle. These three cases, therefore, highlight the difference between the MD and continuum models.

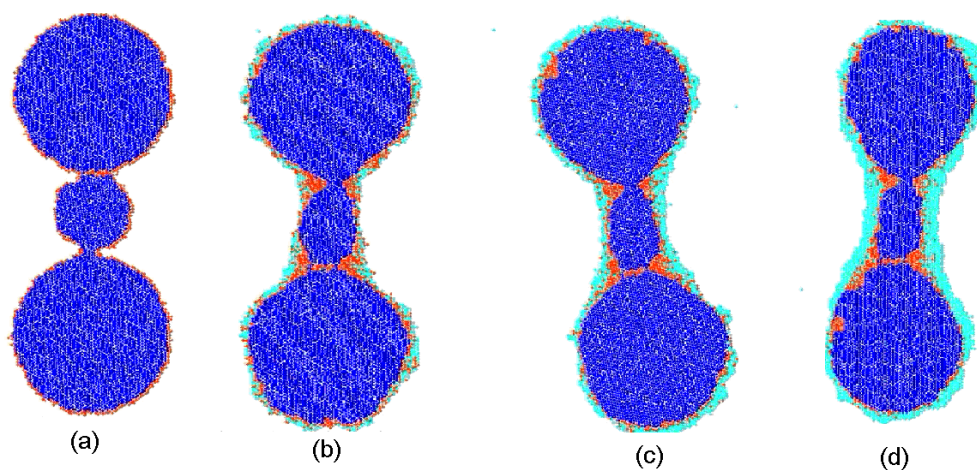


Figure 2.14 MD simulation of one small and two large particles sintering at  $T = 0.26 \epsilon/kB$ . (a)  $t = 500t^*$ ; (b)  $t = 50000t^*$ ; (c)  $t = 200000t^*$ ; (d)  $t = 500000t^*$ . See text for the explanation of the colour scheme.

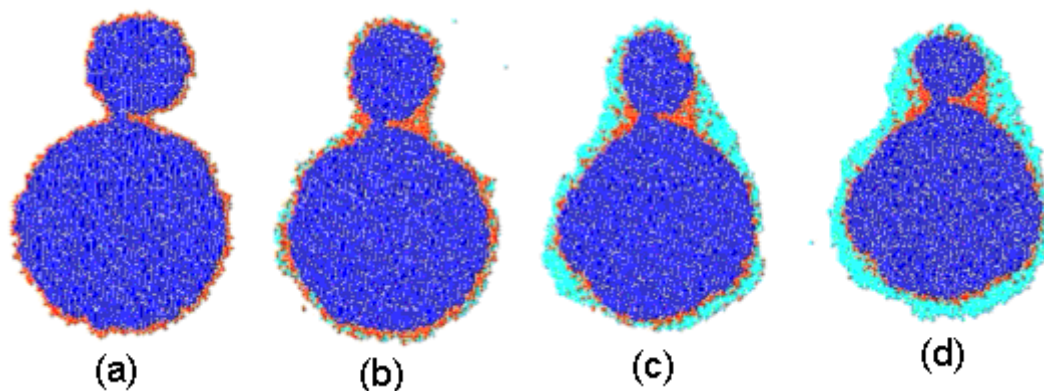


Figure 2.15 MD simulation of a small and a large particle sintering at  $T = 0.26 \epsilon/kB$ . (a)  $t = 500t^*$ ; (b)  $t = 50000t^*$ ; (c)  $t = 200000t^*$ ; (d)  $t = 500000t^*$ . See text for the explanation of the colour scheme.

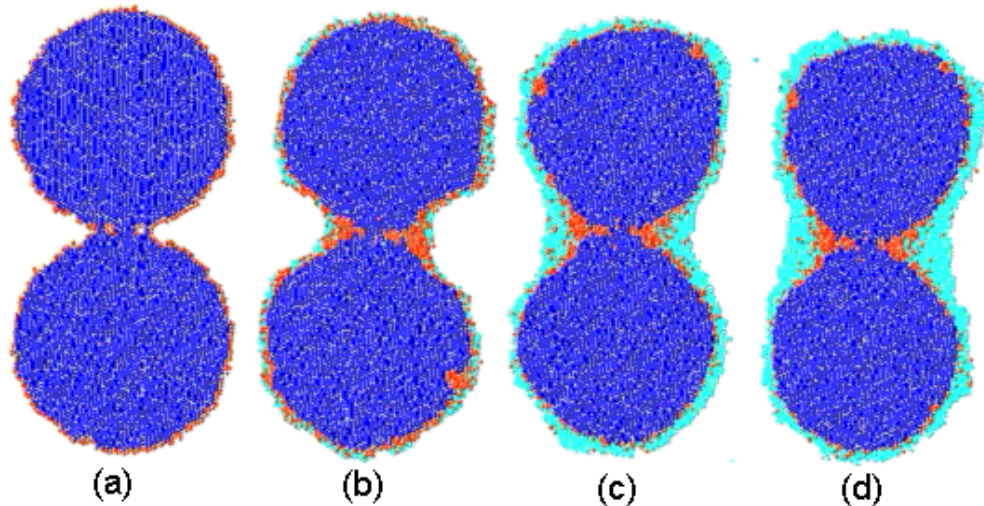


Figure 2.16 MD simulation of two large particles sintering at  $T = 0.26 \varepsilon/k_B$ . (a)  $t = 500t^*$ ; (b)  $t = 50000t^*$ ; (c)  $t = 200000t^*$ ; (d)  $t = 500000t^*$ . See text for the explanation of the colour scheme.

The locations of the centres of the mass of the particle cores were monitored during the simulation. In all three cases, there was no perceptible change in the distance between the particles. This indicated the absence of GB diffusion and that any bulk deformation of the particle was negligible. The simulations were then repeated at  $T = 0.19 \varepsilon/k_B$  at which evaporation is far less important. Figures 2.17, 2.18 and 2.19 show these cases. It is obvious from these figures that at lower sintering temperatures surface diffusion dominates matter redistribution.

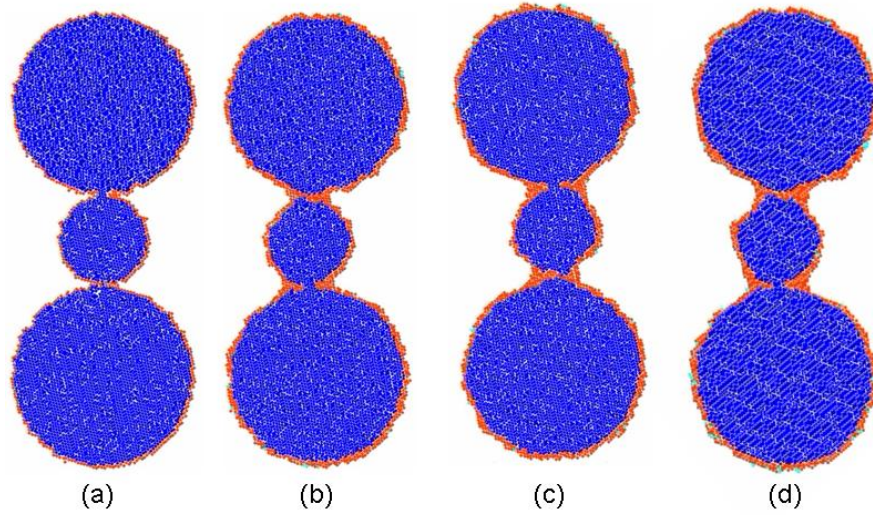


Figure 2.17 MD simulation of one small and two large particles sintering at  $T = 0.19 \text{ } \epsilon/kB$ . (a)  $t = 500t^*$ ; (b)  $t = 50000t^*$ ; (c)  $t = 200000t^*$ ; (d)  $t = 500000t^*$ . See text for the explanation of the colour scheme.

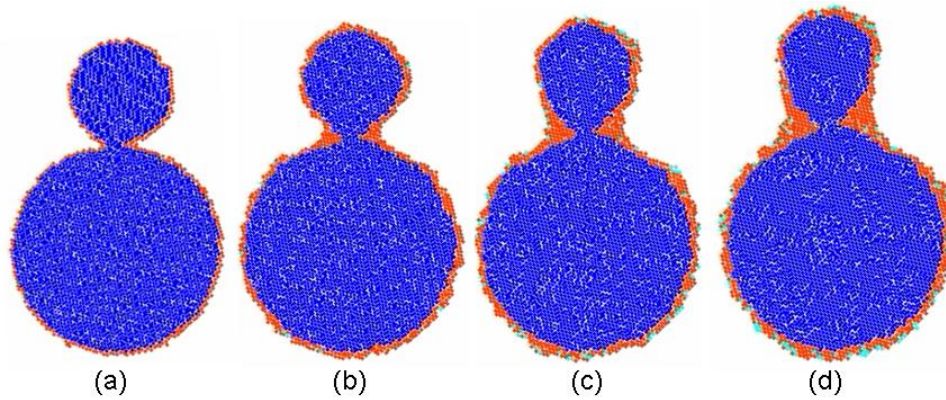


Figure 2.18 MD simulation of a small and a large particle sintering at  $T = 0.19 \text{ } \epsilon/kB$ . (a)  $t = 500t^*$ ; (b)  $t = 50000t^*$ ; (c)  $t = 200000t^*$ ; (d)  $t = 500000t^*$ . See text for the explanation of the colour scheme.

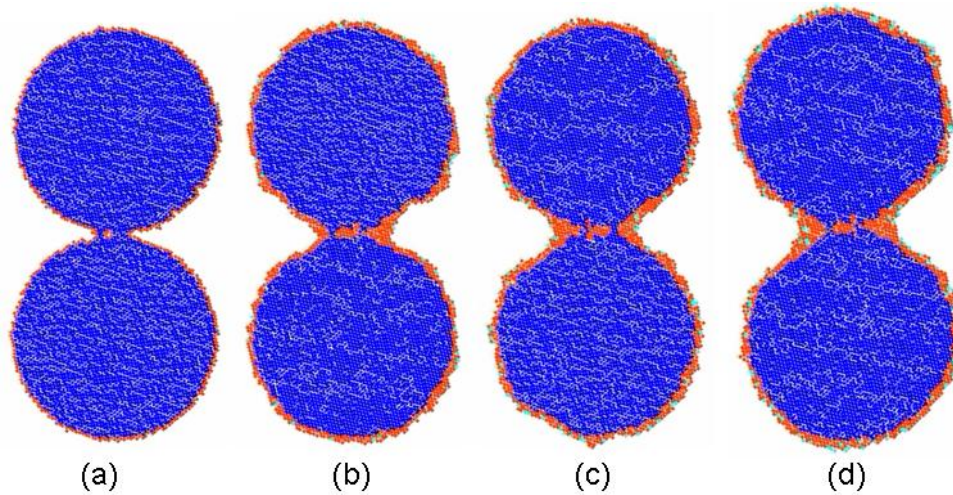


Figure 2.19 MD simulation of two large particles sintering at  $T = 0.19 \text{ } \epsilon/k_B$ . (a)  $t = 500t^*$ ; (b)  $t = 50000t^*$ ; (c)  $t = 200000t^*$ ; (d)  $t = 500000t^*$ . See text for the explanation of the colour scheme.

In all the above cases, there was no GB between the particles in contact. Figure 2.20 shows the case of two same sized particles sintering at  $T = 0.26 \text{ } \epsilon/k_B$  for which a GB is formed between the particles. By  $t = 100t^*$ , a small neck made up of surface atoms has been formed. As sintering proceeds, the neck is filled up dominantly by the red atoms, meaning that these atoms have all been at the particle surface at some stage of the sintering process. The GB was migrating backwards and forwards between the two particles. Figure 2.21 shows the centre-to-centre distance between the two particles as a function of time. It is clear that the particles approach each other during the sintering process, confirming that atoms have been taken away from the GB by the GB diffusion. This can be compared with the case of Figures 2.16 and 2.19 for which there was no GB between the two particles and the distance between the particles remained unchanged. Figure 2.22 shows the neck size as a function of time for the cases showing in Figures 2.16, 2.19 and 2.20. It can be observed that GB diffusion promotes neck size growth.

Faster surface diffusion plus evaporation condensation at higher temperatures are also among the factors promoting faster neck size growth.

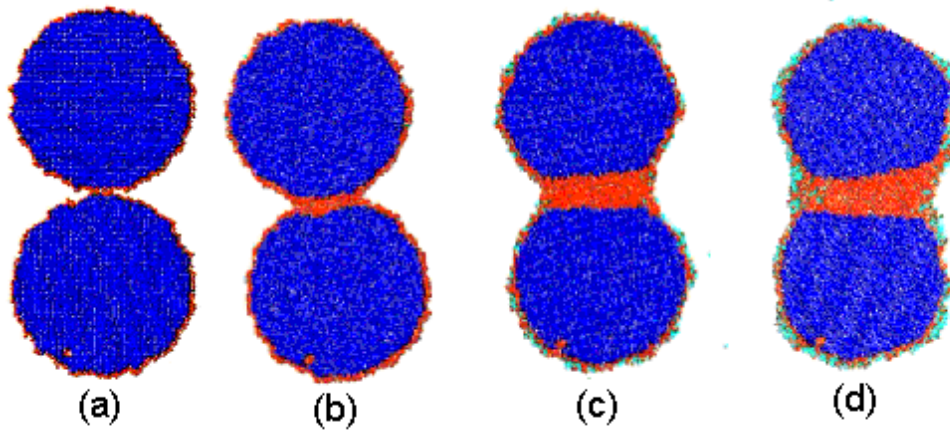


Figure 2.20 MD simulation of two large particles sintering with the GB at  $T = 0.26 \epsilon/k_B$ . (a)  $t = 500t^*$ ; (b)  $t = 50000t^*$ ; (c)  $t = 200000t^*$ ; (d)  $t = 500000t^*$ . See text for the explanation of the colour scheme.

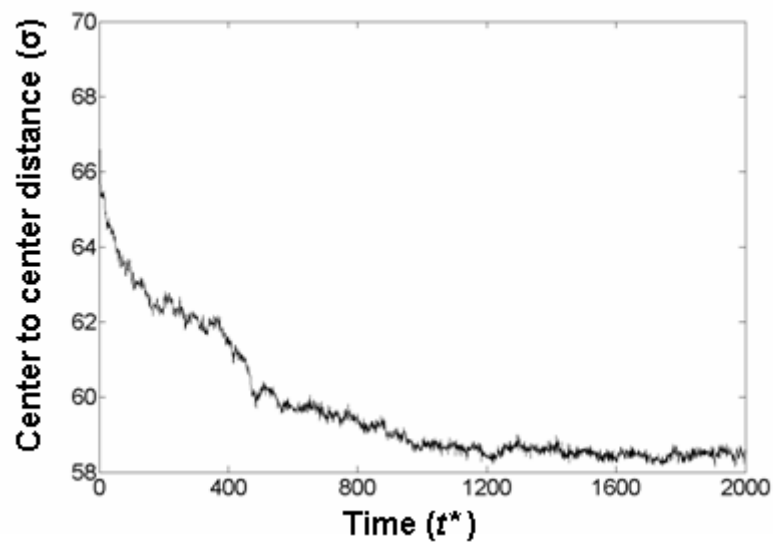


Figure 2.21 Centre-to-centre distance as a function of time for the case shown in Figure 2.20.

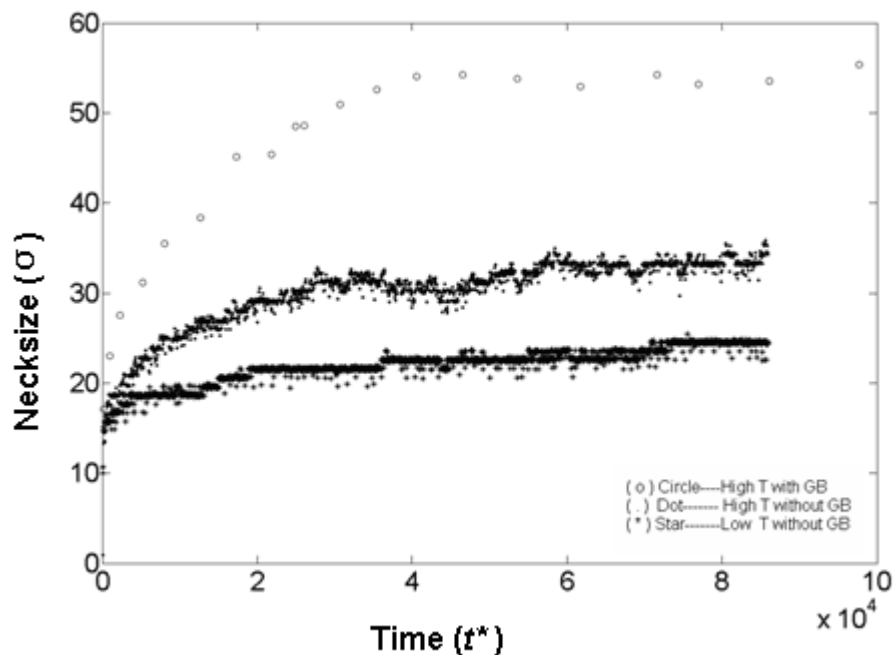


Figure 2.22 Comparison of neck size growth as a function of time for the cases shown in Figures 2.16, 2.19 and 2.20.

Figure 2.23 shows the MD simulation of one small particle in contact with two big neighbours sintering at  $T = 0.26 \epsilon/k_B$ . This is perhaps the most interesting case that demonstrates the difference between the MD model and continuum model. By  $t = 100t^*$  a GB was formed at the upper neck but the initial GB at the lower neck has been eliminated. Then, two very different behaviours of the neck growth can be observed. The upper neck grows by GB diffusion, whereas the lower one grows by surface diffusion. The GB also migrates into the small particle. It is also obvious that the existence of a GB accelerates significantly the neck growth at the upper neck. A continuum model, by contrast, cannot possibly predict such a behaviour because the mechanism of matter transportation has to be assumed rather than predicted by such a model.

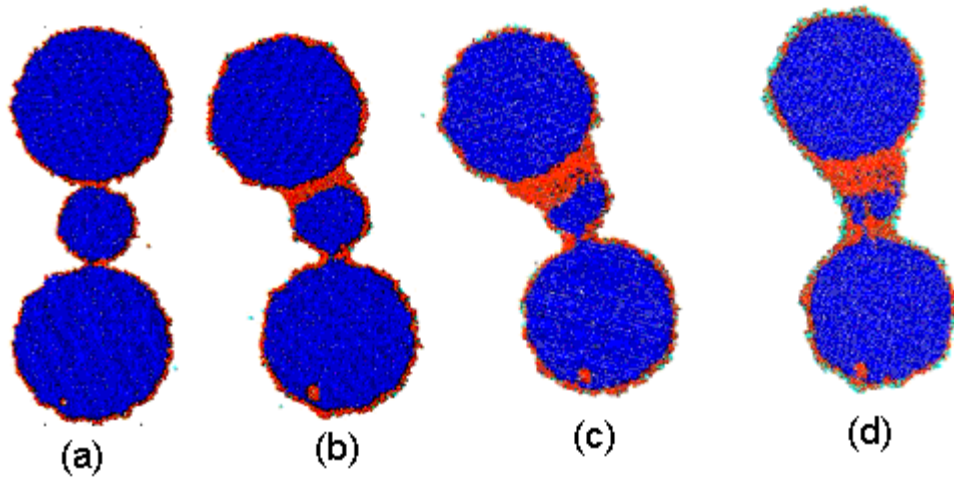


Figure 2.23 MD simulation of one small and two large particles sintering at  $T = 0.26 \epsilon/kB$ . (a)  $t = 500t^*$ ; (b)  $t = 50000t^*$ ; (c)  $t = 200000t^*$ ; (d)  $t = 500000t^*$ . See text for the explanation of the colour scheme.

## 2.7 Conclusions

MD simulations were employed to study fcc nanoparticle interactions. The results are summarised as follows:

1) Three major matter distribution mechanisms were observed to contribute significantly to the early stage sintering of the three different models including:

\* Surface diffusion, which contributes mostly under low temperatures, although it is the general matter distribution mechanism for all models;

\* Vapour diffusion, which contributes to the matter distribution mainly at high temperatures.

\* GB diffusion, which brings about a faster sintering rate if the conditions allow the particles to form a GB. An unusual observation is that the formed GB could disappear between a small particle and a large particle.

2) At the nano-scale, sintering is considerably faster than at the micro-scale. GB diffusion is the dominant factor at high temperatures since it is faster than surface diffusion and vapour diffusion.

3) The initial relative rotation of unconstrained nanoparticles was observed to decrease the misorientation of two particles. This mechanism is important for forming a GB between two particles. Many nanoparticle pairs cannot form a GB but can form a single crystal because of the initial relative rotation.

## **Chapter 3 Computer Simulation of Nanoparticle Sintering Using a 2D Continuum Method**

### ***3.1 Introduction to the continuum model***

As popularly known in computational material science, there is a large difference in time and length scales between different modelling methods. At the opposite ends of the time and length scale spectrum are the atomic simulation and solid mechanics continuum models, each of which is highly developed and reliable modelling method. MD models predict molecular properties based on atomic interactions, whereas computational solid mechanics continuum models predict the macroscopic mechanical behaviour of materials idealised as continuous media based on known bulk material properties. Owing to the unique property of nanostructured material, which is different to macroscopic crystalline materials, many people doubted the extensive use of the continuum model in nano-scale material. Therefore, various models were developed to link these two different scales[22],[23]. In this chapter, the 2D numerical scheme developed by Pan and Cocks[2] is adopted to compare the continuum model with the MD model that is presented in the previous chapter. The model developed by Pan and Cocks was a 3-dimensional model. In order to compare with the 2-dimensional MD simulation, a 2D version of Pan's model is developed and implemented in this project by the author.

The sintering of a ceramic powder is driven by the reduction of the associated total free surface energy, matter flows from both surface diffusion and GB results, resulting in the shrinkage of the pores and densification of the compacted powder. The solid-state diffusion of matter is driven by the gradient of chemical potential of the diffusing

species. This gradient of chemical potential is induced by the gradient of the free surface curvature in the case of surface diffusion and by the gradient of the stress acting normal to the GBs in the case of GB diffusion.[24] When a GB meets a free surface, the two processes are coupled. A given physical problem can often be simplified by first examining two extreme situations: the fast surface diffusion limit and the fast GB diffusion limit. At the extremes of fast surface diffusion, it is assumed that surface diffusion is much faster than boundary diffusion, and matter transported to the pore tip is instantly taken away and distributed along the pore surface. As a result, an equilibrium pore shape is maintained. At the extremes of fast GB diffusion more attention is paid to the evolution of the pore profile, and the GB only acts as a source or sink of matter and as a boundary condition for the chemical potential that links the pore tip curvature with the remote stress. Generally, the continuity conditions at the junctions between pore surfaces and the GB have to be solved to solve the coupled diffusion problem. In this chapter, the numerical finite difference method is employed to solve the coupled diffusion problem.

### ***3.2 A Finite difference model for sintering***

#### **The governing equations**

The solid-state diffusion theory is adopted for the continuum model[25]. According to this theory, the diffusive flux  $j$ , defined as the volume of matter passing across a unit area perpendicular to the flux direction per unit of time, is assumed to be linearly dependent on the gradient of the chemical potential  $\mu$  of the diffusing species:

$$j = -\frac{D\delta}{k_B T} \frac{\partial \mu}{\partial s} \quad (3.1)$$

where  $D$  is the diffusivity,  $\delta$  is the thickness of the layer through which the material diffuses,  $k_B$  is Boltzmann's constant,  $T$  is the absolute temperature and  $s$  is a local coordinate along the diffusion path. A schematic picture of the 2D coupled diffusion model of two-particle sintering is shown in Figure 3.1. GB is assumed to be straight and grains are assumed to be rigid. The GB diffusion and surface diffusion meet at the triple junction point.

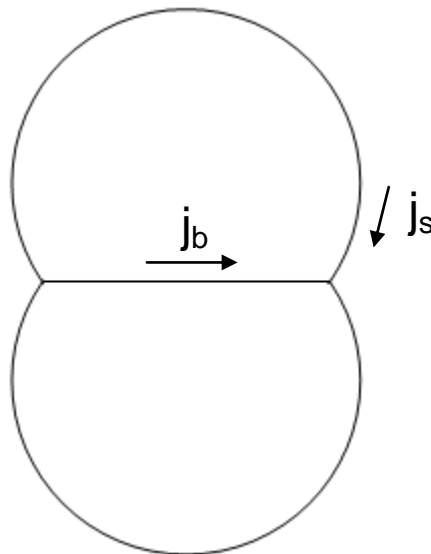


Figure 3.1 The two-dimensional coupled diffusion model for two particles sintering

**GB diffusion**

Along a GB, the gradient of the atomic chemical potential is induced by the gradient of stress  $\sigma$  acting normal to the boundary[26]:

$$\mu = -\Omega\sigma \quad (3.2)$$

where  $\Omega$  is the atomic volume, therefore:

$$j_b = \frac{D_b \delta_b \Omega}{kT} \frac{\partial \sigma}{\partial s} \quad (3.3)$$

where  $D_b$  is the GB diffusivity and  $\delta_b$  is the GB thickness. As matter is deposited onto (or removed from) a GB, the grains on either side of the boundary move with a normal velocity  $v_b$ . Matter conservation requires that:

$$\frac{\partial j_b}{\partial s} + v_b = 0 \quad (3.4)$$

**Surface diffusion**

Along a free surface, the gradient of the atomic chemical potential is induced by the gradient of the free surface curvature[26]:

$$\mu = -\Omega\gamma_s\kappa \quad (3.5)$$

where  $\gamma_s$  is the specific surface energy and  $\kappa$  is the principal surface curvature. It is positive for a concave free surface. So we have:

$$j_s = \frac{D_s \delta_s \Omega \gamma_s}{kT} \frac{\partial \kappa}{\partial s} \quad (3.6)$$

in which  $D_s$  is the free surface diffusivity. As matter is deposited onto (or removed from) a free surface, it migrates with a normal velocity  $v_s$ . Matter conservation requires that:

$$\frac{\partial j_s}{\partial s} + v_s = 0 \quad (3.7)$$

with  $v_s$  assumed to be positive when matter is added to the surface.

### Stress equilibrium

The stress  $\sigma$  acting normal to the GB, together with the free surface tension at the triple point must be in equilibrium; therefore:

$$\int_{GB} \sigma ds + 2\gamma_s \sin \theta = 0 \quad (3.8)$$

where  $\int_{GB} \sigma ds$  integrates the stress over the GB,  $\gamma_s$  is the surface tension and  $\theta$  is the dihedral angle. The dihedral angle is fixed as the equilibrium value since it usually reaches its equilibrium value very fast.[27]

### Continuity

Where a GB meets a free surface, several continuity conditions must be satisfied. Firstly, matter must be conserved at the pore tip:

$$(j_b)_{tip} = -(j_s^+)_{tip} + (j_s^-)_{tip} \quad (3.9)$$

where + and – indicate the two free surfaces joining the GB and sign convention for these local fluxes is defined in Figure 3.2.

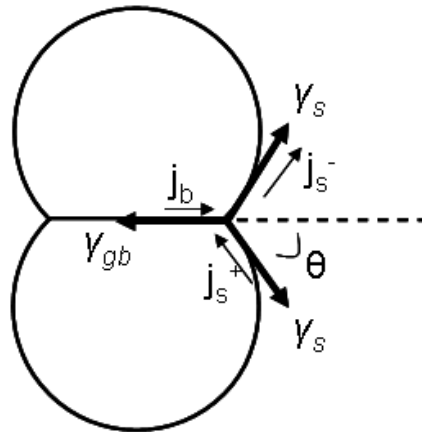


Figure 3.2 Diffusion fluxes and surface and GB tension equilibrium in the 2D coupled diffusion model of two-particle sintering.

Secondly, the surface tension  $\gamma_s$  and grain boundary tension  $\gamma_{gb}$  must be in equilibrium as shown in Figure 3.2. The equilibrium requirement leads to a discontinuity in the tangent of the free surface at the junction, which is often referred to as the dihedral angle  $2\theta$ :

$$\cos \theta = \frac{\gamma_{gb}}{2\gamma_s} \quad (3.10)$$

Finally, the chemical potential must be continuous (otherwise there would be an unbounded flux there). Using equations (3.2) and (3.5), the continuity of the chemical potential can be expressed as:

$$\sigma_{tip} = \gamma_s K_{tip} \quad (3.11)$$

The  $\sigma_{tip}$  is the GB stress at the tip point. However,  $\kappa_{tip}$ , the curvature at the tip point, should not be arbitrarily prescribed. Equation 3.10 implies that there is no curvature at the tip point. Thus,  $\kappa_{tip}$  here is virtual; its purpose is to satisfy the GB and surface coupling Equations 3.11 and surface diffusion Equation 3.6. To obtain the tip curvature, Equations 3.8, 3.9 and 3.11 must be solved together. Once the tip curvature is known, the finite difference method can be employed to update the particle profiles.

### Non-dimensionalisation

Let  $d$  be a characteristic diffusion distance (grain size, for example) and  $\sigma_0$  a suitable reference stress. A reference rate then can be defined as:

$$\dot{\varepsilon}_b = \frac{D_b \delta_b \Omega \sigma_0}{kT d^3} \quad (3.12)$$

which has the dimensions of strain rate, and the governing equations in terms of dimensionless quantities can be written as:

$$\bar{\kappa} = \kappa d, \bar{\sigma} = \sigma / \sigma_0, \bar{j} = j / (\dot{\varepsilon}_b d^2), \bar{v} = v / (\dot{\varepsilon}_b d), \bar{t} = \dot{\varepsilon}_b t \quad (3.13)$$

with any lengths in the physical description scaled by  $d$  the diffusion length. Equations 3.3 and 3.6 then become

$$\bar{j}_b = \frac{\partial \bar{\sigma}}{\partial s} \quad (3.14)$$

and

$$\bar{j}_s = C_s \frac{\partial \bar{k}}{\partial s} \quad (3.15)$$

where

$$C_s = \frac{D_s \delta_s}{D_b \delta_b} \frac{\gamma_s}{\sigma_0 d} = \Theta \overline{\gamma_s} \quad (3.16)$$

i.e.

$$\Theta = \frac{D_s \delta_s}{D_b \delta_b} \quad \text{and} \quad \overline{\gamma_s} = \frac{\gamma_s}{\sigma_0 d} \quad (3.17)$$

Other equations keep their original form in terms of the corresponding non-dimensionalised variables. Three groups of non-dimensionalised material constants come out from the above analysis:  $\Theta$ , which represents the relative importance of the two diffusion processes;  $\gamma_{gb}/\gamma_s$ , which determines the dihedral angle at the pore tip; and  $\gamma_s/\sigma_0 d$ , which represents the relative significance of the surface tension. From now, all the variables used below are non-dimensionalised, even though they do not have a short line above them.

### 3.3 A Finite difference method scheme for sintering

Owing to the symmetrical feature of the continuum model, in our finite difference model, only half of a particle needs to be considered because of the symmetry about both the x and y axes. The surface profile of the particle is discretised into knot points as shown in Figure 3.3. The total number of dots is around 1800, which is big enough to maintain the accuracy of the surface profile. We will refer to these points defining the surface profile as P-points. The first P-point is regarded as the pore tip point. A tiny initial neck size is assigned to solve the first step equations, and the dihedral angle  $\theta$  is maintained during the whole process of simulation. The curvature  $\kappa$  and the centre of the surface at a P-point are determined by constructing a circle through the P-point and its two neighbouring P-points. For a given surface profile, expressed in terms of the P-point coordinates, the curvature is known at all P-points except at the pore tips where the curvature is not defined. A point bisecting two neighbouring P-points is referred to as a B-point. The matter flux  $j_s$  along the surface across a B-point can be determined according to Equation 3.18:

$$j_{s,ib} = C_s \frac{(\kappa_{ib,+p} - \kappa_{ib,-p})}{\Delta s_{ib}} \quad (3.18)$$

except for the point next to the pore tips, where  $\kappa_{ib,+p}$  and  $\kappa_{ib,-p}$  are the curvatures of the two P-points neighbouring the  $i$ th B-point, and  $\Delta s_{ib}$  represents the distances between these two neighbouring P-points. The normal velocity of the pore surface at any P-point can then be determined according to:

$$v_{s,ip} = - \frac{j_{s,ip,+B} - j_{s,ip,-B}}{\Delta s_{ip}} \quad (3.19)$$

except for the pore tip and the P-points next to the pore tip. Here,  $j_{s,ip,+B}$  and  $j_{s,ip,-B}$  are fluxes across the two B-points neighbouring the P-point and  $\Delta s_{ip}$  is the mean of the distances between the  $i$ th P-point and its two neighbouring P-points. The direction of  $v_s$  is determined by the centre of the curvature of the P-point and its two neighbouring P-points. From the resulting values of  $v_s$  and their directions, the surface profile can be updated by using a suitable time integration scheme. However,  $v_s$  at the pore tips and their immediate neighbouring P-points cannot be determined without considering the boundary diffusion part of the problem.

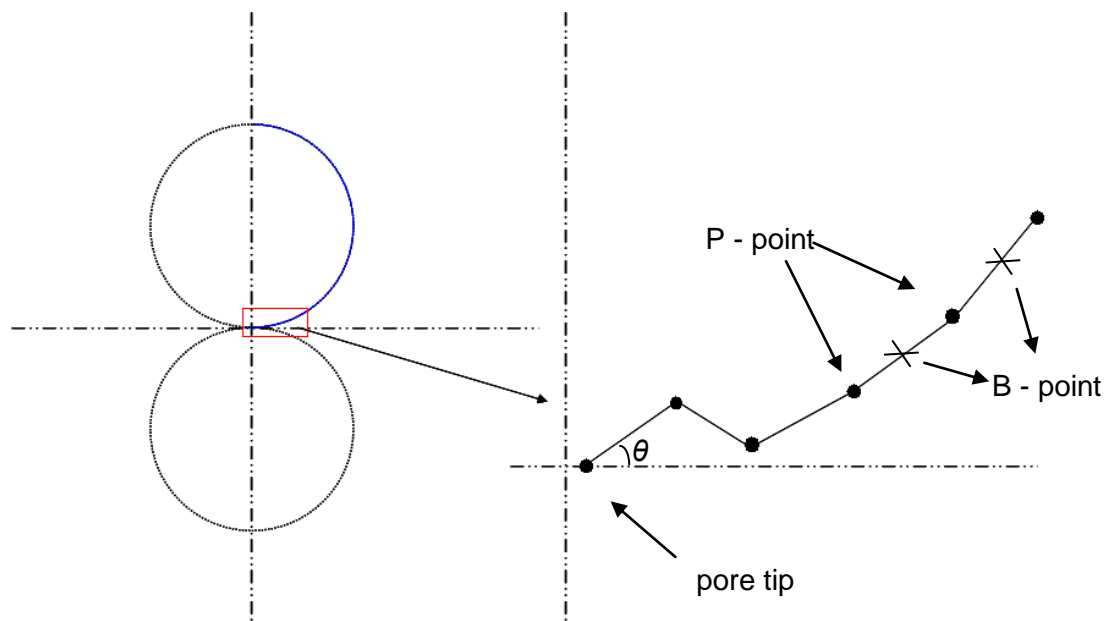


Figure 3.3 Initial configuration of finite difference model of two particles sintering

### 3.4 Coupling between surface and boundary diffusion

Where surface meets grain boundary, matter conservation requires that the amount of material deposited onto the surface between the tip of the P-point and the neighbouring B-points is equal to the amount flowing into this region (so the distance between the tip of the P-point and the next B-point is only  $\Delta s_1 / 2$ , such that

$$j_{b,tip} + j_{s,1} = v_{s,2} \frac{\Delta s_1}{2} \quad (3.20)$$

where  $\Delta s_1$  is the distance between the pore tip and the neighbouring P-point. As mentioned above, the imaginary pore tip curvature  $\kappa_{tip}$  is unknown. The matter fluxes across the B-point next to the pore tip are given by

$$j_{s,1} = C_s \frac{\kappa_2 - \kappa_{tip}}{\Delta s_1} \quad (3.21)$$

in which  $\kappa_2$  is known. Thus, the velocities of the P-point next to the pore tip are given by

$$v_{s,2} = -2 \frac{j_{s,2} - j_{s,1}}{\Delta s_1 + \Delta s_2} \quad (3.22)$$

in which  $j_{s,2}$  is known.

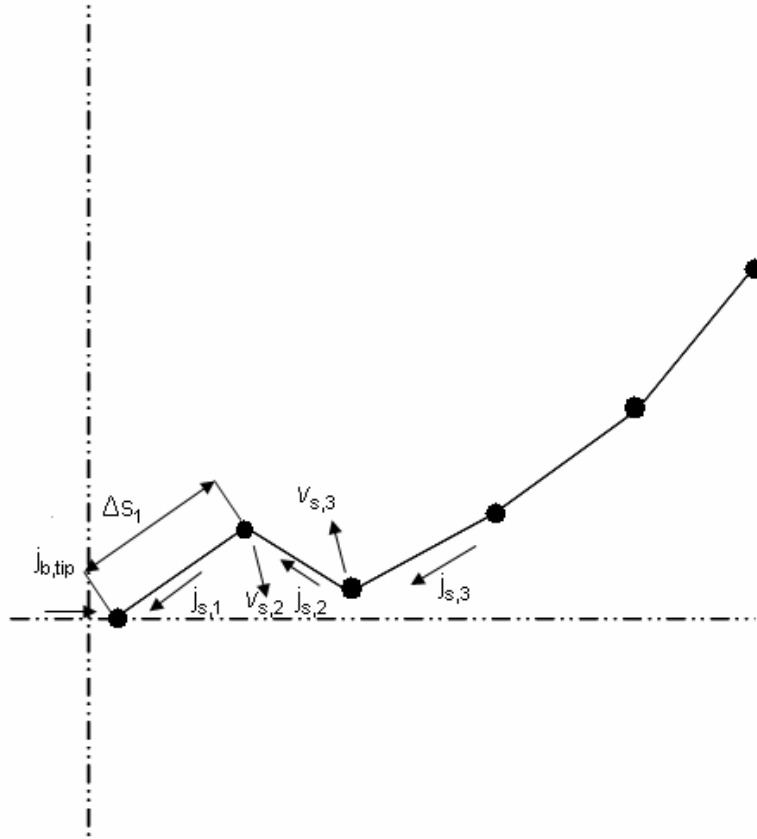


Figure 3.4 Coupling between surface diffusion and GB diffusion.

Next we combine the chemical potential continuity equation 3.11 at the tip point, which could be rewritten with matter flux equations 3.3 and 3.4 as:

$$\gamma_s \kappa_{tip} = \sigma_{tip} = -\frac{1}{2} v_{gb} s^2 + C \quad (3.23)$$

in which  $v_{gb}$  is the unknown GB moving velocity,  $s$  is the neck radius,  $C$  is also an unknown constant produced during equation integration with the stress equilibrium equation 3.8 over the GB, which could also be rewritten with equations 3.23 as:

$$\int_0^s \left( -\frac{1}{2} v_{gb} s^2 + C \right) ds = \gamma_s \sin \theta \quad (3.24)$$

in which  $\theta$  is the dihedral angle.

The unknown pore tip curvature  $\kappa_{tip}$ , the GB moving velocity  $v_{gb}$  and the matter fluxes across the B-point next to the pore tip  $j_{s,1}$ , the velocity of the pore tip,  $v_{tip}$  and the velocity of the P-point next to the tip  $v_{s,2}$  can all be solved by solving equations 3.21, 3.22, 3.23 and 3.24 which represent three conditions: mass conservation, stress equilibrium over the GB and the continuity of the chemical potential at the pore tip. Once the velocities of every P-point are known (through the combination of the surface velocity  $v_s$  with the same direction of the surface curvature and the GB velocity  $v_{gb}$  with the direction normal to the GB), we can upgrade the surface profile by using a suitable time integration scheme.

### 3.5 Updating the profile of the particle

The direct Euler's method is used to perform the time integration of the pore profile:

$$x_i(t + \Delta t) = x_i(t) + v_{is} n_{ix} \Delta t \quad (3.25)$$

$$y_i(t + \Delta t) = y_i(t) + v_{is} n_{iy} \Delta t + v_{gb} \Delta t \quad (3.26)$$

where  $x_i$  and  $y_i$  are P-point coordinates,  $v_{is}$  is the P-point surface velocity,  $n_{ix}$  and  $n_{iy}$  are the P-point normals,  $v_{gb}$  is the GB velocity and  $\Delta t$  is the time step. The time step  $\Delta t$  is determined from the maximum surface velocity  $v_{smax}$  experienced by the P-point at the current time step, such that the displacement increment because of  $\Delta t$  and  $v_{smax}$  is kept constant for all time step increments. If we define the mean distance between all the neighbouring P-points of the initial profile as  $d_{mean}$ , then this constant displacement increment can be set to a prescribed percentage,  $\varepsilon_t$ , of  $d_{mean}$ :

$$\Delta t = \frac{\varepsilon_t d_{mean}}{v_{smax}} \quad (3.27)$$

### 3.6 Results and discussion

From the MD simulations of the two-particle interaction, surface diffusion dominates the matter distribution process in the case of GB elimination and low temperatures, and GB diffusion dominates the matter distribution when the GB is formed at high temperatures. Therefore, in this 2D continuum simulation two extreme matter distribution limits of the surface diffusion and GB diffusion processes are also investigated.

To obtain the neck growth rate of the GB diffusion-dominated sintering process, the following material constants and parameters were used:  $D_s \delta_s / D_{gb} \delta_{gb} = 0.001$  ,  $\gamma_{gb} / (2\gamma_s) = 0.5$  ,  $\gamma_s / (d\sigma_0) = 0.01$  and  $\varepsilon_t = 0.0001$  . As can be seen from  $D_s \delta_s / D_{gb} \delta_{gb} = 0.001$  , the GB diffusion coefficient is much bigger than that of the surface diffusion, which suggests that the whole process will be dominated by GB diffusion.

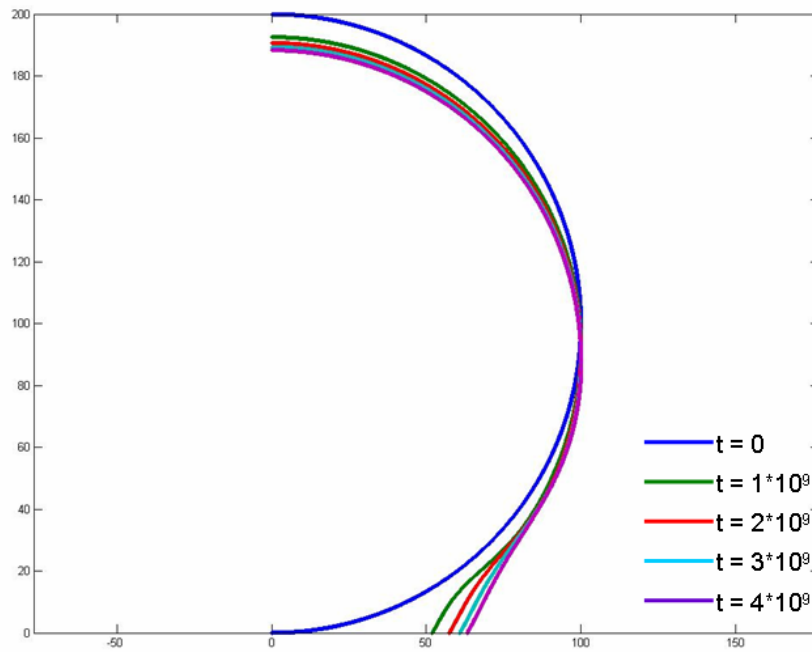


Figure 3.5 Sintering of two identical particles dominated by GB diffusion.

Figure 3.5 shows a quarter of the evolution of geometry for the two identical sintering particles controlled by GB diffusion. Initially, the diffusion distance is short because material flowing from the neck quickly deposits on the neck surface. Because of the matter diffusing out of the GB, the two particles also approach each other. These phenomena are typical of the GB diffusion-controlled sintering process.

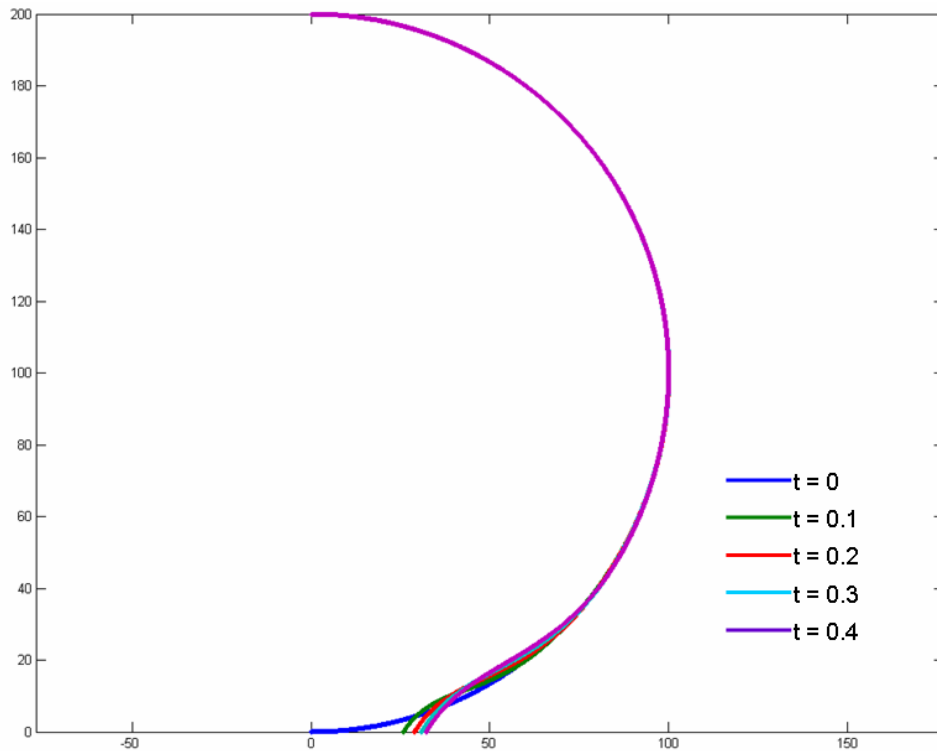


Figure 3.6 Sintering of two identical particles dominated by surface diffusion.

Figure 3.6 shows a quarter of the evolution of geometry for the two identical sintering particles controlled by surface diffusion. The initial fast neck filling was driven by the matter distributed from the high curvature surface, which is close to the neck. Because there is no matter diffusing out of the GB, the two particles are not moving towards each other. These phenomena are typical of the surface diffusion-controlled sintering process.

### ***3.7 Comparison between MD and continuum simulations for 2D nanoparticle sintering***

The most interesting outcome of the MD simulations presented so far is that asking whether an MD model agrees with a continuum model is the wrong question. For

nanoparticles, the sintering behaviour observed in an MD simulation is beyond the predictability of the continuum model. If the assumed mechanism of matter redistribution in the continuum model did occur in an MD simulation, it would be interesting to see if the two models could predict the same neck growth. Figure 3.7 compares the neck sizes as functions of time predicted by the continuum and MD models, respectively. The case is for two particles of the same size of  $R=70\sigma$  sintering at  $T=0.19 \varepsilon/k_B$ , which is controlled by surface diffusion. Log scales are used for both axes. The straight line was obtained from the continuum model, whereas the discrete dots were obtained from several repeated MD simulations of the same problem. Figure 3.8 shows a similar comparison where GB diffusion is the controlling mechanism of matter redistribution. The sintering temperature was set as  $T=0.26 \varepsilon/k_B$ . All the other parameters are the same as those in Figure 3.7. The MD prediction is smoother in Figure 3.8 than in Figure 3.7 because the neck size was obtained manually from a single MD simulation picture. It is remarkable to see that the continuum model agrees with the MD model for particles of only around 8000 atoms.

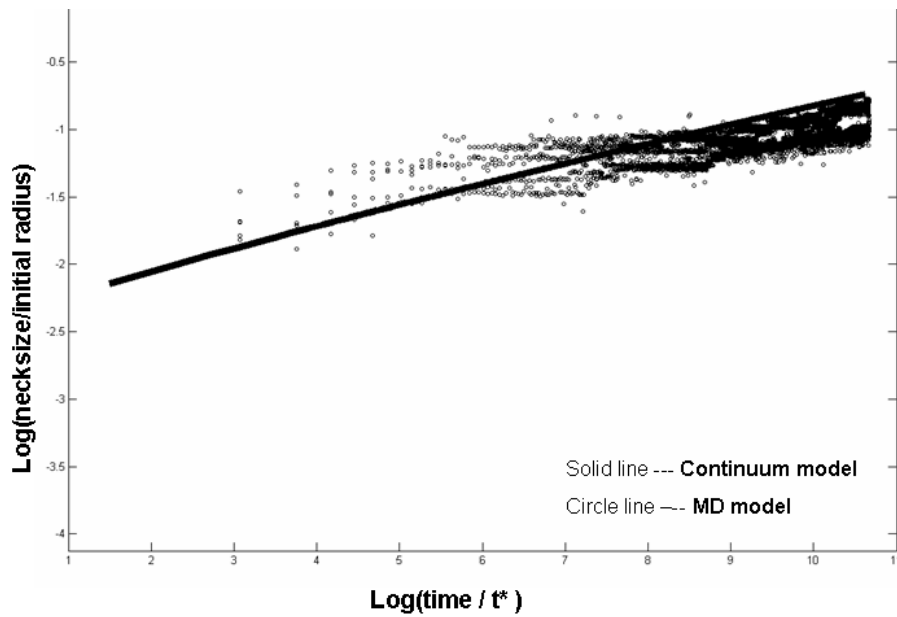


Figure 3.7 Neck size divided by initial particle radius as a function of time predicted by the MD model (discrete dots) and continuum model (solid line) for the sintering of two particles of the same size, each consisting of 5000 atoms at  $T = 0.19\epsilon/k_B$ . Surface diffusion is the dominant mechanism for matter redistribution. Logarithmic scales are used for both axes.

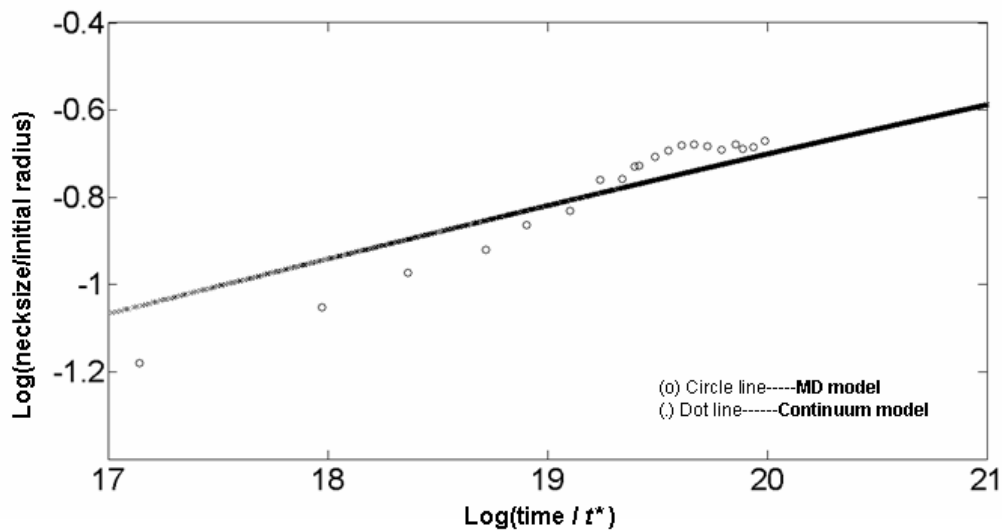


Figure 3.8 Neck size divided by initial particle radius as a function of time predicted by the MD model (discrete dots) and continuum model (solid line) for the sintering of two particles of the same size, each consisting of 5000 atoms, at  $T = 0.26\epsilon/k_B$ . Grain-boundary diffusion is the dominant mechanism for matter redistribution. Logarithmic scales are used for both axes.

### ***3.8 Conclusions of the study of nanoparticle sintering***

It is inappropriate to use continuum models to predict the sintering behaviour of nanoparticles. This is not because the continuum theory of solid-state physics does not apply at this scale, but because nanoparticles behave in so many different scenarios of the continuum theory that one has to predict these scenarios using the MD model. In our MD simulation, it is observed that the particles can reorient themselves to match their crystalline orientations at the beginning of the sintering and thereby form different types of necks between different particles (either with or without the GB). This leads to different mechanisms of matter redistribution at the different necks. It has also been observed that the particles switch the mechanism of matter transportation halfway through the sintering process. None of these can be handled by the continuum model. However, assuming the right scenario, the continuum theory does agree with the MD simulation for particles consisting of just a few thousand atoms.

## **Chapter 4 Multi-scale MD Simulations of Behaviour of Bamboo-like Nanowires at Elevated Temperatures**

### ***4.1 Introduction to Nanowires***

Semiconductor and metallic nanowires are considered important building blocks for future microsystems. The use of nanowires both as passive interconnects and active components of electronic and electromechanical devices, such as gas sensors, transistors or nano-springs[28], demands a thorough understanding of their structures and mechanical properties. The unusual functional properties of nanowires are because of their small diameters, which generate large surface effects because of their large surface-to-volume ratios. The surface stress-induced intrinsic stress in the wire, on the order of gigapascals, leads to NW(nanowire) mechanical properties quite different from the bulk. However, there is also the danger of morphological instability at elevated temperatures, at which diffusion mobility of the atoms becomes important. It is well established that semiconductor nanowires[28] and thin submicrometer metallic filaments in fibrous *in situ* metal matrix composites[29] can break up into isolated particles. Although semiconductor nanowires are usually grown as single crystals, metallic nanowires are often polycrystalline and contain GBs transversing the nanowire normal to its axis (bamboo microstructure). Similar microstructures with transverse heterophase boundaries are also obtained in longitudinal heterostructured semiconductor nanowires produced by switching between different materials during growth[30]. Bamboo-like polycrystalline structures have been well investigated with continuum models using solid matter diffusion theory[31]. However, using the continuum model in nano-regions is always questionable. In this regard, atomistic

simulation is a useful tool to explore polycrystalline nanowire properties at the nano-scale and validate the use of continuum models in nano-regions.

#### 4.2 Understanding the evolution of conventional bamboo-like polycrystalline fibres via the continuum model

A continuum model due to Suo[31] using a variational approach to describe the evolution of bamboo-like polycrystalline fibres is briefly introduced here to compare our MD model with the continuum model. This model is based on a global view that regards evolution as a means to reduce the total free energy.

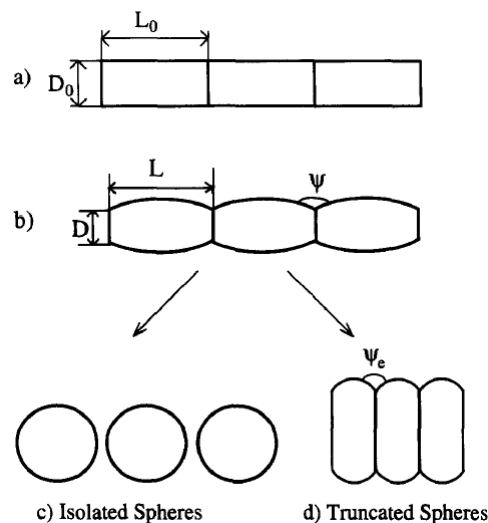


Figure 4.1 (a) The initial array of cylinder-shaped grains. (b) An array of barrel-shaped grains approximates an intermediate, non-equilibrium state. (c) Grains pinch off and spheroidise, approaching an equilibrium state, a row of isolated spheres. (d) The array shrinks as atoms diffuse out from the GBs and plate onto the free surfaces, approaching another equilibrium state, a touching array of truncated spheres. Taken from Suo[31].

The polycrystalline fibre is represented in this model by a row of identical grains, initially cylindrical in shape of length  $L_0$  and diameter  $D_0$  and connected at their ends (Figure 4.1 a). When heated, the grains change shape and are assumed to remain

identical to one another (Figure 4.1 b). In real experimental observations, the evolution of a polycrystalline fibre after heat treatment goes in two different directions: isolated spheres (Figure 4.1 c) and truncated spheres (Figure 4.1 d).[32] These observations are also found in this continuum model. In this model, the total free energy is the sum of total surface energy and total GB energy. The driving force of a grain's shape change is the reduction in total free energy. The matter distribution process of this shape change is operated by surface diffusion and GB diffusion. In Figure 4.1 b, three parameters are necessary to describe this bamboo structure: grain length  $L$ , diameter  $D$  and dihedral angle  $\psi$ . This free energy function determined by two coordinates is pictured as a surface in a 3D space. Figure 4.2 shows the energy landscape for  $L_0/D_0 = 2.5$  and  $\psi_e = 150^\circ$ . A point on the surface represents a non-equilibrium state in general, and the bottom of a valley represents an equilibrium state with lowest free energy. Thermodynamics requires that an evolution path be a curve on the surface, descending from the initial state to the bottom of a valley. The upper left corner of the surface terminates when the grains pinch off. Three special states are indicated on the landscape: the initial cylinders, isolated spheres and truncated spheres. The isolated spheres case does not have the lowest free energy. Thermodynamics by itself should not be the only factor determining the evolution path and final equilibrium state.

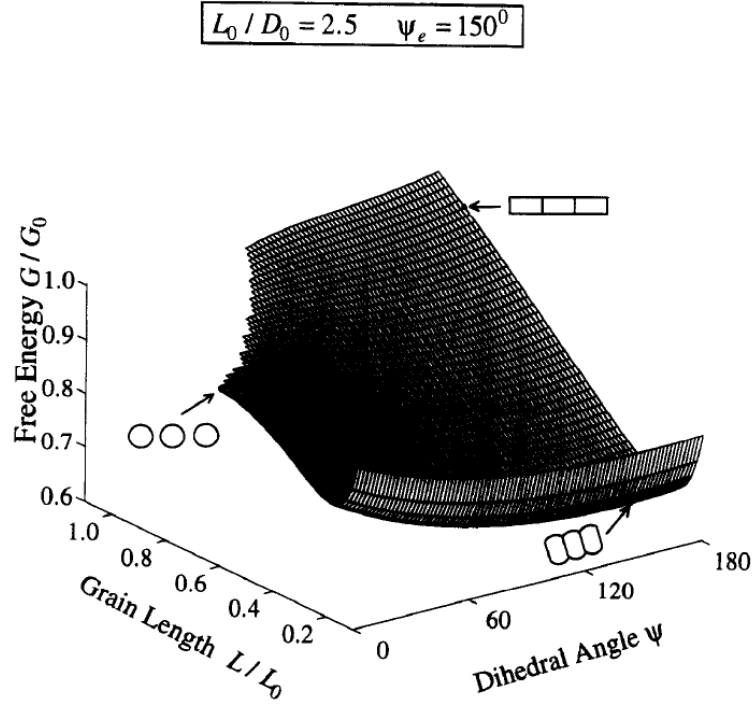


Figure 4.2 Energy landscape. The free energy is a function of the generalised coordinates, represented as a surface in the thermodynamic space. A point on the surface represents a state, generally not in equilibrium. Three special states are indicated on the surface: the initial cylinders, isolated spheres and truncated spheres. Taken from Suo[31].

The continuum model by Suo[31] is based on the so-called variational principle. The surface and GB fluxes  $j_s$  and  $j_b$ , together with suitable velocities, constitute a virtual motion.  $\dot{G}(j_s, j_b)$  is the associated energy rate. The free energy decreases associated with an atom moving unit distance on the surface and GB are defined as force  $F_s$  and  $F_b$ :

$$\dot{G}(j_s, j_b) + \int F_s j_s dA + \int F_b j_b dA = 0 \quad (4.1)$$

Combining the above equation with empirical flux law:

$$j_s = M_s F_s \quad (4.2)$$

$$j_b = M_b F_b \quad (4.3)$$

in which  $M_s$  and  $M_b$  are the surface diffusion mobility and GB diffusion mobility, respectively. With the introduction of the mobility concept, the kinetics is another important factor to influence the grain evolution process.

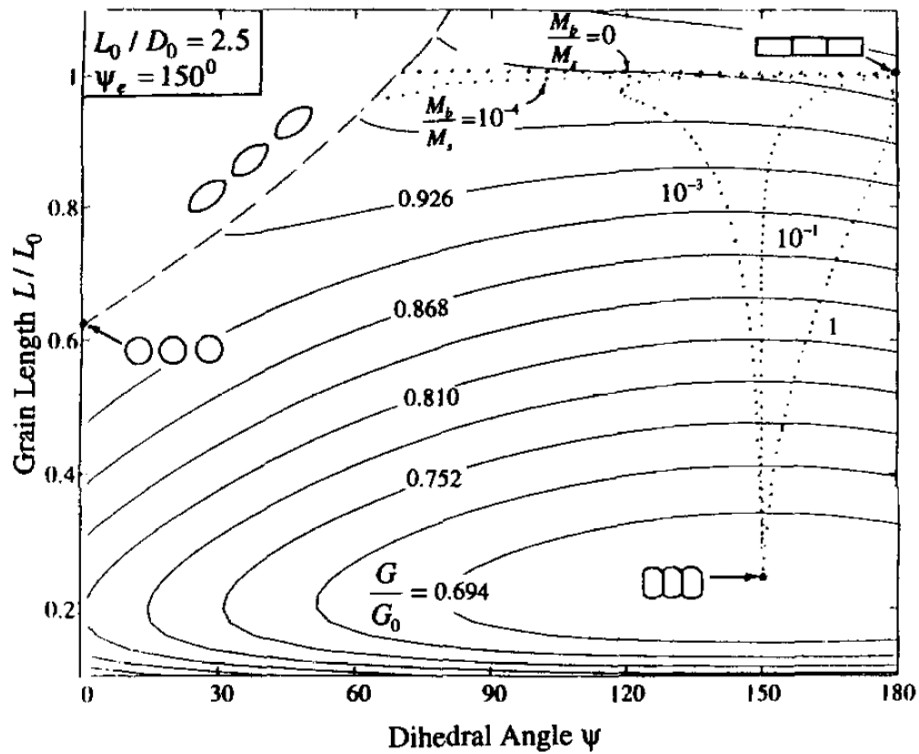


Figure 4.3 The solid lines are the energy contours and the dotted lines are the evolution path when the grains are connected. The dashed line is the evolution path after the grains pinch off. Taken from Suo[31].

Figure 4.3 shows the plane of the generalised coordinates,  $L/L_0$  and  $\psi$ . Indicated are the three special states: the initial cylinders, isolated spheres and truncated spheres. The solid lines are the energy contours, each being the intersection of the energy landscape in Figure 4.3 and a plane parallel to the coordinate plane. One can read approximately the energy levels of the three special states. After the grains pinch off, they are represented by the dashed line in the upper left corner.

The dotted lines are the evolution paths for various mobility ratios  $M_b/M_S$ . When the GB mobility is vanishingly small,  $M_b/M_S = 0$ , the grain length remains constant, whereas for the surface grooves the grains pinch off and spheroidise, approaching a row of isolated spheres. The mobility ratio  $M_b/M_S = 10^{-4}$  allows some grain shrinkage, but does not alter the destination. Increasing the mobility ratio to  $M_b/M_S = 10^{-3}$  allows the grains to shrink to the state of truncated spheres. Consequently, everything else being fixed, a critical GB mobility exists, above which the grains shrink to the lowest energy state, namely the truncated spheres. In conclusion, the evolution path depends on both energetics and kinetics.

### **4.3 A Multi-scale MD scheme**

The mechanical deformation and failure of many engineering materials are inherently multi-scale phenomena that occur on many different length and timescales. Nanometre-scale defects such as GBs, impurities, voids, crack tips and vacancies correspond to specific atomic configurations involving many atoms, and they can also be viewed as individual mechanical entities with specific properties. The deformation fields associated with these defects lead to defect interactions at even larger scales (from

nanometres to many microns) such as dislocation patterning, crack tip shielding by dislocations and solute hardening. These phenomena are often controlled by long-range fields that do not require a fully atomistic description of the defect core. Models that allow for the simultaneous, mechanically coupled simulation of an atomistic and a continuum region are multi-scale models; atomistic phenomena are properly described where necessary, whereas continuum mechanics approaches in surrounding regions are used to significantly reduce the computational burden without compromising accuracy. The coupling of atomistic and continuum models has been an active area of research in recent years. The objective of such coupling is to maintain atomistic resolution in critical regions of a material while coarse-graining the surrounding regions in a manner that preserves the elastic response of the surrounding material and avoids any artificial forces due to interface coupling.

For our polycrystalline bamboo nano-fibre evolution model at elevated temperatures, the whole process is dominated by the GB diffusion and the surface diffusion close to the GB. Thus, it is unnecessary to model all the atoms that are far from the GB. For this reason, a coarse grain model that keeps the far atoms rigid as a whole block is proposed. However, this rigid block could move along with elastic force generated by the free atomic field. This model is mainly based on Qu's[33] 'stadium' damping theory, which will be elaborated below. This model could effectively handle both dynamic wave propagation and finite temperature dynamics within a coupled atomistic/coarse grain region.

### 4.3.1 The details of the multi-scale MD scheme

A classical 3D LJ model is still adopted here for the free atoms region and interface between free atoms and coarse-grained rigid parts. The pairwise LJ potential is still used in this simulation. To speed up the simulation and avoid the self-interaction of particles in simulation with the PBCs, the long “tail” of the LJ potential interaction is truncated as described in the previous chapter. The classical Newton equations of motion are integrated using the leap frog method. The appropriate time step of  $0.02 \sigma(m/\varepsilon)^{1/2}$ , where  $m$  is the atom mass, is used to guarantee the stable numerical integration of the equations of motion. An example of the starting configurations is shown in Figure 4.4.

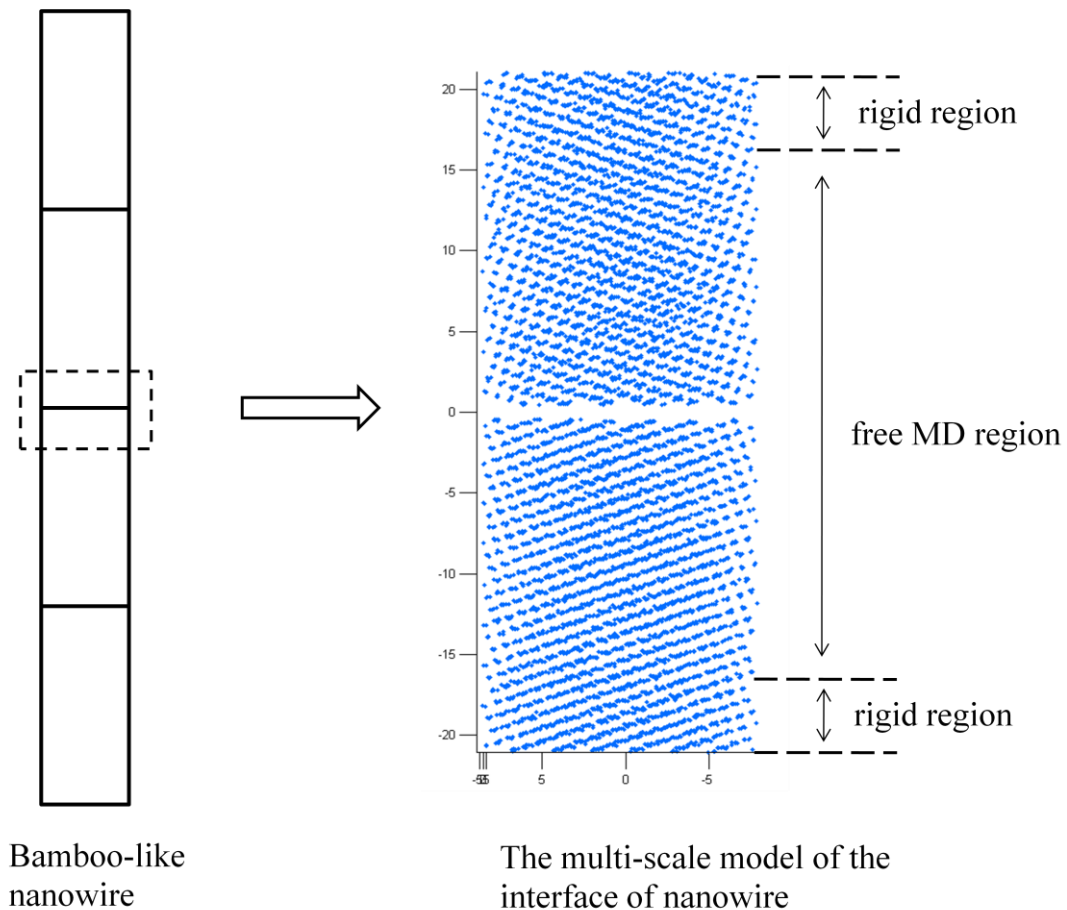


Figure 4.4 The initial configuration of the MD model of the bamboo-like nanowire.

Figure 4.4 shows that the upper grain and lower grain have different crystallographic orientations in order to investigate the effect of the crystallographic orientation. The gap between them is about  $1.5\sigma$ . Before the two grains are placed in contact with each other, each grain is well-equilibrated to obtain the correct bulk and surface density at a certain constant temperature. The constant temperature is realised using the Langevin thermostat described below. To prevent the loss of any vapour atoms from the system, PBCs are also employed, so that a vapour atom leaving the simulation cell through the boundary is reintroduced into the cell with the same velocity at the opposite boundary. The size of the simulation cell is large enough to prevent atoms on the particles interacting with their neighbouring images except for the vapour atoms. The initial total

linear and angular momentums are also removed by removing the linear ( $\sum v_i / N$ ) and angular ( $\omega \times r_i$ ) components of the velocities ( $v_i^{new} = v_i^{old} - \sum_j v_j^{old} / N - \omega \times r_i$ ). [34]

Both the top part of upper grain and bottom part of lower grain are regarded as the rigid coarse-grained continuum part. All the atoms in this region are not allowed to move relative to each other; they are only allowed to move as a whole block if necessary. Their width in the z-direction is slightly wider than the atom–atom cut-off interaction range ( $2.5 \sigma$ ) to make sure the free atoms fully interact. The middle part is the free atom region. In this region, a stadium damping MD is adopted [33]. This stadium model is elaborated below.

To thermostat the atoms and simultaneously absorb waves effectively and efficiently, a Langevin thermostat based on a fluctuation–dissipation thermostat is used [35],[36]. The atoms inside the atom/continuum interface band (Figure 4.5) are given random forces and are artificially damped at each time step so that the equation of motion for an atom is given by

$$\ddot{x} = \frac{F}{m} - \gamma \dot{x} + \sigma \frac{F_A}{m} \quad (4.5)$$

where  $\gamma$  is the applied damping and  $\sigma$  is a random number,  $-1 \ll \sigma \ll 1$ . For each dimension, the component of the random force  $F_A$  is:

$$F_{Ai} = \sqrt{\frac{6\gamma mkT_0}{\Delta t}}, \quad i = x, y, z, \quad (4.6)$$

where  $\Delta t$  is the size of the time step. Furthermore, the applied damping  $\gamma$  is a function of its position relative to the atomistic/continuum interface, decreasing linearly with an increasing distance from the interface as:

$$\gamma = \gamma_{\max} \left(1 - \frac{r(z)}{w}\right) \quad \text{for } r(z) < w, \text{ and } \gamma = 0 \quad \text{for } r(z) \geq w. \quad (4.7)$$

where  $\gamma_{\max}$  is the maximum damping determined from literature[33],  $w$  is the width of the damped ‘stadium’ region and  $r(z)$  is the distance from the atom to the atom/continuum boundary (here in the  $z$ -direction). Thus, the damping coefficient varies linearly from zero at the interface of the damping atom region and free atom region to a value of  $\gamma_{\max}$  at the atom/continuum boundary (Figure 4.5).

In addition, a wall potential is also introduced at the atom/continuum boundary, which is used to stop the free atoms jumping into rigid region via surface diffusion or vapour diffusion. The wall potential equation is:

$$W = e^{(z_i - z_w)/\alpha} \quad (4.8)$$

where  $W$  is the wall potential,  $z_i$  and  $z_w$  are the atom’s  $z$  coordinate and the wall’s  $z$  coordinate and  $\alpha$  is about 0.5 with which the wall potential will not affect the free bulk atoms.

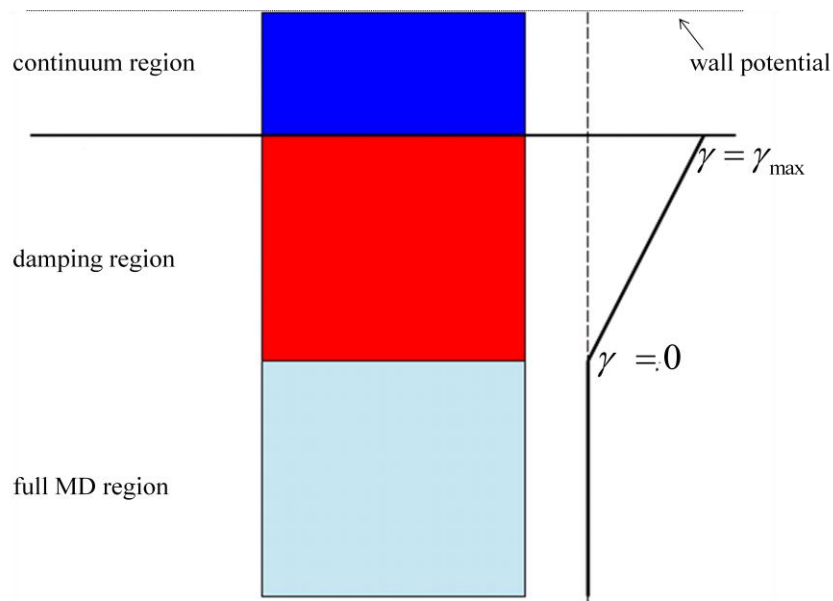


Figure 4.5 Schematic of the finite temperature dynamic coupled atomistic/continuum simulation model for a single grain, which is the upper half of a bamboo model. The lower half is symmetrical to this one.

#### 4.4 Modelling bamboo-like nanowires

It is commonly known that GBs are classified into two different classes: low angle and high angle according to differences in the grain's crystallographic orientation degree. A grain's crystallographic orientation degree difference below about  $11^\circ$  is usually recognised as low angle GB and high angle GB otherwise. Low angle and high angle GB energy and diffusion coefficients differ largely from each other. In our bamboo MD model, low angle and high angle GBs are investigated by setting different grain crystallographic orientations. Two different grain orientations are studied:  $8^\circ$  low angle tilt GB and  $36.9^\circ$  high angle tilt GB at  $\langle 100 \rangle$  direction, which is typical for experimental observations[37] and computer simulations.[38] To investigate the size effect, two different nanowire diameters are also set:  $16\sigma$  and  $12\sigma$  in the reduced unit,

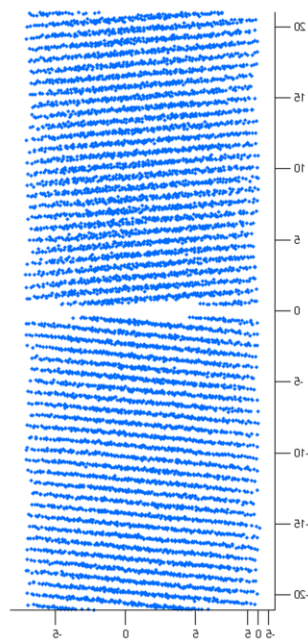
which is about 7 and 5 nm, respectively. For simplicity, these  $16\sigma$  and  $12\sigma$  nanowire diameters are referred to as nanowires with small and large diameters or radii. Therefore, four different models are considered:

Model I: Low angle GB bamboo-like nanowires with a large radius (Figure 4.6);

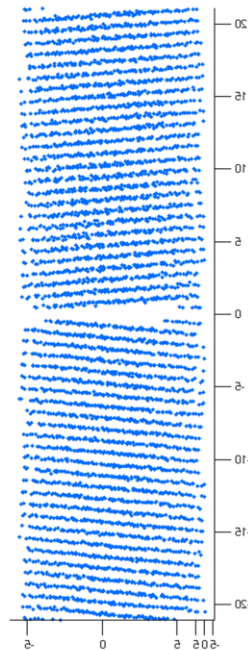
Model II: Low angle GB bamboo-like nanowires with a small radius (Figure 4.6);

Model III: High angle GB bamboo-like nanowires with a large radius (Figure 4.6);

Model IV: High angle GB bamboo-like nanowires with a small radius (Figure 4.6).



Model I



Model II

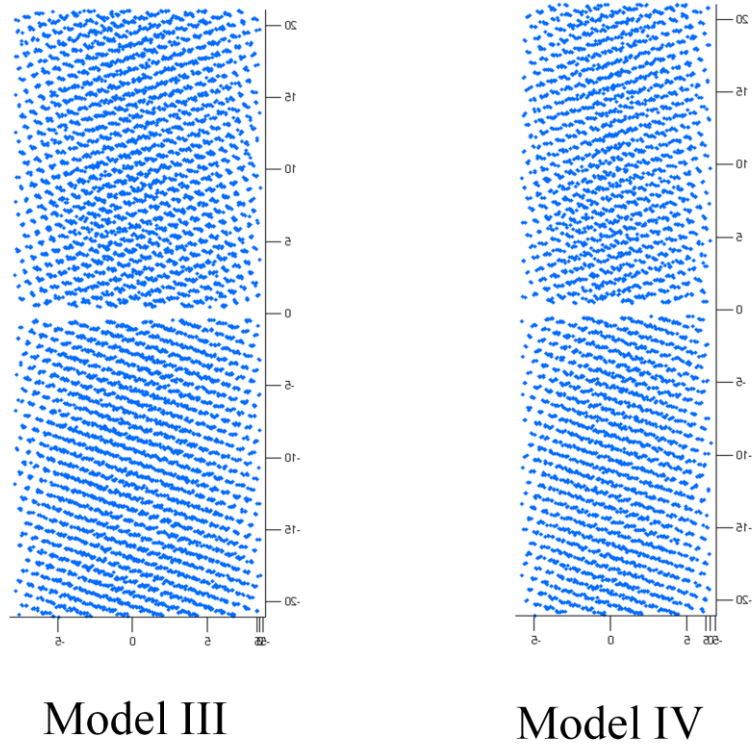


Figure 4.6 Four different models of bamboo-like nanowires.

The GB tilt plane is on the z-x plane (Figure 4.7). The crystallographic orientation is fully aligned on the z-y plane. The observation of the evolution process of detailed GBs in nanowires is by cutting a thin slice on the z-x plane from the middle nanowire as illustrated in yellow in Figure 4.7. Then, all the z and x coordinates of the atoms inside this thin slice are plotted in 2D. The thickness of this thin slice is about three layers of atoms.

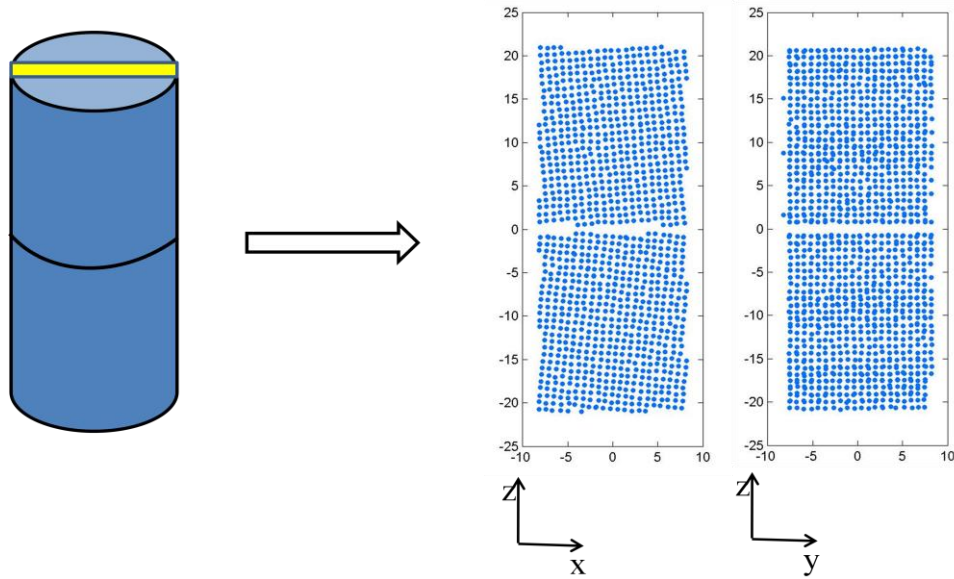


Figure 4.7 The z-x and z-y planes of the nanowire column.

The melting temperature of the 3D LJ crystal is  $T_m = 0.617 \varepsilon/k_B$ . We performed MD simulations at two different temperatures,  $T = 0.4 \varepsilon/k_B$  and  $T = 0.52 \varepsilon/k_B$ , which are 64% and 84% of the melting temperature and are regarded as a low and high temperature in this work, respectively. Every single grain is initially equilibrated under these temperatures to achieve corresponding bulk and surface atom densities. Then, two equilibrated grains are placed close to each other at a distance of  $1.5 \sigma$ . When the experiment starts, the gap between these two grains will be quickly filled and they form a GB. This method is often used in the literature to investigate GB problems[39].

#### ***4.5 The potential energy distribution and potential reduction***

The atoms with different neighbours have different potential energies. As we know from the previous chapter, the potential energy decreases in usually as follows: vapour atoms > surface atoms > GB atoms > bulk atoms. Hence, it is convenient to track down

the potential energy change that is the driving force of the bamboo structure evolution and how much the potential energy has changed. The potential energy of two separate grains could also be monitored and compared with the final structure of bamboo evolution. Moreover, by identifying the surface atoms and GB atoms, their evolution processes could be monitored by plot or dynamic movies. The potential energy distribution of the 3D model of fcc crystal is more complicated than the 2D model (Figure 4.8) because there are more LJ bonds per atom in 3D. The surface and GB cannot be identified separately because they are both regarded as high energy interfaces, which are coloured in green. The bulk atoms are coloured in blue.

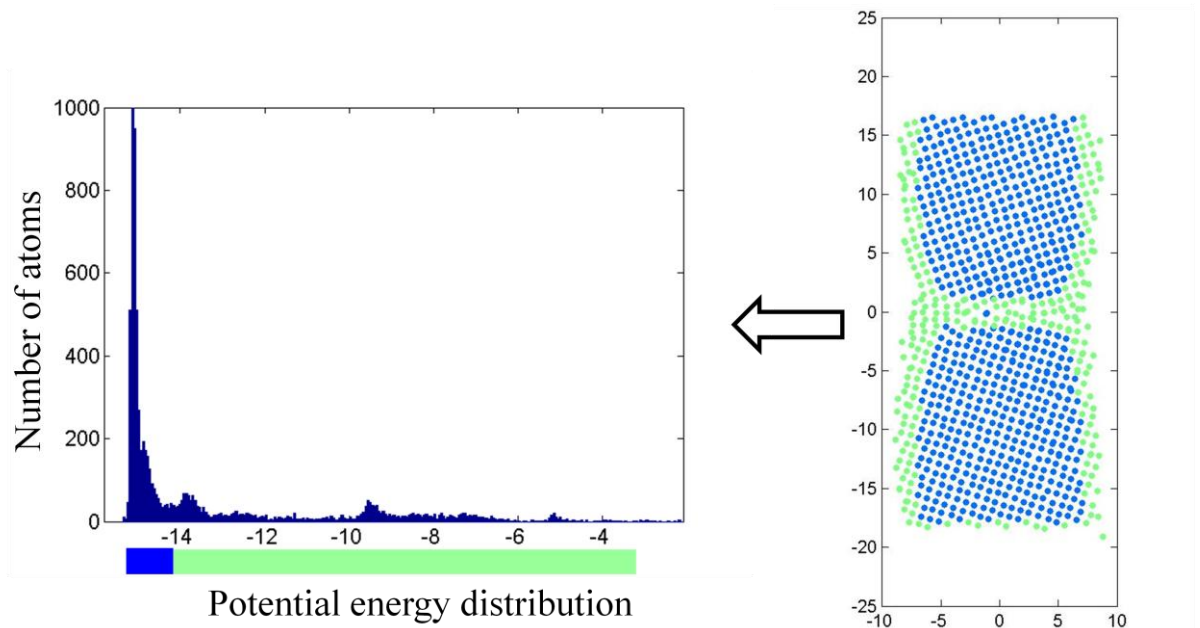


Figure 4.8 The colouring method of surface boundary, GB and bulk atoms based on their potential energies.

## 4.6 Computer simulation results and discussions

### 4.6.1 Elimination of small angle tilt GBs

Before carrying out the multi-scale simulation of bamboo nanowire, the pure MD simulation of two small nano-bamboo grains in contact with each other at a low angle tilt GB was conducted to further examine the crystal reorientation phenomenon in 3D. In our previous 2D nanoparticle interaction study, we found that the nanocrystals with small differences in crystallographic orientation tended to reorient towards each other to eliminate this crystallographic orientation difference.

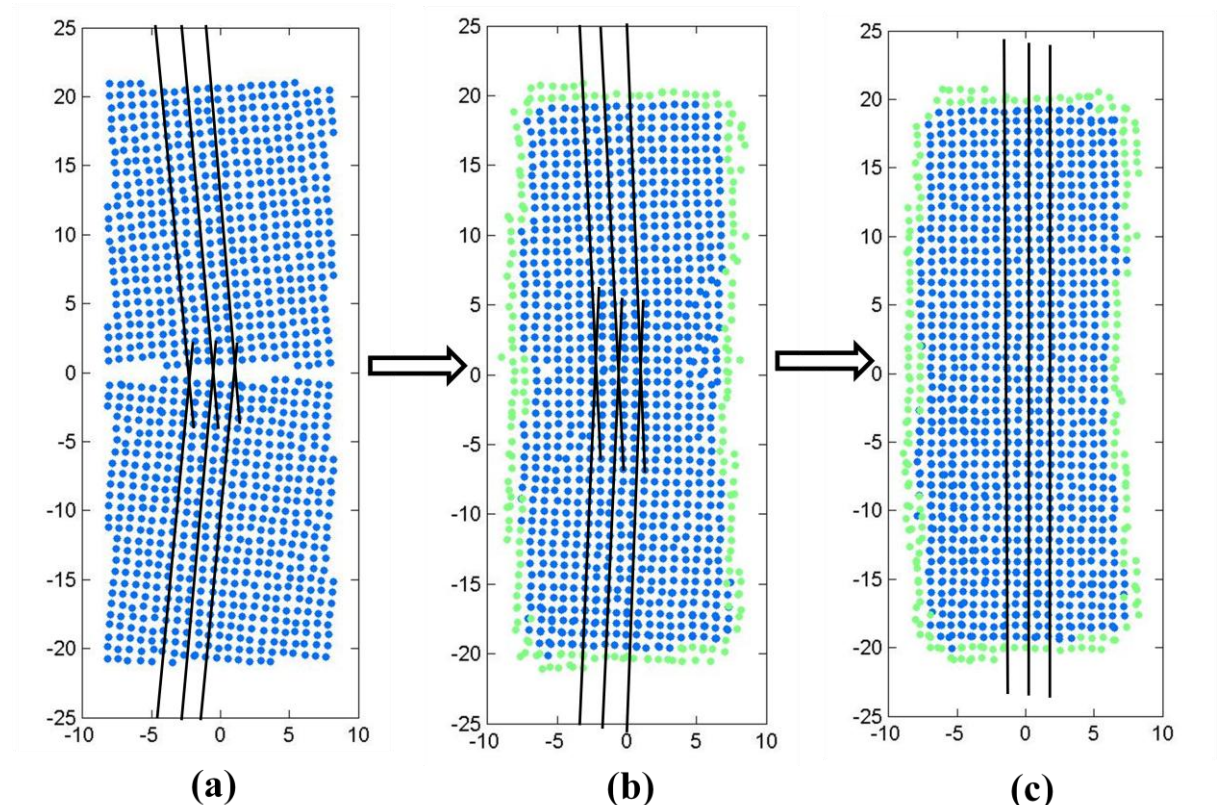


Figure 4.9 Initial reorientation of two free bamboo grains (with no fixed top and bottom continuum regions): (a) represents the nanowire structure at time  $t = 100t^*$ ; (b) represents the nanowire structure at time  $t = 500t^*$ ; (c) represents the nanowire structure at time  $t = 1000t^*$ .

Figure 4.9 shows the microstructure evolution process of the small angle tilt GB formed by two nano-grains under a constant temperature  $T = 0.4 \varepsilon/k_B$ . The degree of small tilt angle is  $8^\circ$ . As expected, the crystal reorientation at the low angle GB also occurs to small nano-grains at 3D. After two nano-grains were placed in contact with each other, no clear GB is observed; instead, several defects including vacancies and dislocations were found in the middle of two grains (Figure 4.9 b). At  $t = 1000t^*$  (Figure 4.9 c) the crystal reorientation quickly eliminated the crystallographic orientation difference and the defects also disappeared from the centre. The two nano-grains then completely aligned with each other and formed a new crystal.

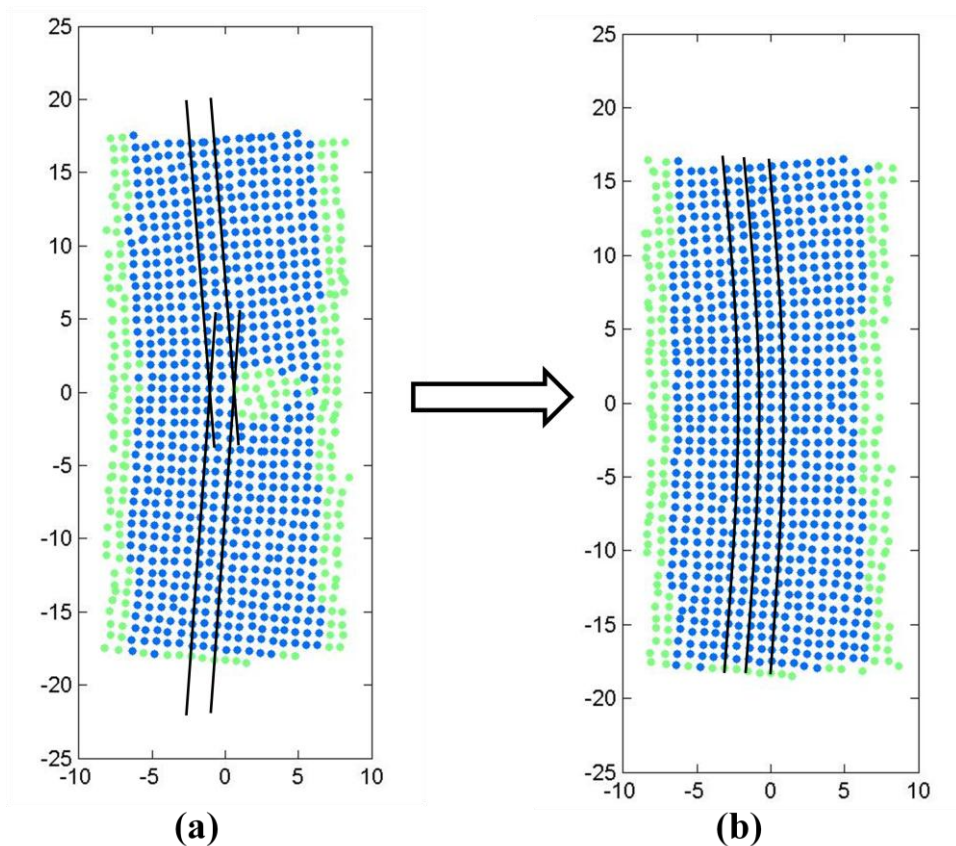


Figure 4.10 The initial low angle GB is eliminated by forming a stable bending structure without any defects for model I at low temperatures: (a) represents the nanowire structure at time  $t = 100t^*$ ; (b) represents the nanowire structure at time  $t = 1000t^*$ .

For the multi-scale model of the bamboo nanowire, the upper and bottom parts of the crystal grains are rigid and recognised as the continuum phase. The rigid continuum phase is not plotted in following pictures. Because of the rigid continuum crystal phase, the crystallographic orientation of the bamboo crystal structure is not easily rotated. Figure 4.10 shows the multi-scale model of the microstructure evolution process of the bamboo nanowire model I with a small angle tilt GB under a constant temperature  $T = 0.4 \varepsilon/k_B$ . The rigid continuum phase is not shown; only the explicit atoms are shown. The blue atoms are presented as bulk atoms. The green atoms are presented as surface atoms, GB atoms, local defects or vacancies. In Figure 4.10 (a), small local disorder with a higher potential energy than bulk atoms coloured green was found in the middle of the bamboo structure at the beginning of the evolution. By time  $t = 1000t^*$ , the small local defects had completely disappeared. The free surface should act as a defect deposition boundary. The entire bamboo structure showed a very stable bending structure without defects. This special bending structure does not exist in ordinary materials. The low angle tilt GB found in ordinary materials looks very similar to a bending structure, but the bend is caused by a series of dislocation walls (Figure 4.11). During our nano-sized MD simulation, the bending structure formed without the presence of dislocations. This is a unique feature at the nano-size level.

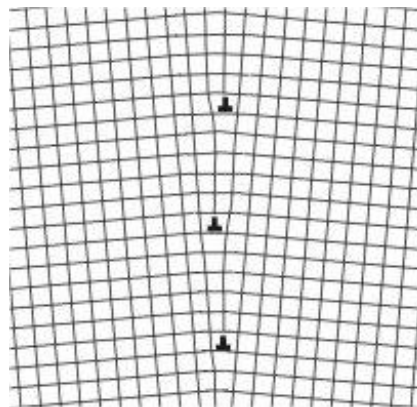


Figure 4.11 The dislocation wall in the conventional low angle tilt GB.

### 4.6.2 Formation of the stable large angle tilt GB

The large angle tilt GB formed in the bamboo structure of model III was found to be stable in our multi-scale model under temperature  $T = 0.4 \varepsilon/k_B$ . Figure 4.12 shows a picture of the stable high angle tilt GB formed in the bamboo structure. A clearly disordered boundary coloured green indicates the GB atoms with the higher potential energy. The dihedral angle in the triple point where the GB meets the surface boundary is around  $160^\circ$  according to the equation:

$$\frac{\gamma_b}{\gamma_s} = \cos \frac{\theta}{2}$$

The dihedral angle  $\theta$  is determined by GB tension  $\gamma_b$  divided by surface tension  $\gamma_s$ . The large dihedral angle formed here in the large tilt GB indicates that the surface tension is larger than the GB tension.

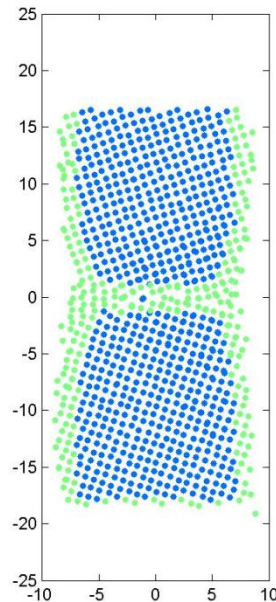


Figure 4.12 The formation of the stable large angle tilt GB for model III at low temperatures.

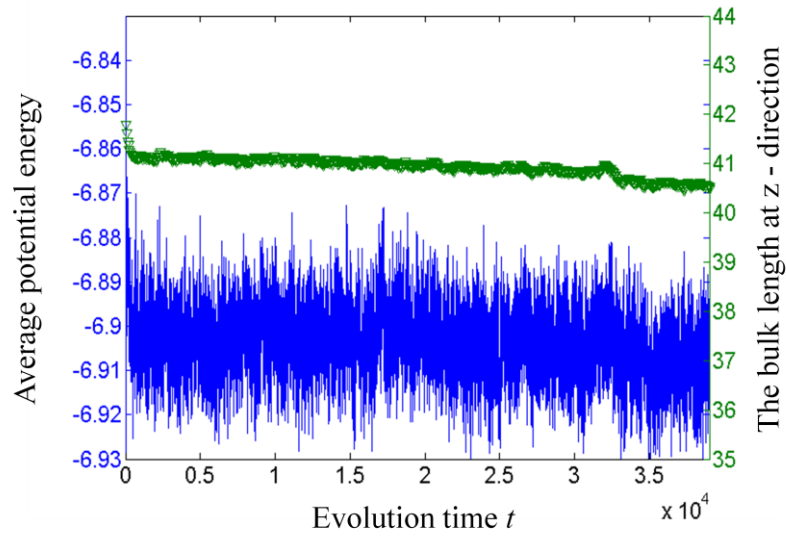


Figure 4.13 The average potential energy and bulk length in the z-direction as a function of evolution time for model III under low temperatures.

Figure 4.13 shows the length change in the z-direction and average potential energy change of the bamboo structure as a function of evolution time. Both the length and average potential energy showed a very small and smooth reduction over the evolution time. GB diffusion is responsible for driving atoms into or out of the GB. The small and smooth length shrinkage in the z-direction implies a slow GB diffusion at a low temperature  $T = 0.4 \varepsilon/k_B$ . The potential energy reduction is the driving force for mass transportation over evolution time.

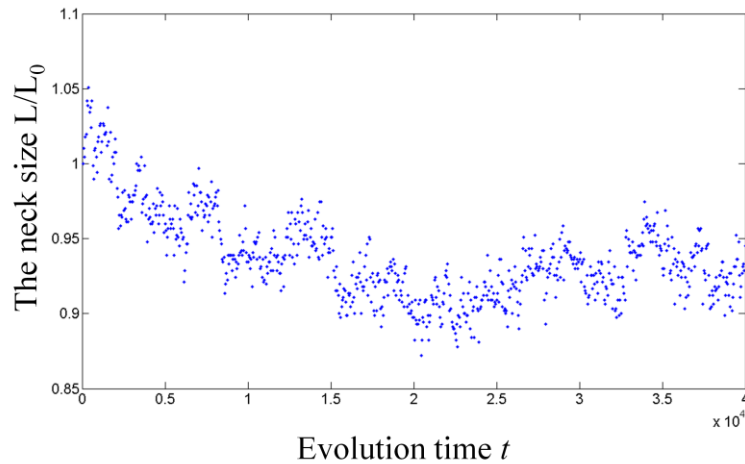


Figure 4.14 The neck size evolution as a function of evolution time for model III under low temperatures.

Figure 4.14 shows the neck size evolution as a function of time. The neck size is initially grooving, but later the grooving stops and necksize increases slightly. The neck size change is a result of both the GB diffusion and surface boundary diffusion processes. The GB diffusion process diffuses matter into or out of the neck region. The surface diffusion process also diffuses matter into or out of the neck region according to the curvature difference. As we found from the bulk length shrinkage of the nanowire, the GB diffusion is also trying to diffuse atoms out of the GB and deposit them into the neck region. The initial grooving is because this fast surface diffusion diffuses atoms out of the neck region, which tries to eliminate the curvature difference around the neck region. After a proper curvature is maintained, the surface diffusion process decreases. Thus, the atoms depositing at the neck region can increase, which brings about the neck size increase.

### 4.6.3 Temperature effect

Models I and III were also carried out the multi-scale MD simulation at an elevated temperature  $T = 0.52 \text{ } \varepsilon/k_B$  to investigate the temperature influence on the bamboo nanowire evolution process. Figure 4.15 shows the evolution process of model I, which starts with low angle GB at an elevated temperature  $T = 0.52 \text{ } \varepsilon/k_B$ . At the beginning of the evolution, a similar evolution at a low temperature  $T = 0.4 \text{ } \varepsilon/k_B$  was used. The low angle GB was also eliminated and a bending structure was formed. Because of the bending, the convex side of the bending should be under a tension stress state and the concave side of the bending should be under a compression state. The energetic convex side and concave side of this bending structure were more apparent at a higher temperature. In Figure 4.15 (a), atoms in the middle part of the two sides appear as a green colour, which indicates more energetic. Owing to the high energy concave and convex points, dislocations were found nucleating from the high energy points. Figure 4.15 shows that more and more dislocation slip planes developed throughout the bamboo nanowire at elevated temperatures. Because of the introduction of these dislocations, the shrinkage and average energy change seemed abrupt (Figure 4.16). The abrupt bulk length reduction is caused by dislocation glide along the  $\langle 111 \rangle$  slip plane. At high temperatures, the high surface tension at the nanowire surface is further strengthened and the crystal plastic resistance is lowered. Therefore, if the surface tension overcame the plastic deformation resistance force, the dislocation nucleation or the dislocation glide could happen. Figure 4.16 shows a slight potential increment peak right before the abrupt potential reduction. This showed the successful overcoming of the potential barrier of the dislocation glide.

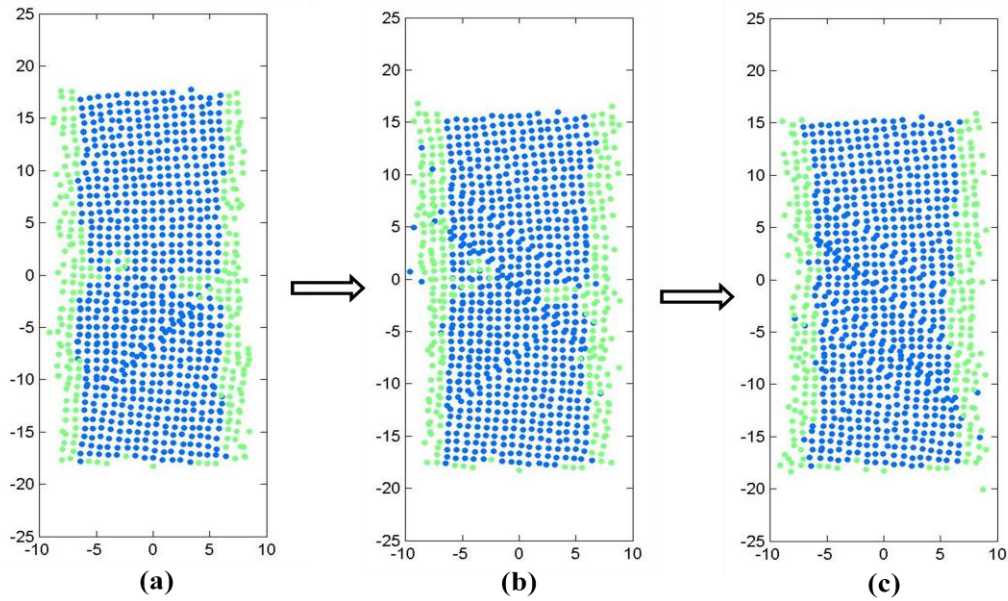


Figure 4.15 Multiple dislocation slip plane was found in model I under high temperatures: (a) represents the nanowire structure at time  $t = 100t^*$ ; (b) represents the nanowire structure at time  $t = 10000t^*$ ; (c) represents the nanowire structure at time  $t = 30000t^*$ .

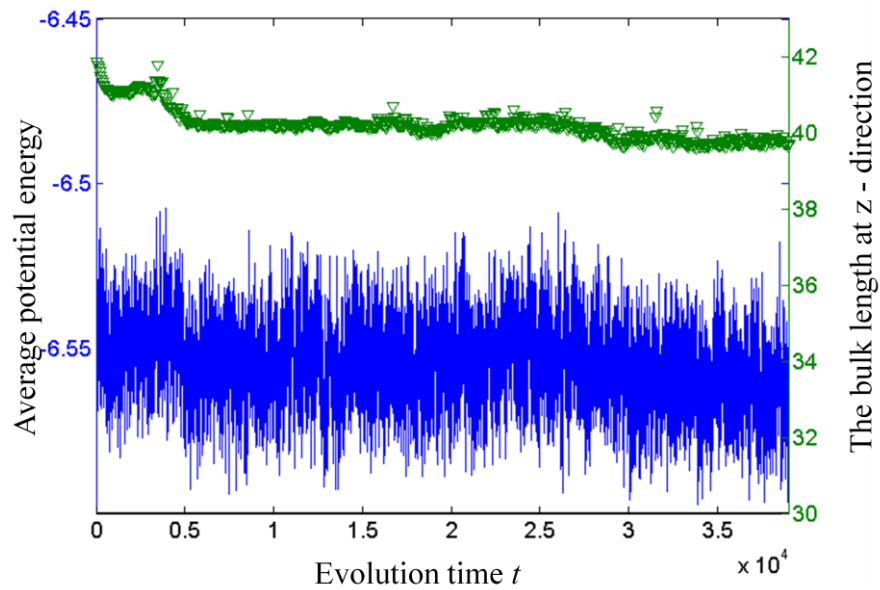


Figure 4.16 Average potential energy and bulk length in the z-direction as a function of evolution time for model I under high temperatures.

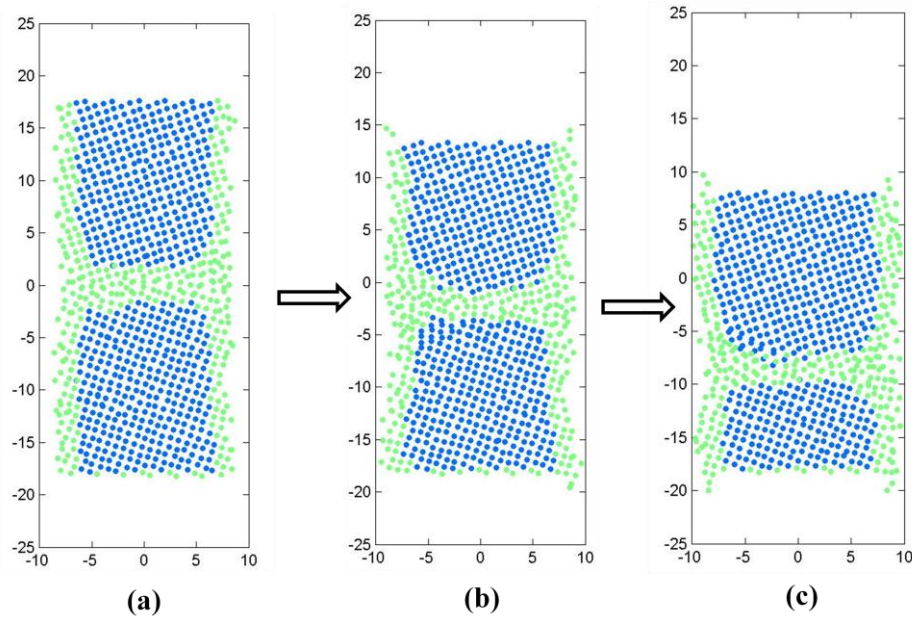


Figure 4.17 The apparent grain growth and GB migration were found using model III under high temperatures: (a) represents the nanowire structure at time  $t = 100t^*$ ; (b) represents the nanowire structure at time  $t = 10000t^*$ ; (c) represents the nanowire structure at time  $t = 30000t^*$ .

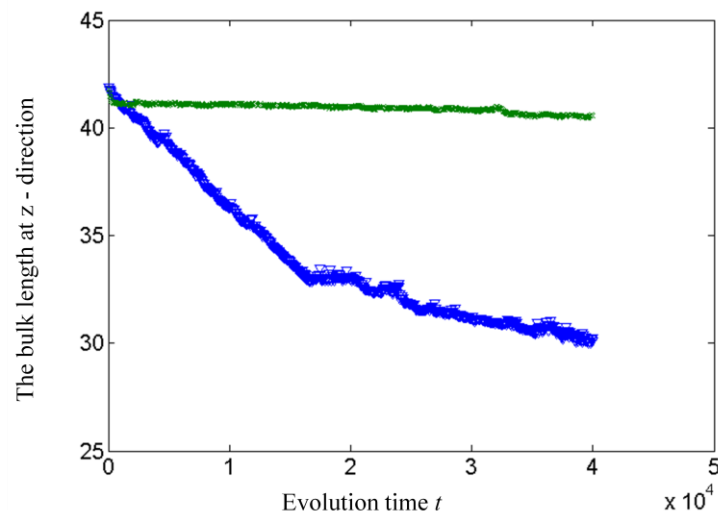


Figure 4.18 The comparison of bulk length shrinkage in the z-direction for model III between low and high temperatures. The green crossed line represents the length shrinkage under low temperatures. The blue triangle line represents the length shrinkage under high temperatures.

Model III, which started with high angle tilt GB, was also carried out on the evolution experiment under an elevated temperature at  $T = 0.52 \varepsilon/k_B$ . Figure 4.17 shows that the bulk length shrinkage in the z-direction is obvious. Meanwhile, an apparent GB migration towards the bottom was observed. Figure 4.18 compares the bulk length shrinkage velocity at high and low temperatures. The bulk length in the z-direction shrinks much faster at high temperatures. This indicates that the GB diffusion is very sensitive to the temperature. High temperatures could easily trigger a fast GB diffusion and bring about shrinkage to the system.

#### 4.6.4 Size effect

To investigate the size effect of the bamboo nanowire, models II and IV, which have smaller radii than models I and III, were carried out in the evolution experiment as well. The evolution experiment of model II, which started with a low angle tilt GB at low temperatures, also showed a bend structure, which is the same behaviour as model I under a low temperature. However, the evolution experiment of model II at high temperatures found more dislocation slip across the structure compared with model I at high temperatures. Figure 4.19 shows three evolution pictures at times  $100t^*$ ,  $10000t^*$  and  $30000t^*$ , which reveals that the slip density is higher than model I at high temperatures. Figure 4.20 also compares the bulk length shrinkage in the z-direction between models II and I. The bulk length shrinkage is triggered by the dislocation glide at the slip plane. The smaller size bamboo nanowire shrunk more as the smaller radius bamboo nanowires provided less plastic resistance to the slip, which is ultimately driven by the surface tension.

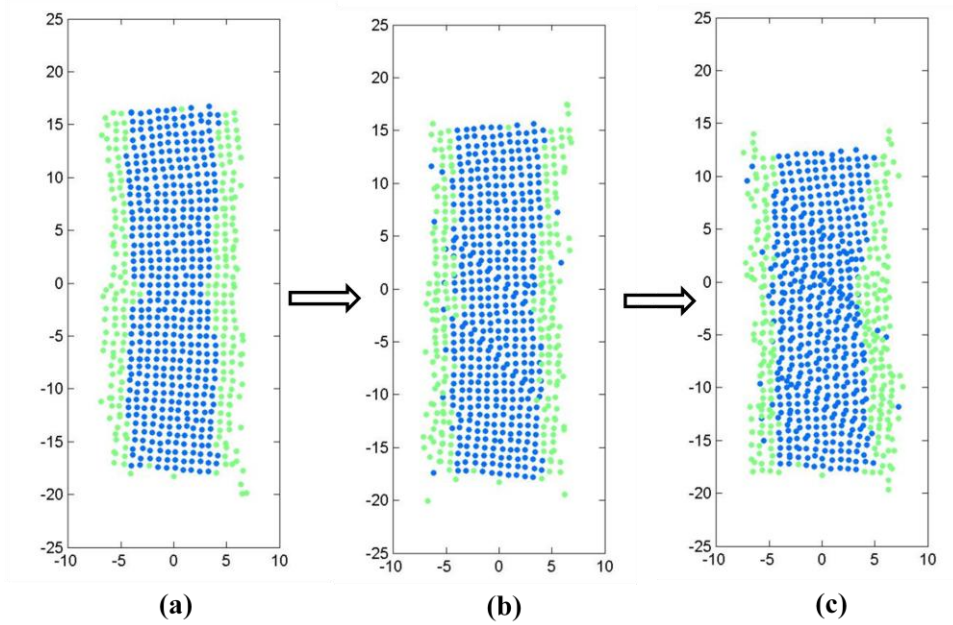


Figure 4.19 Multiple dislocation slip plane was found in model II under high temperatures: (a) represents the nanowire structure at time  $t = 100t^*$ ; (b) represents the nanowire structure at time  $t = 10000t^*$ ; (c) represents the nanowire structure at time  $t = 30000t^*$ .

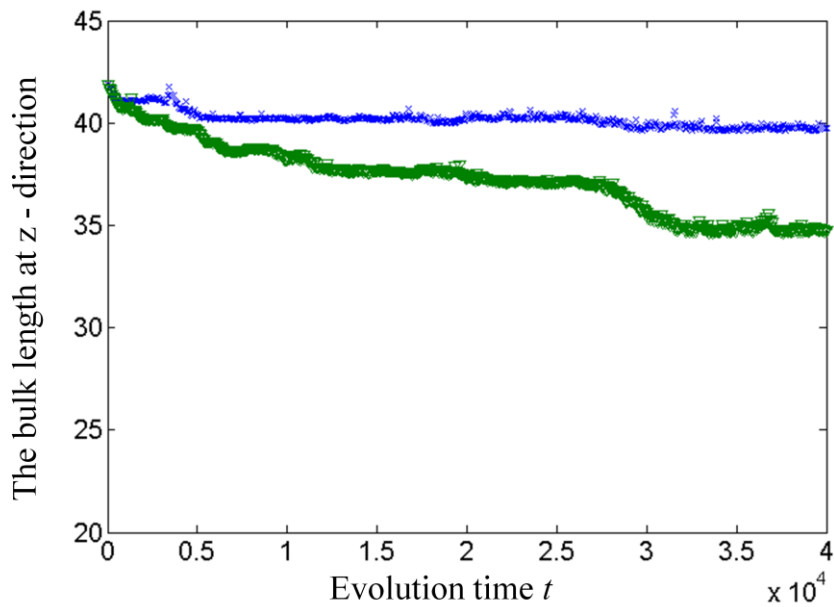


Figure 4.20 The comparison of bulk length shrinkage in the z-direction between models I and II under high temperatures. The blue crossed line represents the length shrinkage of model I. The green triangle line represents the length shrinkage of model II.

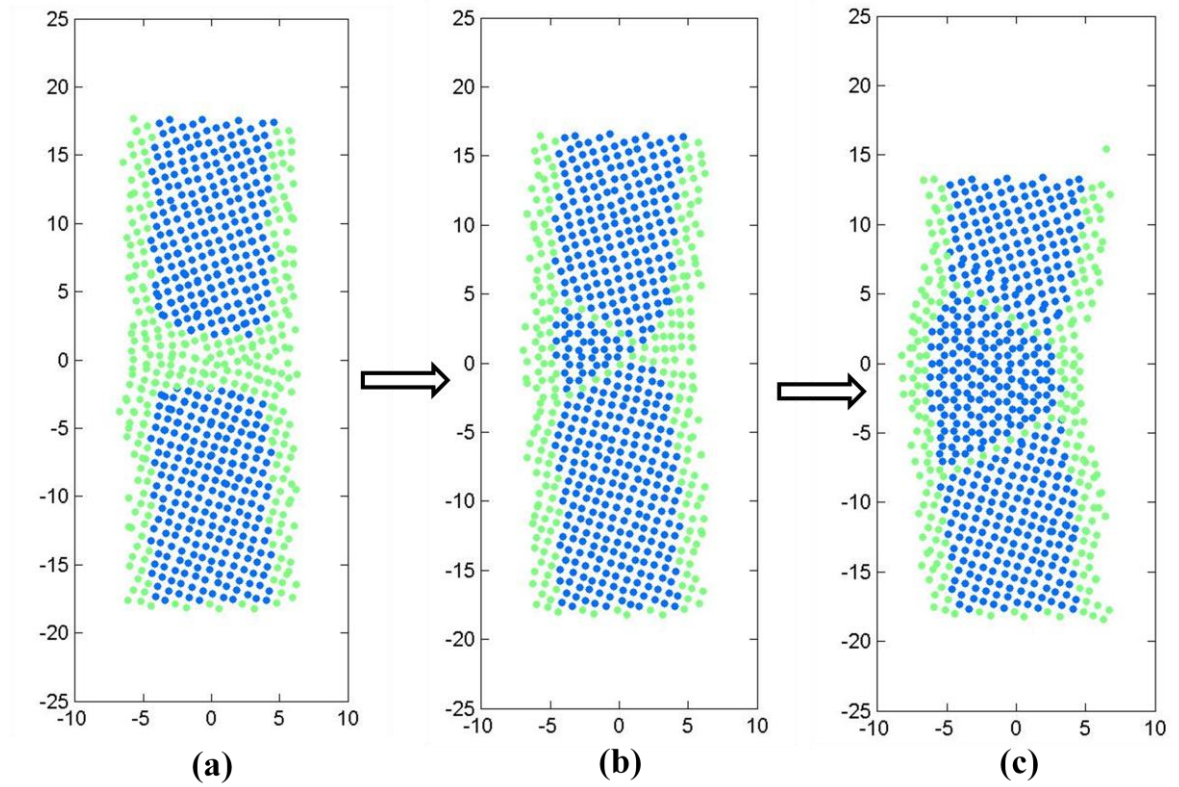


Figure 4.21 One new hcp(hexagonal close-packed) grain was found growing from the triple point in model IV under low temperatures: (a) represents the nanowire structure at time  $t = 100t^*$ ; (b) represents the nanowire structure at time  $t = 10000t^*$ ; (c) represents the nanowire structure at time  $t = 30000t^*$ .

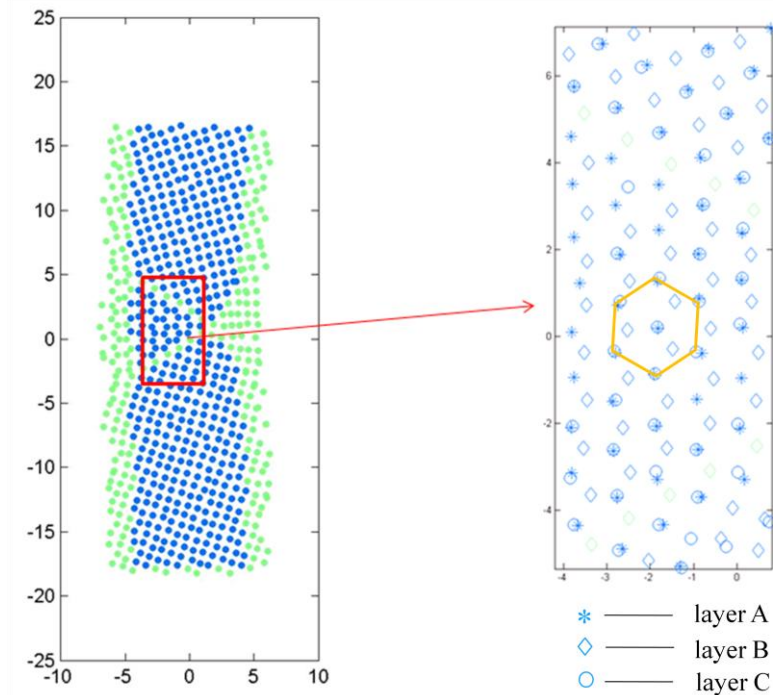


Figure 4.22 Three hexagonal planes (used to be  $\langle 111 \rangle$  at the fcc crystal) sitting on top of each other were plotted with star, diamond and circle shapes (layers A, B and C) from the positions of the newly formed grains. Layer A is obviously overlapped with layer C, which proves that this new grain is an hcp crystal structure.

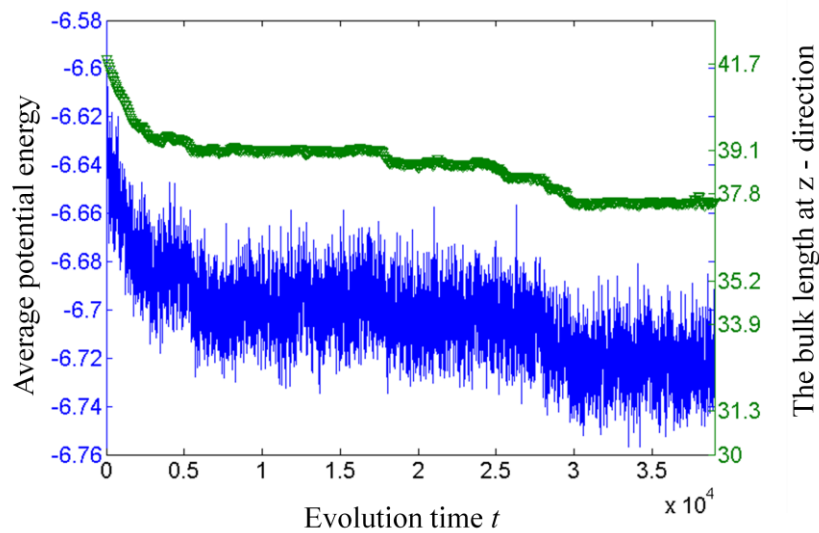


Figure 4.23 The average potential energy and bulk length in the z-direction as a function of evolution time for model IV under low temperatures.

Figure 4.21 shows three evolution pictures of model IV at times  $100t^*$ ,  $10000t^*$  and  $30000t^*$  under a low temperature  $T = 0.4 \epsilon/k_B$ . Model IV has a smaller radius size than model III, which starts with a high angle GB. One interesting phenomenon was found from Figure 4.21. A new grain started nucleation from the triple point where the GB met the surface boundary, and gradually increased its size by invading outwards. This is entirely different behaviour compared with the evolution of model III with a bigger wire radius under the same temperature. The evolution of model III at a low temperature showed a stable high angle GB. The new grain was investigated in Figure 4.22: three hexagonal planes (used to be  $\langle 111 \rangle$  at fcc crystal) sitting on top of each other were plotted with circle, star and diamond shapes. It was found that the first and third layers overlapped with each other; therefore, layer A = layer C. This alternative ABABAB configuration proves that the new crystal is a typical hcp crystal. In a fcc crystal, the position of the first and third layers is different, showing an ABCABC configuration. The original starting bamboo crystal is in a fcc fashion. The nucleation of an hcp grain indicated that an fcc-to-hcp crystal transition was happening during the evolution. This fcc-to-hcp crystal transition is usually found when a fcc crystal is under pressure or loading conditions[40]. The hcp transition found in the smaller nanowires of model IV rather than the bigger nanowires of model III suggests that the large surface tension in the nanowires with smaller radii might play a role in external loading. The reason for this large surface tension is that the melting temperature should be lowered at nano-scale level. And the temperature chose here is about 80% of the normal melting temperature. Put the factor of lowered melting temperature into consideration, it is reasonable to think that the high energy amorphous surface layer is close to the liquid which could generate large surface tension. Figure 4.23 shows the bulk length shrinkage and average potential reduction as a function of evolution time. The bulk length

shrinkage and potential reduction also shows the abrupt change, which is very similar to models I and II with a dislocation slip at high temperatures. Therefore, the hcp and fcc transitions should be dominated by the partial dislocation slip as found in the literature [40].

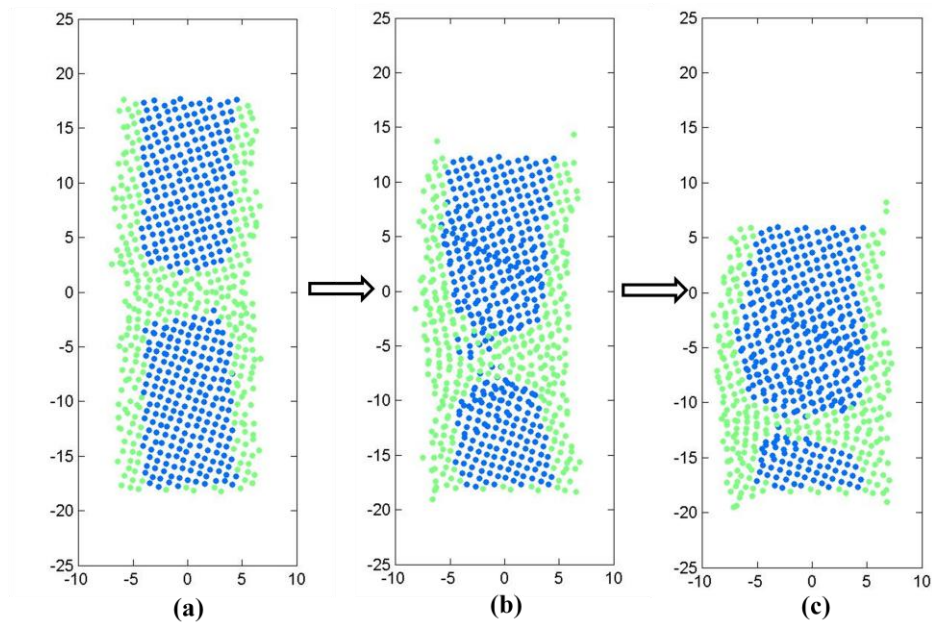


Figure 4.24 Apart from the apparent grain growth and GB migration found in model IV under high temperatures, the dislocation slip is also observed: (a) represents the nanowire structure at time  $t = 100t^*$ ; (b) represents the nanowire structure at time  $t = 10000t^*$ ; (c) represents the nanowire structure at time  $t = 30000t^*$ .

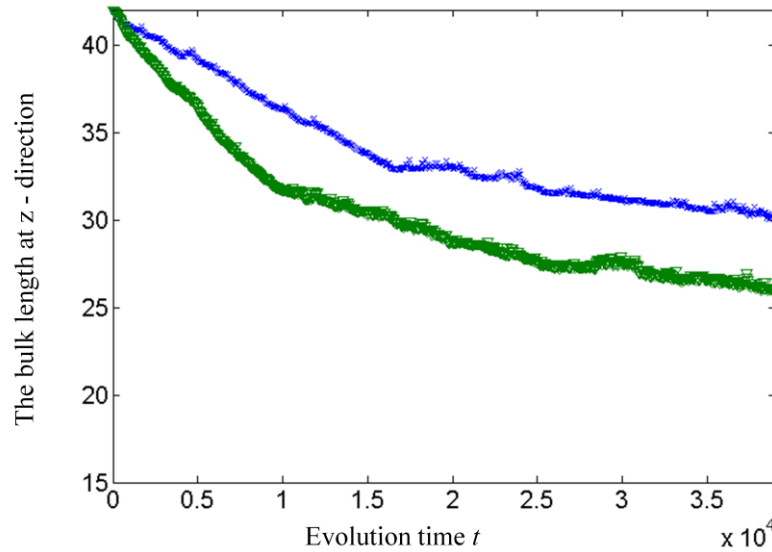


Figure 4.25 The comparison of bulk length shrinkage in the z-direction between models III and IV under high temperatures. The blue crossed line represents the length shrinkage of model III. The green triangle line represents the length shrinkage of model IV.

Figure 4.24 presents the evolution process of model IV at a high temperature  $T = 0.52 \varepsilon/k_B$ . Not only was the high angle GB found during the evolution, dislocation slips were also found inside the bamboo crystal. Figure 4.25 compares the bulk length shrinkage with the evolution of model II at the same high temperature and shows that the bulk length shrinkage of model IV at high temperatures is faster. Because model IV has a small radius, the distance that atoms diffuse from inside the GB to the triple point is shorter and this results in a faster shrinkage process compared with model II.

## 4.7 Conclusions

The evolution of bamboo-like nanowires with different radii is investigated under two different temperatures via multi-scale MD simulation. It is found that the low angle tilt GB inside the nanowire is not stable. The dislocations that form the low angle tilt GB can deposit into the free surface boundary. A bending crystal structure without defects

is formed under low temperatures as a result of the elimination of the low angle tilt GB. However, a high temperature could introduce dislocation slips to the bending crystal. The dislocations introduced are nucleated from the free surface boundary. Therefore, the surface boundary acts as either the dislocation deposition boundary under low temperatures or the dislocation nucleation source under high temperatures. Moreover, the large volume fraction of free surface nanowires also applies surface tension or capillary force to the dislocation slip inside the nanowire, which in turn causes abrupt plastic deformation.

The large angle GB is found stable at low temperatures with relatively large radius nanowires. The large angle GB is very sensitive to temperature. The GB diffusion is much higher at high temperatures, which causes nanowire bulk length shrinkage. An interesting microstructure evolution behaviour of the nanowire with the small radius starting with the large angle GB is observed. A new hcp grain is nucleated from the triple point of the bamboo structure. The growth of this hcp grain actually transforms the original fcc crystal into a hcp crystal. This phenomenon is usually found when the fcc crystal is under external loading or pressure. The large volume fraction of the free surface of the nanowire again applies its large surface tension to the nanowire. The highly disordered triple point where the free surface boundary meets the high angle GB accommodates hcp crystal nucleation. In summary, the microstructure evolution behaviour of the bamboo nanowire is very different to the conventional bamboo structure polycrystals. When the materials reduce to the nano-size, different evolution behaviour occurs.

## **Chapter 5      A MD Study of the Mechanical Behaviour of Semi-crystalline Polymers**

### ***5.1 Introduction to semicrystalline polymers***

Polymers are extensively used materials in various aspects of everyday applications such as in clothing, housing materials, appliances, cars, aerospace devices, medical usage and communication, as well as in many important emerging technologies. Polymers have advantages over other types of materials, such as metals and ceramics, because of their unique properties such as toughness, elongation, impact strength and degradation. Polymers are macromolecules formed by linking many small molecules, or monomers, in a chain via a covalent bond. The simplest hydrocarbon polymer is polyethylene. In this thesis, polyethylene is selected to serve as a typical semicrystalline polymer model because it would be complicated to study all the different kinds of semicrystalline polymers and because polyethylene is the most representative linear semicrystalline polymer that offers valuable data and ideas for the study of other semicrystalline polymers. In polymer science, the term morphology generally refers to polymer chain arrangement and organisation. Polymers can be classified into two different categories according to their different morphologies: amorphous polymers and crystalline polymers. Amorphous polymers consist of totally disordered chains. In the amorphous structure of a glass, as in a liquid, there are no discontinuities or differences in the geometrical arrangement of the molecules from one point to another. Crystalline polymers, by contrast, contain many small polymer crystals that consist by packing the polymer chains into a regular crystal shape. However, within a synthetic polymer there is no 100% crystallised polymer. There must be some amorphous chains acting as

boundaries inside the crystalline polymer. In other words, crystalline synthetic polymers are invariably partly crystalline and partly amorphous; the term crystalline polymers always implies a semicrystalline polymer. Semicrystalline polymer morphology has been an intense area of study for about 50 years since it directly impacts the industrial production of polyethylene and other polyolefin, polyamide and polyester systems, and because it is a fundamental area for academic contribution. The connection between the mechanical properties of semicrystalline polymers and their morphology remains poorly defined, and a wide range of fundamental questions remain unanswered despite the effort invested in this field. The properties of semicrystalline polymers are directly related to their unique structure. Figures 5.1 and 5.2 show a typical melt crystallised spherulitic structure that forms in most semicrystalline polymeric systems. Crystalline polymers have a hierarchical structure, that is there are two different structures on different length scales. The basic unit of most polymer crystals is the chain-folded crystal lamella (Figure 5.2). A typical value for the thickness of crystal lamellar is around 10 nm. Lamellae are separated by amorphous regions; individual chains can be involved in more than one lamella as well as the amorphous regions in between. The chain-folded lamellae are themselves organised in larger scale structures called spherulites (Figure 5.1). These structures, which can be many microns in size, consist of sheaves of individual lamellae that grow out from a central nucleus until finally the whole of the space is filled by these structures.

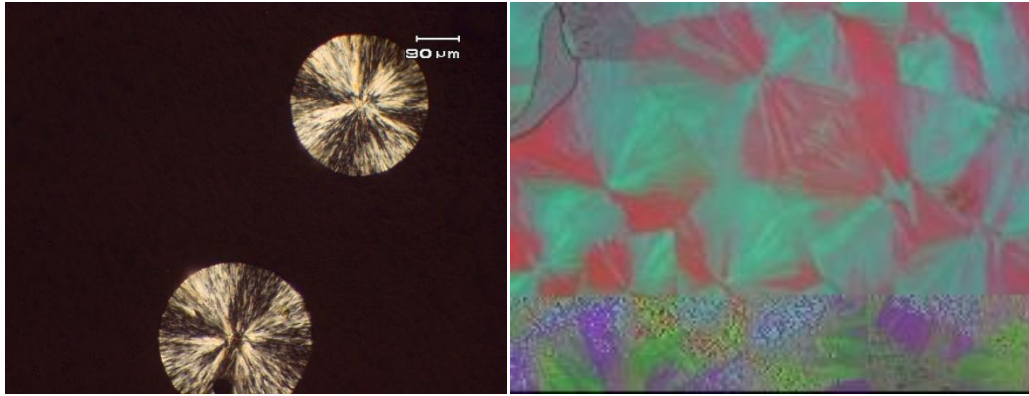


Figure 5.1 Spherulitic structure in a semicrystalline polymer as observed under an optical polarising microscope: single spherulite (left) and spherulitic impingement (right). Taken from [41]

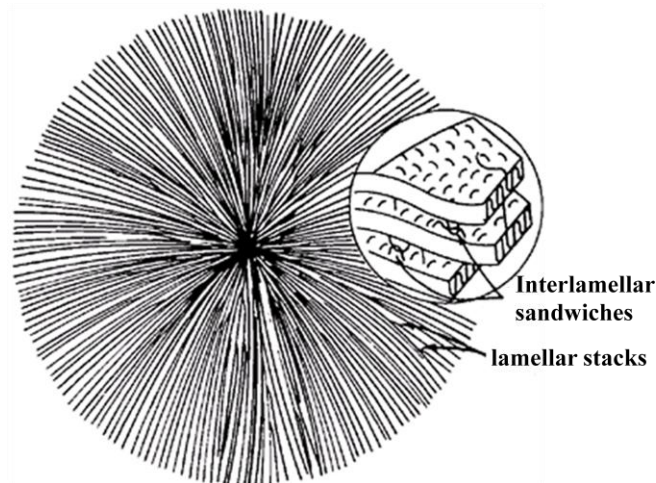


Figure 5.2 Schematic representation of the structure of polymer spherulites. The branches of the spherulites are made of crystal lamellar stacks and all the lamellars are connected via interlamellar amorphous polymers. Taken from [41]

### 5.1.1 The structure of crystal lamellars

The crystal structure of polyethylene was first determined by Bunn [42]. The orthorhombic unit cell, identical to the crystal structure of straight-chain alkanes, is the most stable polymer crystal structure. The basic unit cell of the crystal contains four

CH<sub>2</sub> groups and the all-trans chains are parallel (Figure 5.3). The dimensions of the orthorhombic cell of linear polyethylene are  $a = 0.74$  nm,  $b = 0.49$  nm and  $c = 0.254$  nm according to Busing [43]. There are two different chains in the orthorhombic cell whose zigzag planes have different setting angles of  $\pm 45^\circ$  according to a recent study [44].

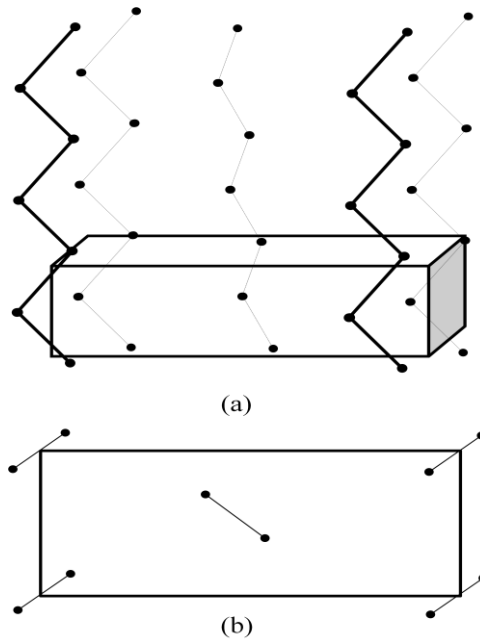


Figure 5.3 Structure of polyethylene crystal, showing the position of the chain in the unit cell. (a) Side view. (b) Projection along the direction of the chain axes [45].

Figure 5.3 represents the skeleton structure of the polyethylene chains. In this diagram, the C-H bonds are omitted for simplicity. The distance of the C-C bonds is 0.1530 nm. The angle between two C-C bonds is  $112^\circ$ . The details of the structure and unit cell dimension vary from one polymer to another, but in all cases the chains run parallel to one another through the unit cell and most linearly zigzag polymer chains are packed in orthorhombic fashion, for instance the PGA crystal that will be discussed in the next chapter.

### 5.1.2 The nature of the interlamellar phase

For most semicrystalline polymers crystallised from the melt, the polymer chains must achieve a regular crystal conformation from the highly entangled melt and align parallel to each other to form thin plate-like crystal lamellars. It is now well established that polymer chains must be folded backwards and forwards across the thickness of the lamellar [46]. Nevertheless, the lamellar is by no means made up of only one polymer chain. The predominant morphology consists of chains threading through alternating layers of the crystalline and amorphous regions. How the crystal lamellar connects with the amorphous phase and the detailed structure of the amorphous phase has been the subject of the extensive research [47],[48].

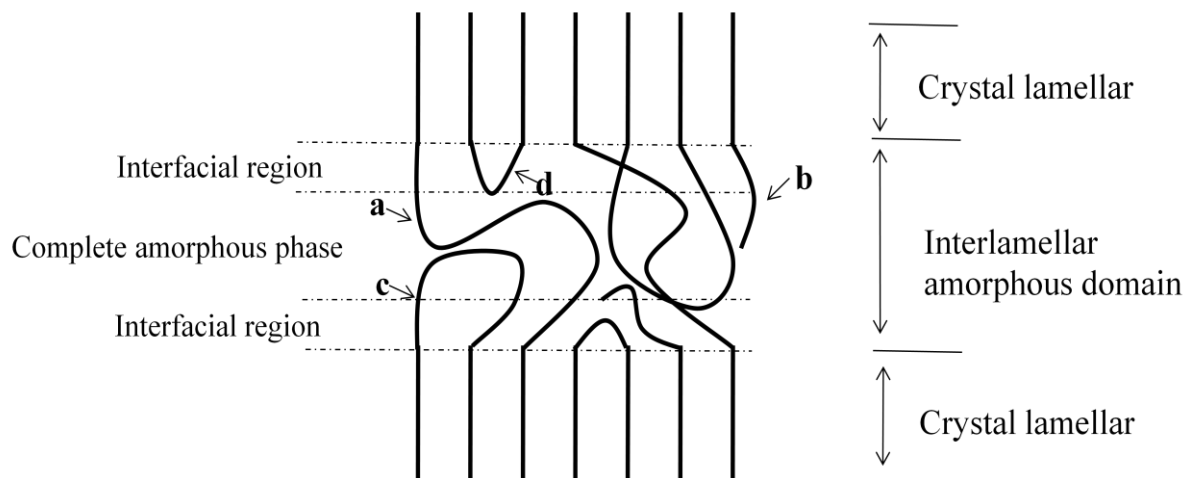


Figure 5.4 An illustration of the crystal lamellar and the interlamellar amorphous region in semicrystalline polymers. The conformations of chains are shown: (a) bridges; (b) chain ends; (c) loose chain folds and (d) tight chain folds.

Various experimental techniques, primarily small-angle X-ray scattering [49], proton NMR [50], Raman spectroscopy [51] and neutron scattering [52], have been employed

to investigate the structure of the interlamellar domain. As a result, it has been concluded that most semicrystalline polymers consist of a crystal lamellar region and an interlamellar amorphous domain. A typical image of the interlamellar region for most semicrystalline polymers is depicted in Figure 5.4. The interlamellar region is about 10–30 nm. Up to now, most research results support the theory that the interlamellar amorphous domain is divided into two zones [53],[54]: the first zone consisting of an interfacial region close to the crystal surface whose conformation still has some dependence on the crystal region and the second zone tending to have a liquid-like nature and be truly amorphous. The size of the interfacial zone is reported to be of the order of 8–10 angstrom [49]. This interfacial zone is also called the “fold surface” because of the existence of the tight chain folds in the surface of the crystal. The population of chains within the interlamellar phase can consist of chain bridges (tie chains), chain ends and chain loops (tight chain folds and loose chain folds; Figure 5.4).

At present, it is widely accepted that the real crystal–amorphous interfaces in semicrystalline polymers exhibit characteristics of both tight chain folding (the so-called “adjacent chain re-entry model”) and loose chain folding (the so-called “switch board model”). The reason for the chain folds back to the crystal is that the density of the crystal lamellar is higher than the amorphous part; in other words, the chain flux from crystal into amorphous must be decreased. These chain folds accommodate this need. The fractions of chains that loop back into the crystal lamella are reported to be in the range from 30% to 70% [55]. The chain ends could be localised near the crystal surface or ends in the total amorphous region.

As the semicrystalline polymer deforms, the crystallites are often seen as hard and inert; the deformation usually comes from the interlamellar amorphous region. There have been some controversial understandings about the mechanical property of the

amorphous interlamellar region. Seguela[56] suggested that the tie chains (the highly stretched chain bridges) are the main factors responsible for the mechanical properties of the semicrystalline polymers. However, Zuo[57] found that the mechanical properties of semicrystalline polymers are mainly dominated by the chain entanglement. In Rutledge's simulation study of the interlamellar phase,[3] the authors suggest that the fraction of the tie chains is extremely low (about 2–8%) and that the tie chains are in a relaxed state.

The deformation of the nano-scale interlamellar molecular structures depends on various interactions between the polymer chains. Unfortunately, the experimental and analytical techniques to understand nano-scale level issues are extremely difficult. It is desirable to create models to simulate the deformation processes and be able to predict the relationship between the material morphology and behaviour at the atomistic level. To understand the relationship between nano-scale structures and mechanical properties, a complex set of interactions governing polymer molecules must be elucidated. The integration of the atomistic, monomeric and configurational attributes of polymer molecules must be included in the development of models. An accurate model can have benefits beyond just predicting the mechanical response of the material. It can provide useful information on the morphological evolution during the manufacturing process and can help identify the required polymer nanostructures to achieve specific properties.

## **5.2 Glass transition temperature and mechanical properties of polymers**

In the study of amorphous interlamellar polymers and their mechanical properties, it is important to understand the concept of the glass transition temperature  $T_g$ . The glass transition temperature is actually a function of chain flexibility. When the polymer is under the glass transition temperature, it is defined as a glassy state and all the polymer chains are very rigid. Only individual polymer chain bead vibration is allowed. The glassy state can be defined as a form of matter that has physical properties similar to a crystalline solid but has the molecular disorder of a liquid. The glass transition occurs when there is enough vibrational (thermal) energy in the system to create sufficient free volume to permit a long chain segment to move together as a unit, but the molecular conformation does not change. At this point, the mechanical behaviour of the polymer changes from rigid and brittle to tough and leathery. Therefore, as the temperature of a polymer drops below  $T_g$ , it behaves in an increasingly hard and brittle manner; as the temperature rises above  $T_g$ , the polymer becomes more rubber-like.

The glass transition temperature is more important than the melting point because it tells us a lot about how the polymer behaves under ambient conditions. The melting temperature is where the polymer changes state from solid to liquid. Technically, only crystalline polymers have a true melting point, the temperature at which the crystallites melt and the total mass of plastic becomes amorphous. Amorphous polymers do not have a true melting point; however, they have a melting temperature region where their mechanical behaviour transitions from a rubbery nature to viscous rubbery flow.

Two important types of polymer behaviour can be assigned to polymers under and above the glass transition temperature according to their response to an application of a

force: elastic and plastic. In the glassy state, the mechanical behaviour of the polymer is relatively stable. The polymer material is very hard and brittle, the modulus remains high and the impact strength is low. When a force is applied, a flow will occur, much like a highly viscous liquid. This is called plastic polymer material. However, as the temperature rises, there will be a point where the behaviour of the polymer will fairly rapidly change from glassy to a very tough and leathery behaviour. When a force is applied the material will deform, but the polymer material will return to its original shape once the force is removed. This is called elastic material. As a matter of fact, plastic and elastic behaviour cannot be purely separate. Most polymer materials demonstrate a combination of these two types of behaviour.

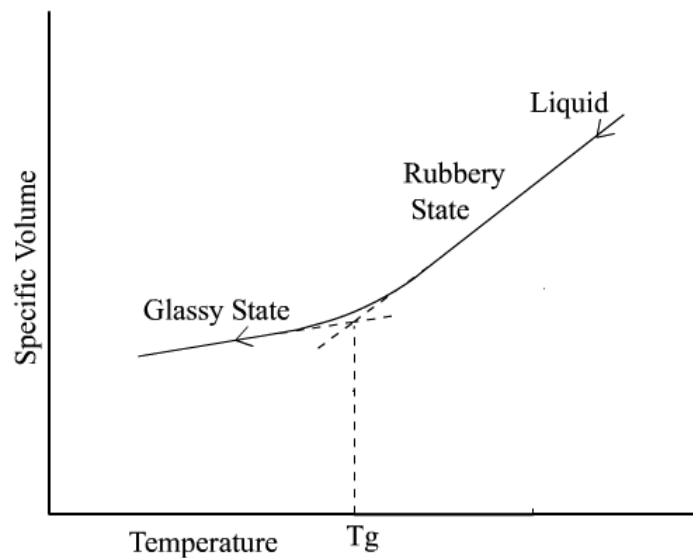


Figure 5.5 The effect of temperature on the total volume of a polymer. Taken from [58]

To quantify the characterisation of the liquid–glass transition phenomenon and  $T_g$ , it is noted that in cooling an amorphous material from the liquid state, there is a change in

slope of the curve of specific volume vs. temperature at the glass transition temperature, moving from a low value in the glassy state to a higher value in the rubbery state over a range of temperatures.

### **5.3 The thermodynamics of the deformation of amorphous polymers**

This section presents a brief outline of the thermodynamics of the amorphous polymer's deformation. Most of the materials in this section is taken from the book by Ward[59]. Consider a force applied to a piece of amorphous polymer material,  $f$ , is related to its stretched length,  $l$ . For an isothermal change of state at a constant volume, the work done can be equated to the change in the Helmholtz function  $A$ . The work done on the solid in an infinitesimal displacement  $dl$  is:

$$dW = fdl = dA = dU - TdS - SdT \quad (5.3.1)$$

where  $U$  represents internal energy,  $S$  is entropy and  $T$  is temperature.

Under isothermal conditions:

$$f = \left(\frac{\partial A}{\partial l}\right)_T = \left(\frac{\partial U}{\partial l}\right)_T - T\left(\frac{\partial S}{\partial l}\right)_T \quad (5.3.2)$$

For the ideal elastomer, the entropy model assumes that the internal energy change during deformation can be ignored [59]:

$$\left(\frac{\partial U}{\partial l}\right)_T = 0 \quad (5.3.3)$$

It is the entropy increase of the polymer chains from a disordered state to a more ordered state during deformation that provides the elasticity of the material. The entropy theory reflects the fact that very little force is carried by the polymer backbone during deformation. During the polymerisation process, the repeating units connect to each other to form long polymer chains following the random walk mechanism. These polymer chains have their end-to-end distances distributed in the form of a Gaussian error function. The entropy of a single chain can be calculated as [59] (Figure 5.6):

$$s = c - k_B^2 r^2 = c - k_B^2 (x^2 + y^2 + z^2) \quad (5.3.4)$$

where  $b$  is Gaussian parameter,  $c$  is an arbitrary constant,  $k$  is the Boltzmann constant,  $r$  is the end-to-end vector and  $x$ ,  $y$  and  $z$  are vector  $r$ 's coordinates.

The root mean square chain end-to-end length can be calculated as [59]:

$$\langle r^2 \rangle = ma^2 = \frac{3}{2b^2} \quad (5.3.5)$$

where  $a$  is the bond length,  $m$  is the number of the bonds and  $b$  again is the Gaussian parameter.

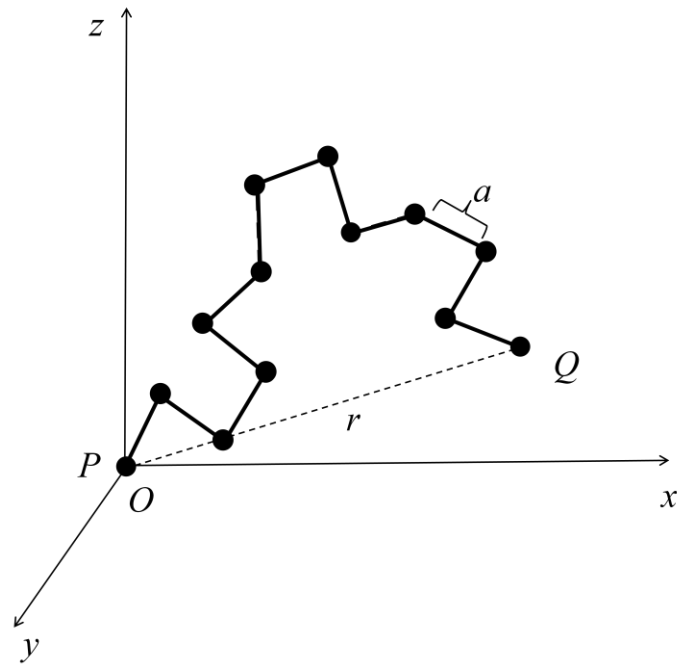


Figure 5.6 A single polymer chain

The entropy changes if the polymer chain deforms, i.e. the chain end moves from Q to Q', as in Figure 5.7.

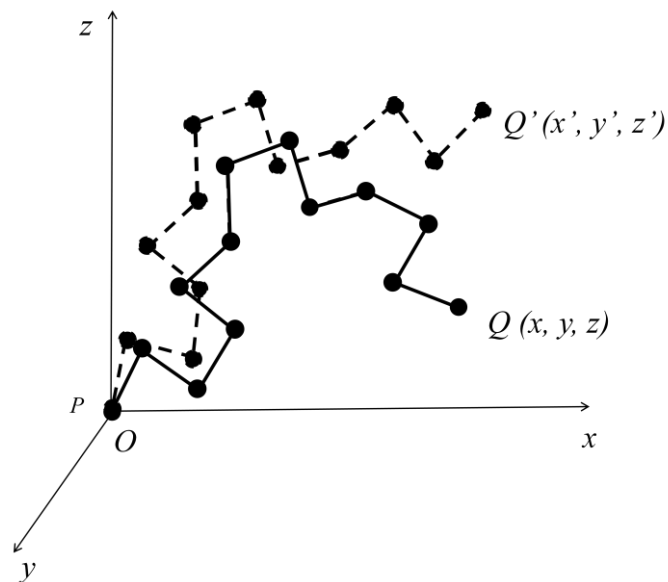


Figure 5.7 Entropy change of a single chain as the polymer deforms.

If the deformation of this chain follows:

$$x' = \lambda_1 x; \quad y' = \lambda_2 y; \quad z' = \lambda_3 z \quad (5.3.6)$$

the entropy of the chain after the deformation becomes:

$$s' = c - kb^2(\lambda_1^2 x^2 + \lambda_2^2 y^2 + \lambda_3^2 z^2) \quad (5.3.7)$$

The difference of the entropy in this case is:

$$\Delta s = -kb^2[(\lambda_1^2 - 1)x^2 + (\lambda_2^2 - 1)y^2 + (\lambda_3^2 - 1)z^2] \quad (5.3.8)$$

For  $N$  chains per unit volume in the system, because there is no preferred direction for the chain vectors in the isotropic state, there is no preference for the x-, y- and z- directions with the mean square chain length, so that:

$$\sum_1^N x^2 = \sum_1^N y^2 = \sum_1^N z^2 = \frac{1}{3} \sum_1^N r^2 = \frac{1}{3} N \langle r^2 \rangle = \frac{1}{3} N \left[ \frac{3}{2b^2} \right] \quad (5.3.9)$$

The total entropy change for all the  $N$  chains in a unit volume can be derived as:

$$\Delta S = \sum_1^N \Delta s = -\frac{1}{2} Nk[(\lambda_1^2 + \lambda_2^2 + \lambda_3^2) - 3] \quad (5.3.10)$$

The Helmholtz function is defined by:

$$\Delta A = \Delta U - T\Delta S \quad (5.3.11)$$

Because it is assumed that there is no change in the internal energy  $\Delta U = 0$

$$\Delta A = -T\Delta S = \frac{1}{2} NkT[(\lambda_1^2 + \lambda_2^2 + \lambda_3^2) - 3] \quad (5.3.11)$$

The change in strain energy comes from the change in Helmholtz free energy and if the strain-energy function  $U_s$  is zero initially, and then we have:

$$U_s = \Delta A = \frac{1}{2} NkT[(\lambda_1^2 + \lambda_2^2 + \lambda_3^2) - 3] \quad (5.3.12)$$

Consider the simple elongation  $\lambda$  in the x-direction; the incompressibility relationship indicates  $\lambda_1\lambda_2\lambda_3 = 1$ , by symmetry we have  $\lambda_2 = \lambda_3 = \lambda^{-1/2}$

Equation (5.3.12) becomes:

$$U_s = \Delta A = \frac{1}{2} NkT[\lambda^2 + \frac{2}{\lambda} - 3] \quad (5.3.13)$$

Then we have:

$$f = \frac{\partial U}{\partial \lambda} = NkT(\lambda - \frac{1}{\lambda^2}) \quad (5.3.14)$$

For a small strain, let  $\lambda = 1 + e_{xx}$ , then the stress is:

$$\begin{aligned} \sigma_{xx} = f\lambda &= NkT(\lambda^2 - \frac{1}{\lambda}) = NkT((1 + e_{xx})^2 - \frac{1}{1 + e_{xx}}) \\ &= NkT(1 + 2e_{xx} + e_{xx}^2 - \frac{1}{1 + e_{xx}}) \end{aligned} \quad (5.3.15)$$

We approximate  $e_{xx}^2 = 0$ , we have  $1 = 1 - e_{xx}^2 = (1 - e_{xx})(1 + e_{xx})$ , so  $\frac{1}{(1 + e_{xx})} = (1 - e_{xx})$

$$\text{Then } \sigma_{xx} = NkT(1 + 2e_{xx} - (1 - e_{xx})) = 3NkTe_{xx} \quad (5.3.16)$$

We then have Young's modulus E:

$$E = \frac{\sigma_{xx}}{e_{xx}} = 3NkT \quad (5.3.17)$$

That is, Young's modulus under isothermal conditions is proportional to the number of polymer chains of a unit volume of polymers times the absolute temperature. The condition for this equation is that the polymer should be under the ideal elastomer state. The entropy theory is true for polymers in the elastomer state because when a polymer is in the elastomer state, the temperature should be around the glass transition temperature. Because all the polymer chains have relatively large free volume-to-vibrate, the forces generated by internal energy, which includes both inter-chain potential energy (bond potential, bond angle potential and torsional energy) and intra-chain potential energy (LJ potential), are weak. By contrast, for polymers under the glass transition temperature, the glassy state and the mechanical strength are mainly dominated by the inter-atomic forces and the entropy term can be neglected:

$$T\left(\frac{\partial S}{\partial l}\right)_T = 0$$

Therefore:

$$f = \left(\frac{\partial U}{\partial l}\right)_T \quad (5.3.18)$$

## **5.4 Molecular dynamics simulation of the semicrystalline polymers**

The application of atomistic simulation develops rapidly in polymer science because of the complexity of macromolecular architecture and geometrical structure, the enormous variability of physical properties and the widespread range of application in the nano- and micro-scale regions. For real laboratory techniques, it is possible to examine some of the polymer properties at the nano-scale level, such as the chemical composition of polymers, the degree of polymerisation or crystallisation using nuclear magnetic resonance or other spectrum techniques. However, it is very difficult or even impossible to observe polymer chain activities fully or handle any mechanical test at the atomistic level.

Theoretical continuum methods usually apply rough mathematical approximations that are not always easy to validate, together with the limitation that its usefulness is only at the nano-length level. By contrast, atomistic simulation, such as the MD and Monte Carlo(MC) methods, can study nano-scale level polymer systems in full detail. With such atomistic simulations, it is straightforward to explore the polymer system at the nano-scale, particularly the polymer interphase among crystal and amorphous polymers.

### **5.4.1 The force field**

A proper choice of potentials governing the interactions is crucial in predicting macroscopic properties of the polymeric systems. The force field for the united atom model of polyethylene have been originally proposed by Paul et al.[60] and modified subsequently by Bolton et al.[61] and by In't Veld and Rutledge.[62]. This force field

finally modified by Rutledge has previously shown to describe accurately both the structure and dynamics of the amorphous polyethylene melt, crystallization and melting transitions for n-alkanes and polyethylene, and structure and kinetics of lamellar crystallization of polyethylene from the melt[63, 64].

The LJ potential is used to compute the non-bonded CH<sub>2</sub> interactions between all united atomic bead pairs on different chains and those separated by three or more beads within the same chain. The LJ potential equation is:

$$E_{LJ,ij} = 4\varepsilon_{LJ} \left[ \left( \frac{\sigma_{LJ}}{d_{ij}} \right)^{12} - \left( \frac{\sigma_{LJ}}{d_{ij}} \right)^6 \right], \quad d_{ij} = |\Delta r_{ij}|, \quad \Delta r_{ij} = r_i - r_j \quad (5.4.3)$$

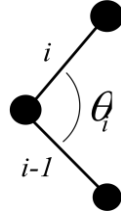
where  $\varepsilon_{LJ} = 390.95$  J/mol,  $\sigma_{LJ} = 0.4009$  nm and  $r_i$  and  $r_j$  represent the Cartesian coordinates of sites  $i$  and  $j$ , respectively. Non-bonded LJ interactions are truncated at a cut-off distance  $r_c = 2.5 \sigma_{LJ}$  to avoid extensive computation, which is the same as in the previous chapter. The covalent bond stretching potential is harmonic in bond length:

$$E_{i,j} = \frac{1}{2} k_l (l_{ij} - l_0)^2 \quad (5.4.4)$$

where  $l_{ij}$  is the length of the covalent bond between beads  $i$  and  $j$  and the bond stretching constants are  $k_l = 376.1 \cdot 10^6$  J/mol/nm<sup>2</sup> and  $l_0 = 0.153$  nm.

The covalent bond angle bending potential is also harmonic in the cosine of the bond angle:

$$E_{\theta,i} = \frac{1}{2} \frac{k_\theta}{\sin^2 \theta_0} (\cos \theta_i - \cos \theta_0)^2 \quad (5.4.5)$$



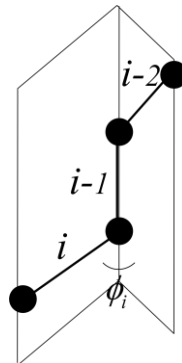
where  $\theta_i$  is the bond angle constructed by two connected covalent bonds  $i$  and  $i-1$  and the angle bending constants are  $k_\theta = 502.1$  kJ/mol and  $\theta_0 = 112.0^\circ$ .

The covalent bond torsion potential has the form:

$$E_{\phi,i} = \sum_{n=0}^3 k_n \cos^n \phi_i \quad (5.4.6)$$

where  $\phi_i$  is the covalent bond torsion angle constructed by bond pairs  $\{i, i-1\}$  and  $\{i-1, i-2\}$  and the torsion constants are  $k_n \in \{6.498, -16.99, 3.626, 27.11\}$  kJ/mol. Here  $\cos \phi_i$  is calculated using:

$$\Delta r_i = r_i - r_{i-1}, \quad n_i = \Delta r_i \times \Delta r_{i-1}, \quad \cos \phi_i = \frac{n_i \bullet n_{i-1}}{|n_i| |n_{i-1}|} \quad (5.4.7)$$



where  $r_i$  represents the position vector of united atomic bead  $i$  and  $\Delta r_i$  is the bond vector between the two bonded sites. The total torsion potential is obtained by summing all available torsion angles.

### **5.4.2 Coupling between the rigid crystal lamellar and flexible atomistic interlamellar phase at a constant temperature**

The focus of this model is to capture the nature of the amorphous interlamellar phase at the atomistic level. The crystal lamellars are aimed to be treated as inert and rigid. But they should still retain their exact atomic crystal structures to exert the realistic atomic interactions to the atoms in the interlamellar phase. The proposed MD configuration of the interlamellar phase is shown in Figure 5.8. The amorphous interlamellar region is jointed with two neighbouring crystal lamellars. All the polymer beads are explicitly modelled in the simulation. However, only the beads inside the interlamellar region are allowed to move according to their interaction forces. All the polymer beads in the crystal region are kept rigid. The crystal regions are only allowed to move as a whole block in the z axis to trigger the deformation of the amorphous interlamellar phase. As a result, the problem of coupling between the rigid crystal lamellar and flexible atomistic interlamellar phase seems to be similar to the multi-scale modelling of coupling the atomistic and continuum regions. Only the continuum region is replaced by the rigid molecules here. There are many methods to couple the atomistic/continuum region in the literature. Among them, Miller's stadium damping theory has proven very effective and accurate and is employed in this study to solve the coupling between the rigid crystal lamellar and flexible atomistic interlamellar phase under a constant temperature [33].

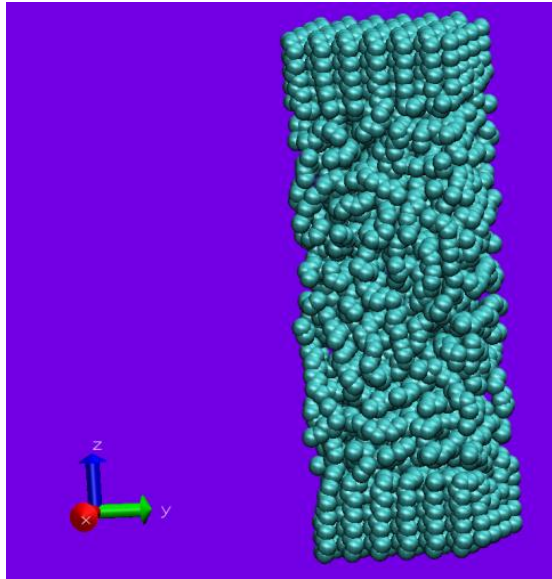


Figure 5.8 The MD configuration of interlamellar phase.

### 5.4.3 Neighbour list

Two types of neighbour lists are used in the polymer MD simulation. The first type of neighbour list is for storing LJ potential pairs as Chapter 2. The second type of neighbour list is for the potentials calculation within the polymer chain: the covalent bond potential, covalent bond angle potential and covalent bond torsion potential.

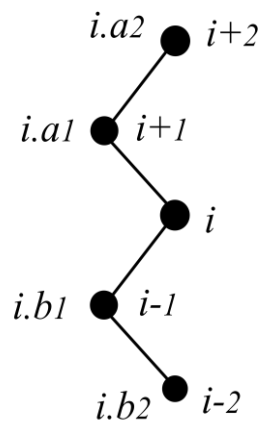


Figure 5.9 The neighbour list method used in a polymer chain.

For each polymer bead  $i$ , four variables are constructed to store its four closest neighbours:  $i.a1 = i+1$ ;  $i.a2 = i+2$ ;  $i.b1 = i-1$ ; and  $i.b2 = i-2$ . If bead  $i$  is near or at the end of a polymer chain, four of these beads,  $i+1$ ,  $i+2$ ,  $i-1$  and  $i-2$  might not exist. For any neighbour that does not exist, minus one ( $-1$ ) is assigned to the neighbour variable; for instance, if bead  $i$  is the chain end, bead  $i-1$  and  $i-2$  do not exist, then  $i.b1 = -1$  and  $i.b2 = -1$ . By this way, it is very convenient to identify the polymer chain ends. Once we can identify the chain ends, it helps recognise each polymer chain, which is essential for analysing and reconstructing all polymer chains. Of course, if a chain break or chain swap happens, the neighbour list also needs to be updated.

#### **5.4.4 Boundary conditions**

IBCs are used in the  $z$  direction of a polymeric system. Both top- and bottom-restricted polymer crystal lamellars act as crystal boundaries for interlamellar amorphous polymers. Beyond them are vacuums. In the  $x$ - and  $y$ -directions of a polymeric system, PBCs are applied. The explicit motion of all polymer beads is tracked in the predefined cell. This cell is surrounded by infinitely replicated, periodic images of itself along the  $x$  and  $y$  directions. Therefore, a polymer bead can interact not only with particles in the same cell but also with beads in adjacent image cells.

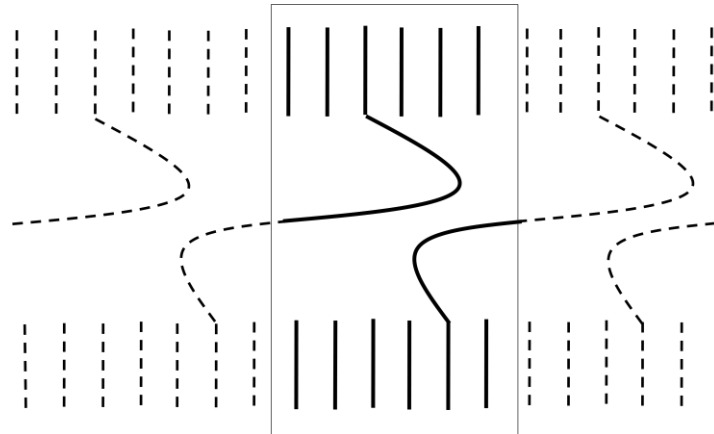


Figure 5.10 A schematic illustration of PBCs, which explains that the polymer chain can leave the left boundary and re-enter from the right boundary (solid lines are the polymer chains in the predefined MD cell and dashed lines are the polymer chains in its adjacent image cells).

The technical detail of the PBCs is elaborated as follows:

- a) During the MD simulation, after each integration step of bead motion the bead's coordinates must be examined. If an atom is found to have moved outside the region its coordinates must be adjusted to re-enter from the opposite side. For instance, the x coordinate is defined to lie between  $-L_x/2$  and  $L_x/2$ , where  $L_x$  is the region size in the x-direction:

If  $r_{ix} \geq L_x/2$ , then  $r_{ix} = r_{ix} - L_x$ ; and

If  $r_{ix} \leq -L_x/2$ , then  $r_{ix} = r_{ix} + L_x$ .

- b) If we need to calculate the interaction of beads between the original cell and its adjacent image cell, we need to first update the beads' coordinates to its mirror image.

For LJ potential, covalent bond potential and angle potential, updating the pair's bond vector is the same as updating the bead coordinate of its mirror image:

If  $r_{ijx} \geq L_x/2$ , then  $r_{ijx} = r_{ijx} - L_x$ ; and

If  $r_{ijx} \leq -L_x/2$ , then  $r_{ijx} = r_{ijx} + L_x$ .

Because the force calculation equation can be simplified to contain only bond vectors let's take the covalent bond force calculation, for example:

$$E_{i,j} = \frac{1}{2} k_l (l_{ij} - l_0)^2$$

$$F_{r_i} = -\nabla_{r_i} E_{i,j} = -(E_{i,j})' \nabla l_{ij} = -(E_{i,j})' \nabla \sqrt{l_{ijx}^2 + l_{ijy}^2 + l_{ijz}^2}$$

$$F_{r_{ix}} = -(E_{i,j})' \frac{d\sqrt{l_{ijx}^2 + l_{ijy}^2 + l_{ijz}^2}}{dr_{ix}} = -(E_{i,j})' \frac{d\sqrt{l_{ijx}^2 + l_{ijy}^2 + l_{ijz}^2}}{dl_{ijx}} \frac{dl_{ijx}}{dr_{ix}} = -(E_{i,j})' \frac{d\sqrt{l_{ijx}^2 + l_{ijy}^2 + l_{ijz}^2}}{dl_{ijx}}$$

, where  $l_{ijx} = r_{ix} - r_{jx}$ ;

$$F_{r_{iy}} = -(E_{i,j})' \frac{d\sqrt{l_{ijx}^2 + l_{ijy}^2 + l_{ijz}^2}}{dl_{ijy}}$$

$$F_{r_{iz}} = -(E_{i,j})' \frac{d\sqrt{l_{ijx}^2 + l_{ijy}^2 + l_{ijz}^2}}{dl_{ijz}}$$

For the LJ potential and angle potential, the force calculation equation could also be simplified to contain the bond vector only and eliminate the exact bead coordinates; therefore, it only needs to update the bond vector for the effect of periodicity.

However, for the covalent bond torsion potential, it is necessary to update the beads' coordinates of one side of its mirror image to match the beads on the other side of the boundary because the force calculation equation involves all the beads' coordinates and cannot be simplified to contain only the bond vector.

#### **5.4.5 Generation of the initial semicrystalline polymer structure**

The aim of the simulation is to model the detailed structure of the interlamellar phase. The boundary conditions for the interlamellar phase in the z direction consist of polymer chains fixed in the crystal structure. Chains emerging from the crystal phases should be in crystallographic order and this is modelled by keeping the first 5 beads of a chain at the top and bottom faces in crystallographic phase. The chains within the interlamellar phase are required to be amorphous and still closely connected with top and bottom crystal lamellae (see Fig. 5.8). The equilibrium density of the amorphous phase is smaller than that of the crystal phase.

The generation of an initial structure satisfying these requirements is not straightforward. The construction of the top and bottom crystal lamellae is easy by simply replicating the crystal unit cell in x, y and z directions. The generation of the amorphous interlamellar phase requires much more care. Most of the available methods have been focused on the study of polymer lattice models[65],[66] rather than the off lattice polymer molecular models. We adopt a method mainly from the work of Rutledge's group.[3, 62] They were using off-lattice Monte Carlo simulation of flexible chain models to generate the amorphous interlamellar phase.

The starting point of their work is that the interlamellar phase in semicrystalline polymers is in a metastable state[67] , i.e., it can be thought of as existing in a state of local equilibrium, amenable to investigation using equilibrium statistical mechanics. The details of the off-lattice Monte Carlo method is elaborates as follows:

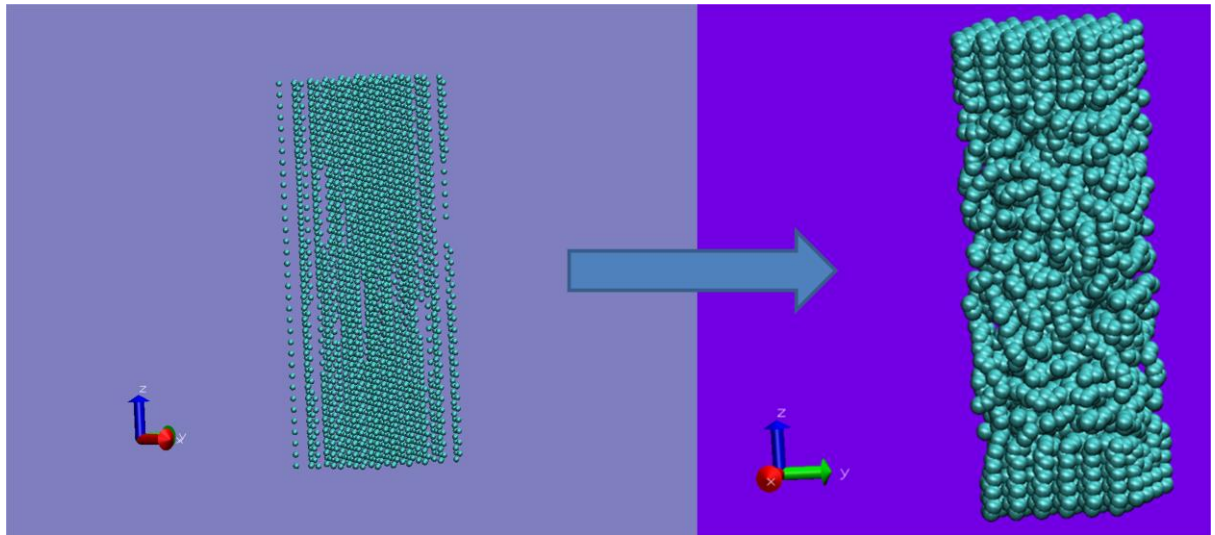


Figure 5.11 The construction of the amorphous interlamellar using the MC method.

Firstly, a polymer crystal block was constructed by replicating a required number of crystal unit cells in x, y and z direction. This polymer crystal block was viewed as all polymer chains in the all trans configuration bridging crystal sites of the two crystal lamellae. Beads between the two crystal lamellae were then removed at random to create enough free volume to match the average amorphous polymer density. (Figure 5.11) A minimum of three beads were removed from a random bridge chain in order to accommodate a proper LJ potential distance between two newly generated chain ends. Each randomly selected bridge chain was only allowed to be cut once in order to avoid generation of free chain fragments.

Secondly, two types of Monte Carlo moves were used to equilibrate the resulting polymer structure: topology-altering moves (end-bridging and end-reptation) and site displacement moves (end-rotation, re-bridging, and single-site displacement). The topology-altering moves are responsible for sampling topological degrees of freedom. By topology we mean the distribution of chain lengths and their entry and exit points at the top and bottom crystal boundaries. Chains located at the interlamellar amorphous

phase can be classified as having three different forms: bridges, which start from one crystal, pass through the amorphous region, and end in the other crystal; loops, which start from one crystal and fold back into the same crystal; tails, which start from one polymer crystal and end within the amorphous region. After the first step of deleting beads from the middle of the polymer crystal, an initial population of tails and bridges is introduced to the simulation system. By performing the topology-altering moves, both the population ratio of bridges and loops and the length distribution of bridges, loops and tails could be sampled to reach its statistical equilibrium. The site displacement moves (end-rotation, re-bridging, and single-site displacement) are responsible for achieving conformational equilibrium. By conformation we mean the three-dimensional polymer chain arrangement. In our work the site displacement MC moves were replaced with the MD dynamics.

### **End-bridging MC move**

The end-bridging move was first proposed by Pant and Theodorou for the study of amorphous polymers [68]. In this move, a three-atom segment of a chain (either loop or bridge chain only) in the vicinity of the terminus of a second, tail-type chain is excised and reconfigured to connect one branch of the first chain to the terminus of the second chain. The remaining branch of the first chain then becomes a new tail chain. As seen from Figure 5.12, a three-atom segment of a bridge chain (solid dots) is excised by cutting the two bonds connecting them. Then, it is reconfigured to connect one nearby tail branch by creating two new bonds. So, after performing the end-bridging move, a bridge chain is transformed into a loop chain. A loop chain can also be attacked by a chain end to become a bridge chain. Moreover, a loop chain can be changed into

another loop chain with a different length as well as a bridge. Therefore, it is possible to sample the population of loop chains and bridge chains, and bring the ordered crystal structure into a disordered amorphous structure. The detail of the end-bridging MC algorithm is in Appendix A.

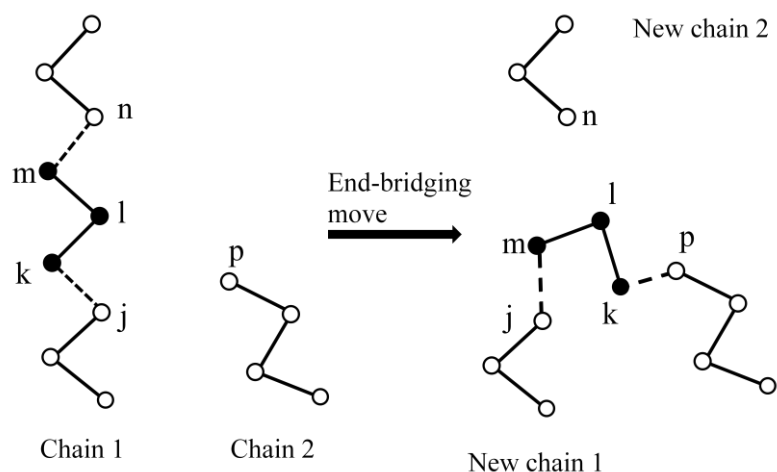


Figure 5.12 End-bridging MC move (a three-atom segment of a bridge or loop chain is excised by cutting the two bonds connecting them, and then reconfigured to connect another nearby tail branch by creating two new bonds).

According to the end-bridging MC algorithm in Appendix A, there might be several solutions for the trimer bridging problem. Microscopic reversibility is ensured by taking care to evaluate all solutions of both forward and backward trimer bridging moves. This means that not only all the solutions of trimer bridging during the *new chain 1* are calculated, but also the number of solutions of trimer bridging during the *old chain 1* is also obtained. The attempt probabilities of the forward and backward moves for an end-bridging move are given by:

$$\alpha(m \rightarrow n) = 1/N_n, \quad \alpha(n \rightarrow m) = 1/N_m$$

where  $N_n$  and  $N_m$  are the forward and backward solutions in the end-bridging algorithm.

The metropolis criteria for the acceptance of an end-bridging move are then given by:

$$P(m \rightarrow n) = \min\left[1, \frac{\alpha(n \rightarrow m) \exp(-U(n) / kT)}{\alpha(m \rightarrow n) \exp(-U(m) / kT)}\right]$$

where  $U(m)$  and  $U(n)$  are the total potential energies of the conformations in the backward and forward moves.

The general procedure of end-bridging move is:

- (a) Select a tail chain at random; for the selected end  $p$ , a corresponding bead  $j$  located at either the bridge chain or loop chain should be found. Then, the bead  $j$ 's three neighbouring atoms  $k$ ,  $l$  and  $m$  in that bridge chain or loop chain are the trimer we are looking for are found. The condition for this  $j$  is that the distance between  $j$  and  $p$  should be smaller than the maximum distance over four bonds. Thus, a scan is performed for every chain end to include all the available trimers, and these trimers are stored as a trimer list for each chain end;
- (b) To increase the end-bridging success rate, the selected chain end and all the trimer lists are tested for the end-bridging move under the above metropolis acceptance criteria  $P(m \rightarrow n)$ .
- (c) If one of the trimers in the trimer lists in the move (b) is successful, all other trimer lists are abandoned. If all the trimer lists are unsuccessful, start at (a) again and keep trying up to five times. If accepted or five attempts are exhausted, start another MD or end-reptation move.

## End-reptation MC move

The standard end-reptation method proposes a move of a bead  $m$  from one end of a tail chain  $n$  to another tail chain end  $p$ , while accepting or rejecting under the metropolis rules was used (Figure 5.13). Meanwhile, the bond length and bond angle are conserved, and only the torsional angle is selected at random during reptation, so that the chain end bead  $m$  can access a circular configuration. The detail of the numerical algorithm of replacing bead  $m$  is in Appendix B.

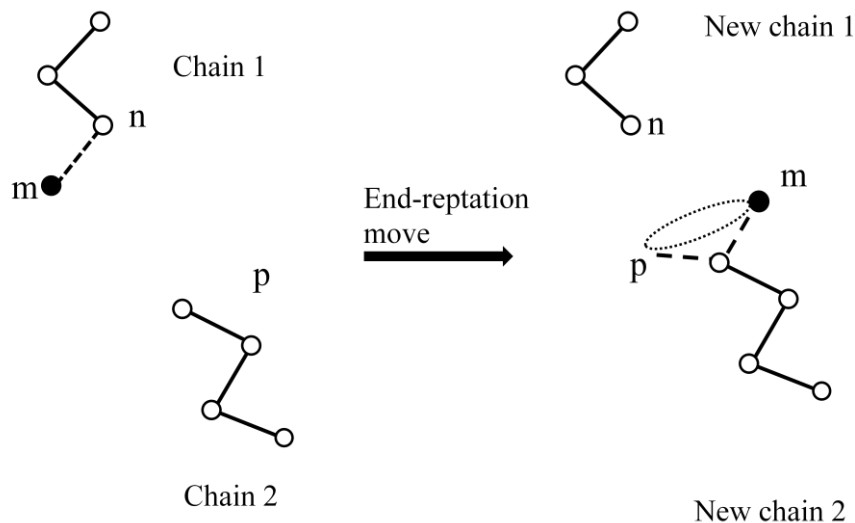


Figure 5.13 End-reptation move (one chain end bead  $m$  is excised from chain 1 and joined to another chain end, chain 2).

The metropolis criteria for the acceptance of the end-bridging move are then given by:

$$P(m \rightarrow n) = \min\left[1, \frac{\exp(-U(n)/kT)}{\exp(-U(m)/kT)}\right]$$

The general procedure of the end-reptation move is:

- (a) Select an source chain end (chain 1) at random;

- (b) Select another chain end (chain 2) again, but avoid the already selected chain end (chain 2);
- (c) Try to move the bead  $m$  from chain 1 to chain 2 with a randomly selected torsional angle under the above metropolis acceptance criteria  $P(m \rightarrow n)$ ;
- (d) If the move (c) is not accepted, try again with a new random torsion angle. Keep trying up to five times. If accepted or five attempts are exhausted, start again at (a); and
- (e) If the move (d) is not accepted, select another random chain end (chain 2) again. Keep trying up to five times. If accepted or five attempts are exhausted, start another MD move or end-bridging move.

#### **5.4.6 Computer simulation results for interlamellar phase amorphization**

Typical dimensions of simulation box in the X and Y directions are 2.96 nm and 2.8817 nm, corresponding to 4 and 6 unit cells in X and Y directions. Each unit cell contains two chains; we thus initially have 48 bridge chains in the crystal structure. The thickness of the interlamellar phase at Z direction could vary from 6-10 nm. Chain fragments were removed from randomly selected polymer chains at a random position, allowing only one fragment to be removed from any given chain. The length and the number of chain fragments deleted varied from case to case, but the initial average interlamellar density was maintained as the same 0.88 g/cm<sup>3</sup> at temperature  $T = 300\text{K}$ .

We have generated many initial configurations with different numbers of deleted chain fragments and hence different numbers of chain ends within the interlamellar region. Each initial configuration was then equilibrated using MD and the topology-altering

MC moves: both the end-bridging moves and the end-reptation moves were attempted every 200 MD steps, each MD step is about  $9.6136 \times 10^{-16}$  s. The acceptance rate of the end-bridging moves is small ( $\sim 0.2\%$ ), but the changes in the system topology brought on by these MC moves are significant. As can be seen from Figure 5.14, the interlamellar phase acquires completely disordered morphology. Meanwhile, the total chain population is not changed. The number of chain ends does not change either. The population of chain loops and chain bridges can change since loops and bridges can transform into each other via the end-bridging moves. The chain length distribution varies as well due to the end-reptation moves.

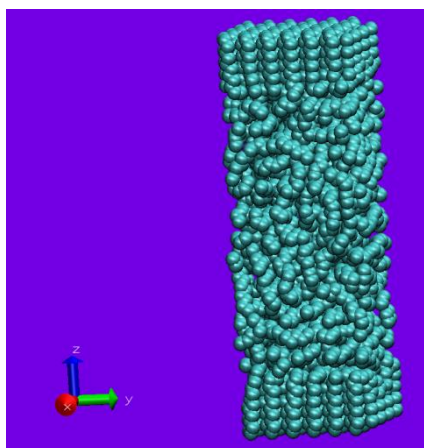


Figure 5.14 The atomistic picture of the semicrystalline polymer interlamellar domain (the amorphous chains between two small polymer crystal lamellars).

### **Chain composition in the interlamellar region**

After the amorphization process, the interlamellar region consists of different types of chains: loops, bridges and tails as expected. Each type of chains is plotted in 3D pictures. Figure 5.15 shows how a bridge chain starts from one crystal, passes through the amorphous region and ends in another crystal. Figure 5.16 shows how a tight loop starts from one crystal and immediately folds back to the same crystal. Figure 5.17 shows

how one loose loop starts from a polymer crystal, passes through the amorphous interlamellar domain and folds back to the original polymer crystal. Figure 5.18 shows how one chain tail starts from a polymer crystal, goes into the amorphous interlamellar domain before the chain ends in the amorphous region.

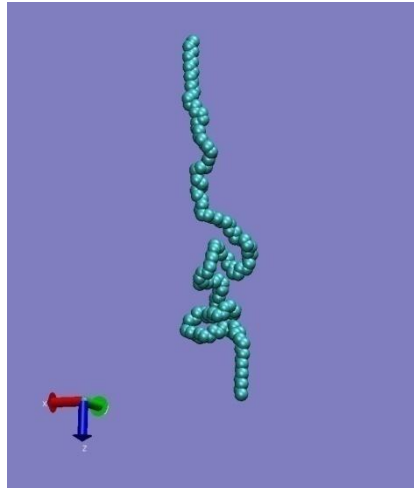


Figure 5.15 One bridge chain starts from one crystal, passes through the amorphous region and ends in another crystal.

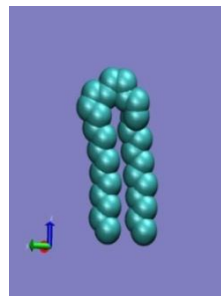


Figure 5.16 One tight loop starts from one crystal and immediately folds back to the same crystal.

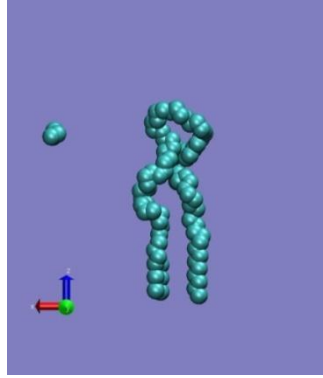


Figure 5.17 One loose loop starts from one polymer crystal, passes through the amorphous interlamellar domain and folds back to the original polymer crystal.

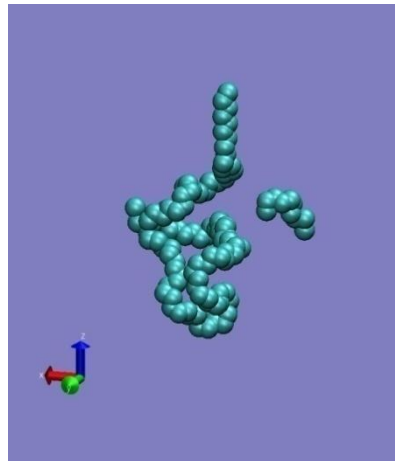


Figure 5.18 One chain tail starts from one polymer crystal, goes into the amorphous interlamellar domain before the chain ends in the amorphous region.

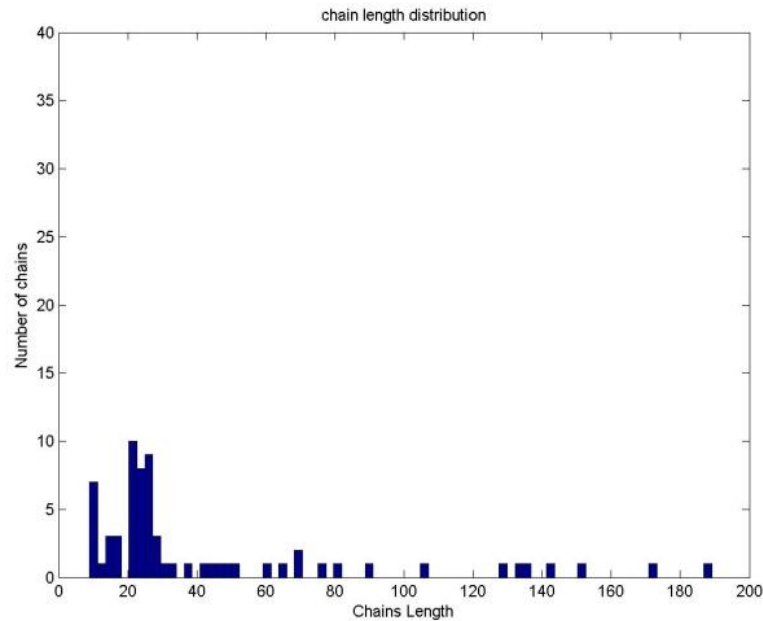


Figure 5.19 Chain length distribution map in the amorphous interlamellar region.

A typical chain length distribution map of the amorphous interlamellar region is shown in Figure 5.19. The original chain length in a bulk polymer crystal is about 60 beads. After the amorphization process, we have a wide range of chain length distribution. A peak in the small chain region indicates the large presence of tight chain loops and some short chain tails. The presence of tight chain loops is commonly found in real lamellar semicrystalline polymers[69]. Chain loops play a key role in dissipating the chain flux emanating from the polymer crystal region into the amorphous region. The bridge population is rather small, only containing about 5~10% of the chain population which is consistent with Rutledge's result [70]. Other two important compositions are loose chain loops and chain tails whose length could be up to 2-3 times the original maximum crystal chain length.

### **Density and bond orientation distribution**

To further characterize the structure of the interlamellar phase, we have calculated the density and bond orientation profiles along the z-axis. One slice of the bin normal to the z axis is scanned through the simulation box. Each scan step distance is 1/100 of the simulation box's z axis length. The width of the bin is about 0.5 nm.

The number density profile is computed by adding all the beads inside a bin and then dividing by the bin volume. It is averaged over many configurations during the simulation run. The simulation run is about 4.8068 ns and about 100 profiles are computed at regular interval. The density profile along the z-axis is show in Figure 5.20. The periodic oscillations in the crystal region indicate the regular crystal planar nature. The density increase near the crystal plateau indicates the presence of the tight loops, since the folding of the chains results in an increased number of atoms in the fold plane. Once the fold plane is crossed, the density drops down and loses its periodic nature, reflecting the disordered structure in the amorphous phase. The average amorphous density is around 0.88 gm/cc which is close to the experimental amorphous density.

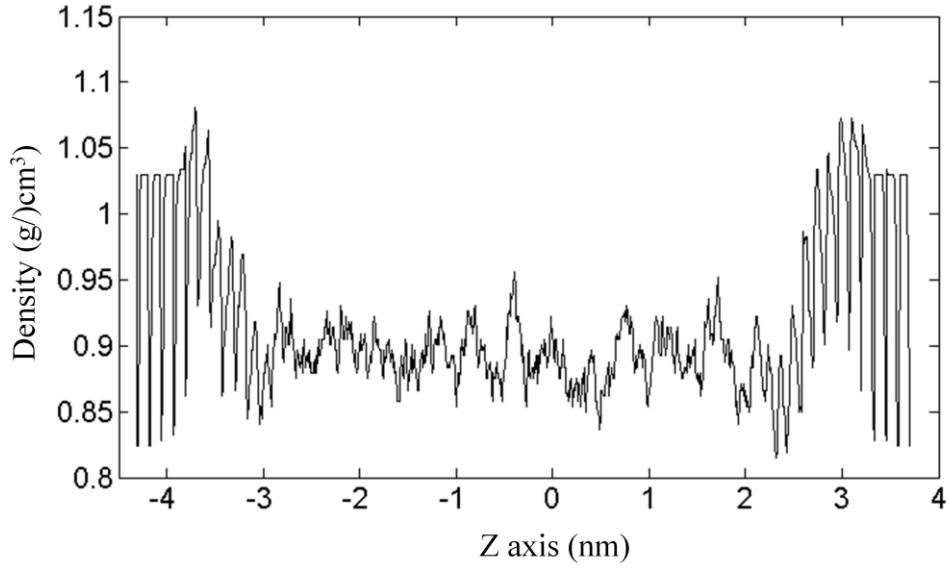


Figure 5.20 Density distribution profile along the Z axis at T = 300K

Another important way to characterize the interphase is by studying the bond orientation parameter defined as

$$S(z) = (3 \langle \cos^2 \phi(z) \rangle - 1) / 2$$

Where  $\phi$  is the angle measured by the C-C-C bond chord with respect to the z-axis, and  $\langle \dots \rangle$  represents the average over all configurations within each bin.  $S(z)$  varies in the range (-0.5, 1). Its value is close to 0 for randomly oriented bond chords. The results of our study are shown in Figure 5.21, which demonstrate a decrease in bond orientation order from the crystal region into the amorphous region. The location of the region where the bond orientation parameter decreases from its value in the crystal to zero in the amorphous phase coincides with the location of the increased number density at the tight loop fold plane.

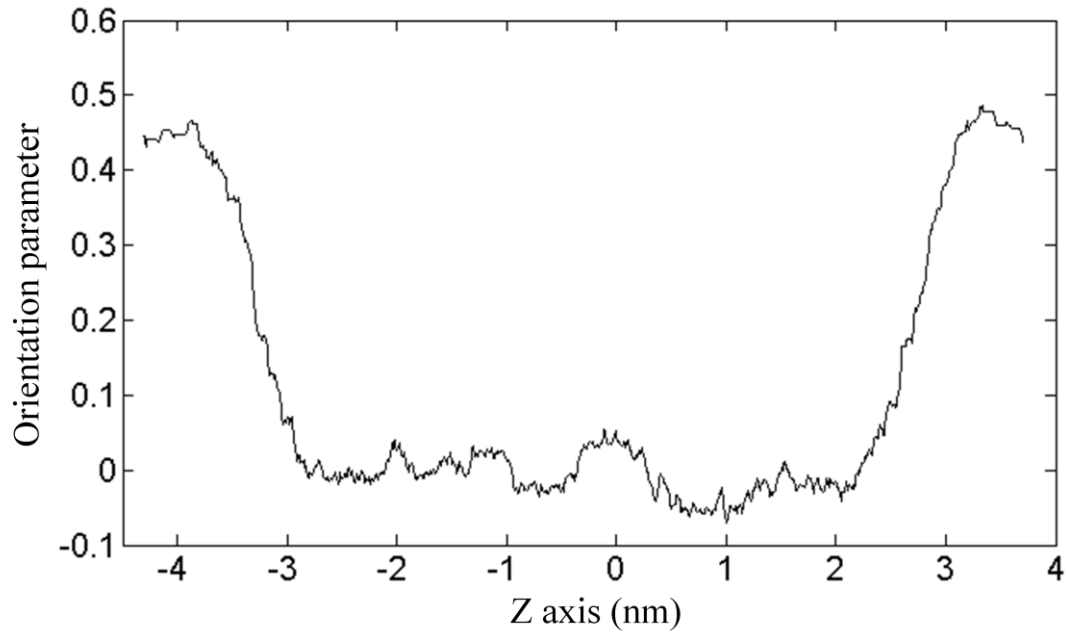


Figure 5.21 Bond orientation Order parameter distribution profile along the Z axis at  $T = 300\text{K}$

## **5.5 Mechanical properties of the interlamellar phase in semicrystalline polymers**

### **5.5.1 Deformation in the MD model**

After the equilibration of the amorphous interlamellar domain, the semicrystalline interlamellar domain was subjected to the tensile pulling test to determine its Young's modulus as well as its behaviour under stress. Because of the unique feature of our model - the presence of the rigid polymer crystal boundaries - the tensile pulling deformation procedure is carried out by simply pulling on the polymer crystal boundary rather than, as done conventionally in systems without boundaries, by scaling the whole polymer system. In semi-crystalline polymers, the mechanical properties are mostly determined by the amorphous interlamellar regions, since any deformation of the crystal regions requires much more stress. Therefore it is reasonable to consider the crystal

region as inert. Its only purpose is to transmit the pulling forces into the amorphous region. The details of the MD modelling of the tensile pulling deformation is as follows:

(Figure 5.22 shows the schematic details of the test)

- (1) Carry out constant temperature MD simulation of the semicrystalline polymer system. During the simulation, keep the bottom polymer crystal fixed
- (2) Slowly pull the rigid top crystal in the z-axis direction by updating its beads' positions every MD step. The total pulling distance is about 0.05% of the polymer bulk length in the z direction, which is small enough to ignore the volume change effect.
- (3) All the forces exerted by the amorphous region on the top crystal are summed up, including LJ potential force, covalent bond force, covalent bond angle force and torsional potential force. This total force  $F_{up}$  divided by the x-y cross-section area determines the stress due to the deformation of the interlamellar amorphous domain.
- (4) The stress  $F_{up} / A$  is plotted against the strain every 200 MD steps (Figure 5.23). The Young's modulus is then calculated using linear regression. (the linear regression method is elaborated in Appendix C).

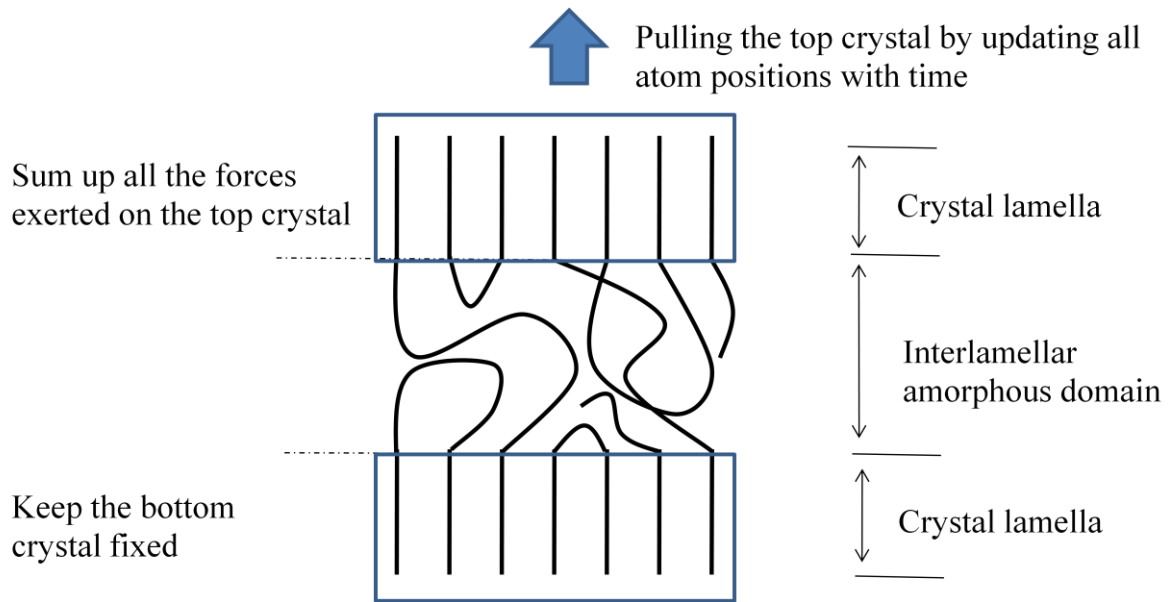


Figure 5.22 Schematic details of Molecular Dynamics modelling of tensile pulling test of semi-crystalline polymer

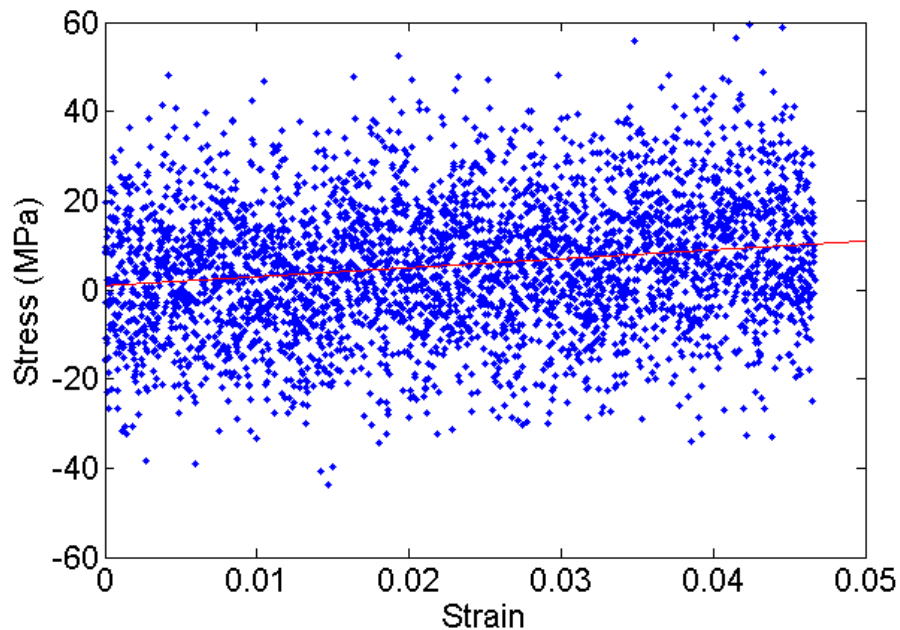


Figure 5.23 The stress in the interlamellar region as a function of the strain applied to it by the pulling deformation. The straight red line is calculated using linear regression. Its slope determines Young's modulus of the interlamellar region.

### 5.5.2 Determination of the glass transition temperature

The glass transition temperature  $T_g$  is one of the most important characteristics of amorphous polymers. Mechanical properties of amorphous polymers below and above  $T_g$  are very different: when the temperature is below  $T_g$ , the polymer material is very hard and brittle and shows plastic behaviour; when the temperature is above  $T_g$ , the polymer material exhibits elastic behaviour. Therefore, it is important to determine the glass transition temperature for the simulated polymer system. Since the polymer system we are modelling is described by an approximate united atom PE model, it is inappropriate to use the  $T_g$  determined experimentally for real PE. There are also several MD simulation studies determining PE's  $T_g$  in the literature.[71],[72] However, since these studies have been carried out on bulk systems, films, or networks and simulations were run under different conditions and with different potential parameters, it is inappropriate to compare them with our model, especially since our polymer system has a semi-crystalline nature. Therefore, we have performed MD simulations at different temperatures in order to estimate the glass transition temperature of our system.

The approximate melting point of the united atom model of PE  $T_m$  is around 410k.[60], so the glass transition temperature should be below  $T_m$ . After generating the initial configuration of the semicrystalline system, eleven different temperatures were selected to perform constant temperature MD simulation:  $T=\{200K, 220K, 240K, 260K, 280K, 300K, 320K, 340K, 360K, 380K, 400K\}$ . The interlamellar phase was first equilibrated for 24 ns. After equilibration, the Young's modulus of semicrystalline polymer at each temperature was calculated.

Figure 5.24 presents the equilibrium volume of amorphous interlamellar phase and its Young's modulus at different temperatures. The volume appears to increase linearly

with temperature with different slopes below and above around  $T = 360\text{-}380\text{K}$ . At low temperatures, the Young's modulus drops quickly with increasing temperature up to a turning point at around  $T = 360\text{-}380\text{K}$ , above which the Young's modulus starts to increase with the temperature. The change of the Young's modulus dependence on temperature could be explained by the Gough-Joule effect which predicts that the polymer's Young's modulus should decrease as temperature increases while the polymer is in the glassy state. This is because all the polymer chains in the glassy state are frozen within a local potential energy minimum, so the Young's modulus is mainly determined by the stiffness of the inter-atomic interactions. On the other hand, the Young's modulus of a polymer in the elastomer state should increase with temperature due to a large entropic effect: the entropy theory predicts that Young's modulus should be proportional to temperature. Thus, the turning point in the temperature dependence of Young's modulus is associated with the glass transition temperature.

As a result, we estimate the glass transition temperature for our semicrystalline polymer system to be around  $T_g = 360\text{K}\text{-}380\text{K}$ . This simulation not only provides us with the glass transition temperature, but also confirms the amorphous nature of the semicrystalline region.

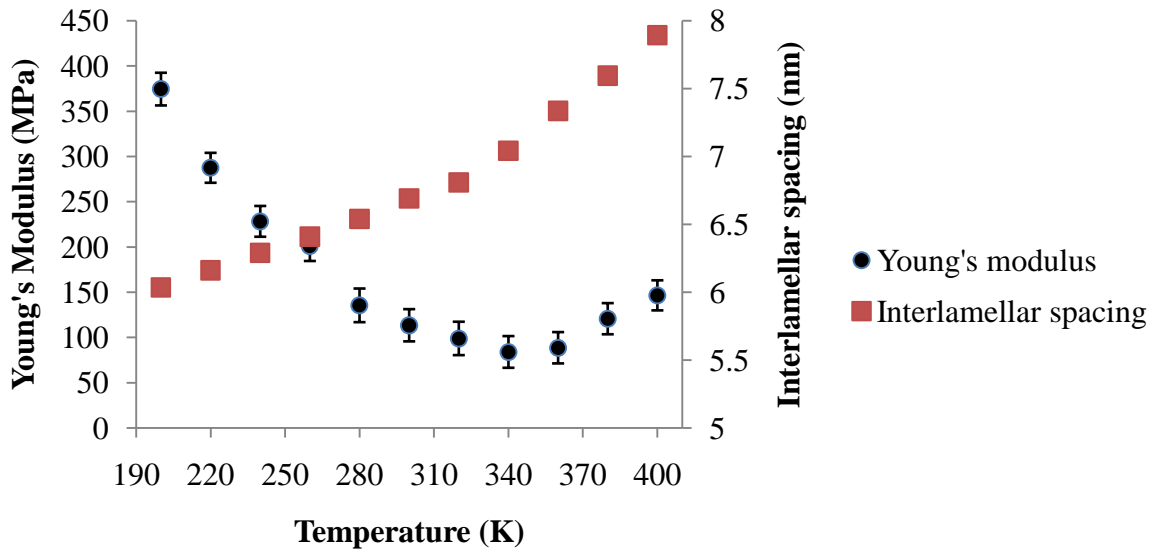


Figure 5.24 Young's modulus and volume change of semicrystalline polymer as a function of the temperature

### 5.5.3 Mechanical properties of semicrystalline polymers under $T_g$

#### Analysis of internal energy change during deformation

The total energy of the system in a molecular dynamics simulation consists of two parts: kinetic energy and potential energy. It is instructive to monitor the energy change during MD simulation. For a constant temperature MD simulation, the average kinetic energy should stay constant because it is proportional to the system temperature:

$$T = \frac{2}{n} \langle E_k \rangle$$

where  $T$  is the temperature,  $n$  is the degree of the dimensions and  $\langle E_k \rangle$  is the average kinetic energy [1].

The tensile test MD simulation of semicrystalline polymers is a constant temperature MD simulation. Figures 5.25 and 5.26 monitor the kinetic energy and potential energy

change during the tensile test MD simulation at a temperature under  $T_g$  (300K) and above  $T_g$  (390K). As expected, the kinetic energy remains constant because of the constant temperature MD setup. However, both Figures 5.25 and 5.26 reveal that the potential energy increases as the semicrystalline polymer deforms at temperatures under  $T_g$  and above  $T_g$ . This indicates that there is an internal energy change in both the glassy polymer state and elastomer state. Thus, this amorphous semicrystalline interlamellar phase is not an ideal elastomer when the temperature is above the glass transition temperature.

To look further into the potential energy change during deformation, all four different types of potential energies – covalent bond potential, covalent bond angle potential, torsional potential and LJ potential – are monitored separately. As seen in Figure 5.27, only the LJ potential energy (blue line) increased during deformation, whereas the others remained almost constant. This suggests that only the LJ inter-chain interaction governs the stress change during interlamellar region deformation. The other three intra-chain interactions do not contribute to stress generation during deformation. Therefore, there is no polymer chain stretching including bond stretching or bond angle stretching involved in interlamellar region deformation. In other words, no straight bridge chains exist in the interlamellar phase. The mechanical stiffness of the semicrystalline interlamellar region is mainly dominated by weak van der Waal forces. The contribution from polymer chain stretching (bond stretching and/or bond angle deformation) is insignificant, which can be interpreted as the absence of straight bridge chains in the interlamellar phase.

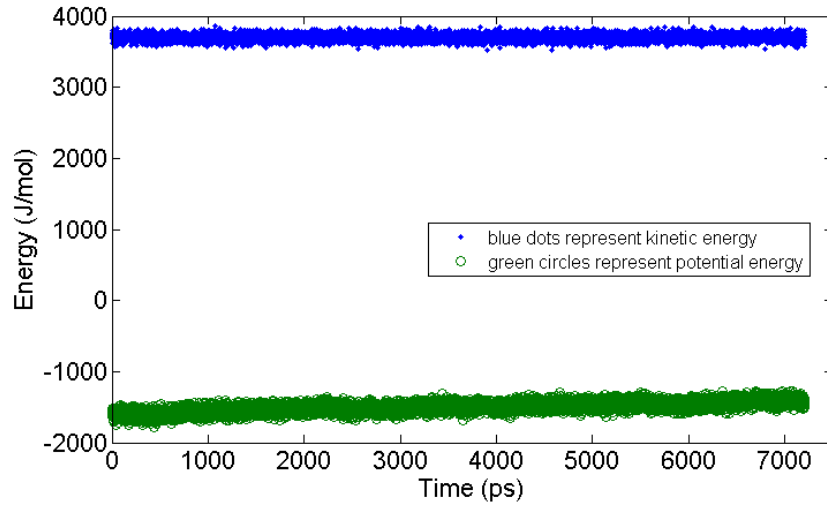


Figure 5.25 Kinetic and potential energy change during the tensile pulling simulation at temperature  $T = 300$  K which is below the estimated glass transition temperature  $T_g$

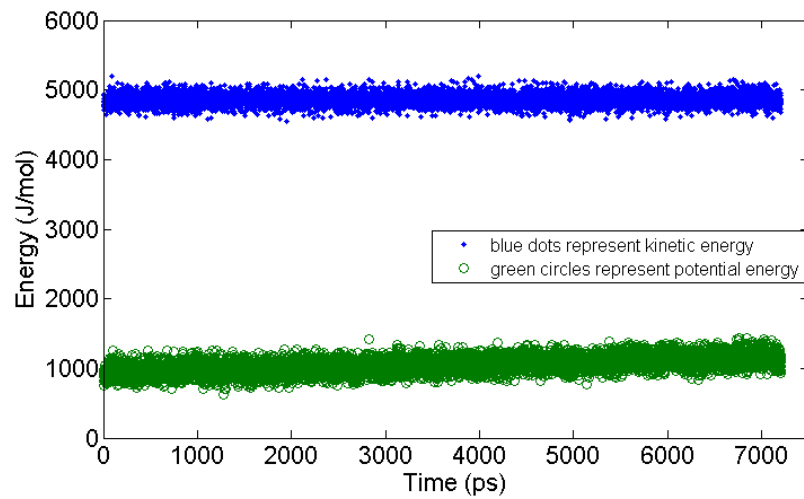


Figure 5.26 Kinetic and potential energy change during the tensile pulling simulation at temperature  $T = 390$  K, which is above  $T_g$

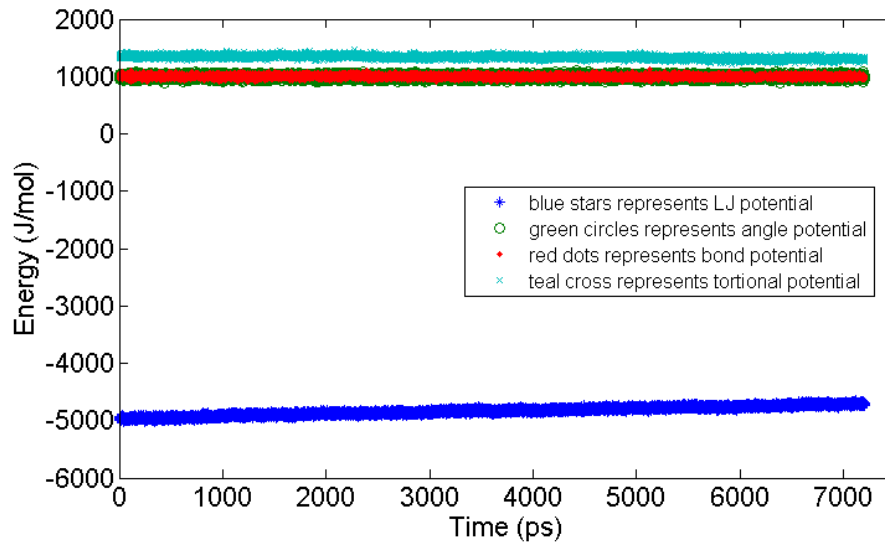


Figure 5.27 Separate contributions of different interatomic potentials to the total potential energy change during the tensile pulling test of the interlamellar region at  $T = 300\text{K}$

### Effect of interlamellar density and chain ends density

In the very initial polymer crystal before the MC amorphisation process, different numbers of crystal chain bridges were cut in different cases. Therefore, different cases contained different numbers of chain ends. During the MC amorphisation process, only the number of chain loops and chain bridges transfer between each other. The number of chain ends inside the interlamellar phase can be controlled and investigated. The number of chain ends divided by the bulk volume is regarded here as the chain ends density.

Figure 5.28 shows the semicrystalline interlamellar average density is almost linear with the number of chain ends per unit volume. At the atomic level, every tail chain contains one chain end bead. This chain end atom has only one covalent bond neighbour atom compared with other middle chain atoms that have two covalent bond neighbour atoms. In this way, the chain end atom enjoys more free volume than the other middle chain

atoms. Within the same amount of volume, a higher number of chains ends would definitely have more free volume inside the system, which leads to a lower mass density.

The average density versus Young's modulus is then examined. Firstly, the interlamellar variation is small (between 0.85~0.89), which indicates that the MC amorphization is successful. By contrast, the Young's modulus of the interlamellar phase shows only a little dependence on the interlamellar mass density at temperature  $T = 300\text{K}$  (Figure 5.29).

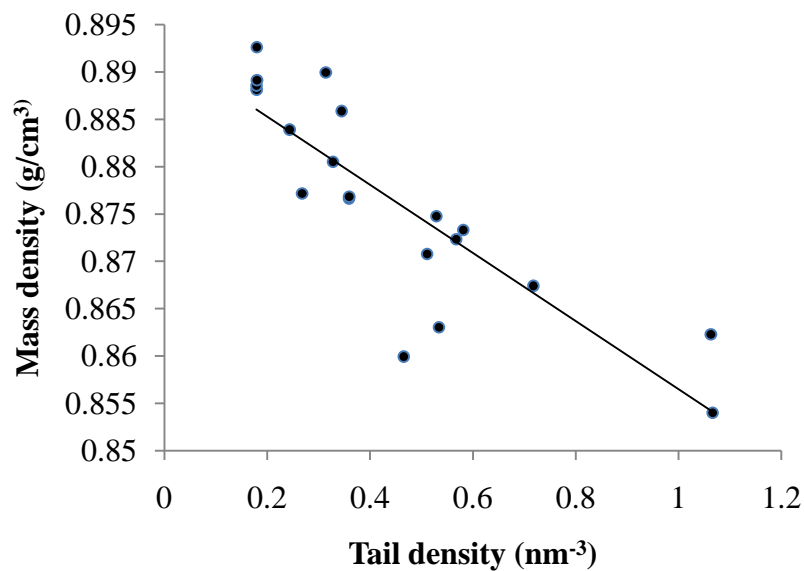


Figure 5.28 The interlamellar density of semicrystalline polymers as a function of the chain ends density (the solid line is presented as a guide line).

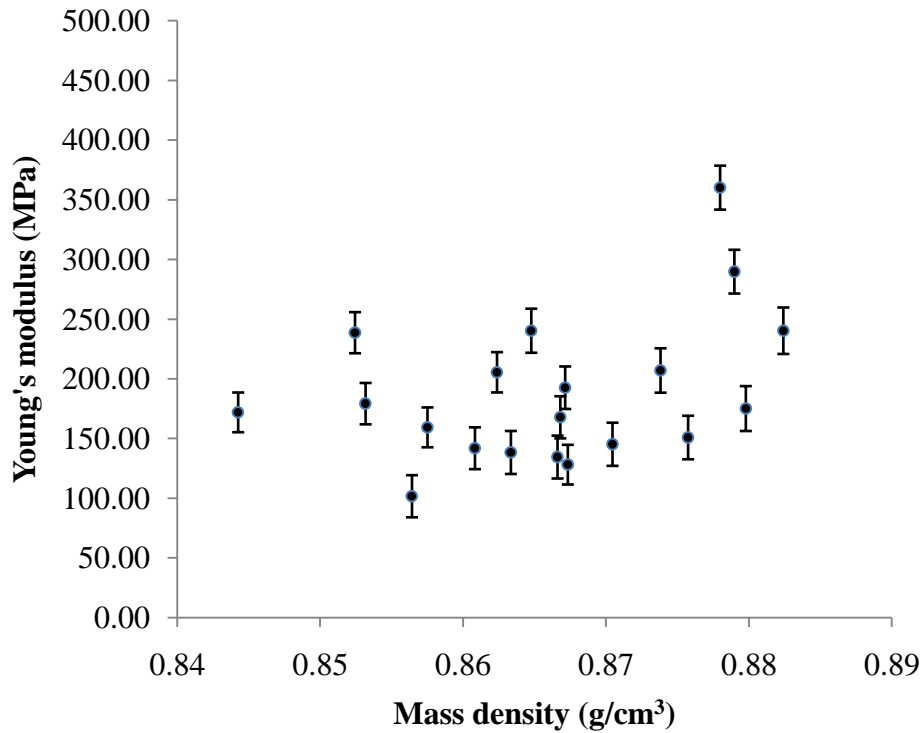


Figure 5.29 Young's modulus of semicrystalline polymers as a function of the interlamellar density under Tg.

### The effect of chain entanglement

As commonly known, the mechanical stiffness of amorphous chains is directly related to the degree of polymer chain entanglement.[59] However, the explicit microscopic definition of the concept of “chain entanglement” is not always clear. Since we already know that stress change during interlamellar deformation is caused mainly by the LJ interaction between the polymer chains, we define the “chain entanglement” based on the number of LJ “bonds” between chains connected to the top crystal lamella (let's call them “top chains”) and chains connected to the bottom lamella (“bottom chains”).

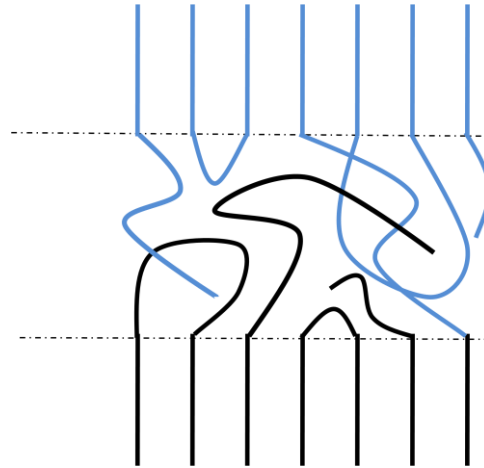


Figure 5.30 A schematic illustration of the entanglement of chains within the interlamellar region. The chains connected to the top lamella (“top chains”) are coloured blue, while the remaining chains are coloured black. The number of LJ bonds is counted between the top chains and the remaining chains

The reasoning behind counting only the number of bonds between chains connected to different crystal lamellae is as follows. During the interlamellar deformation process, the top crystal lamella moves up and all the polymer chains connected to it by the covalent bonds will be pulled away from the interlamellar phase. (Figure 5.30) The resistance to this pull will be provided mainly by the LJ interaction of the top chains with the bottom chains, as well as with the bridge chains, which for the purpose of defining LJ bonds are classified as both top and bottom. We say that two monomers form an LJ bond if the distance between them is smaller than the LJ interaction cut-off radius. The degree of entanglement of interlamellar chains is characterised by the number of LJ bonds between top and bottom chains per unit volume of the interlamellar region, i.e. the number density of LJ bonds.

As can be seen from Figure 5.31, the Young's modulus of semicrystalline polymer increases with the number density of LJ bonds. Higher number density indicates better entanglement of top and bottom chains, which results in a higher Young's modulus.

We have also investigated the effect of the thickness of interlamellar region by simulating systems with different distances between crystal lamellae:  $d = 6\text{nm}$ ,  $8\text{nm}$ , and  $10\text{nm}$ . The result is shown in Figure 5.31. It shows that the larger the interlamellar distance is, the smaller the Young's modulus of the interlamellar region will be. In real bulk semicrystalline polymer, smaller interlamellar distance implies higher crystallinity. And the semicrystalline polymer with higher crystallinity usually has higher Young's modulus. Therefore, our results appear to support this observation. The microscopic explanation behind this result can be given in terms of the properties of interlamellar region immediately adjacent to the crystal lamellae. As was shown in Figure 5.20, this region has a higher density compared to the middle of the amorphous phase, and thus has a higher number density of LJ bonds.

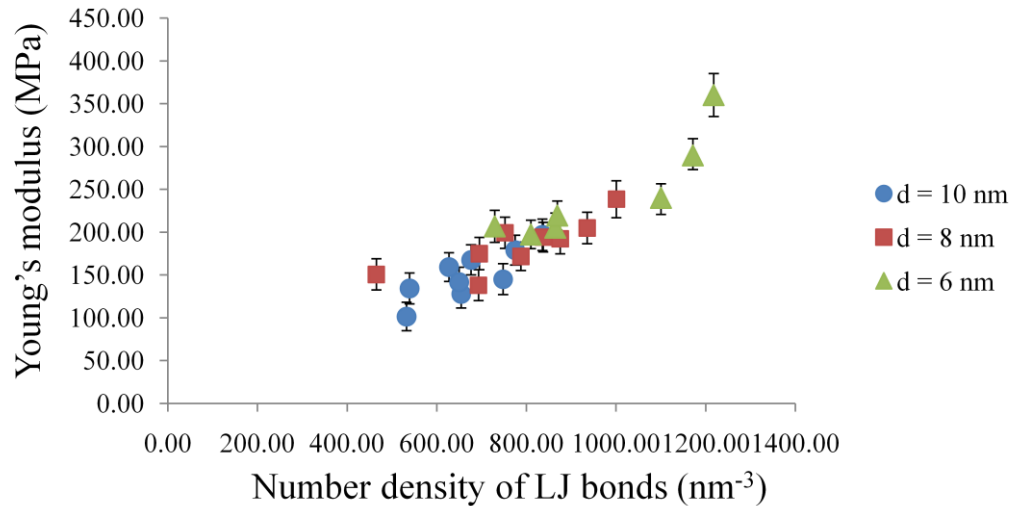


Figure 5.31 Young's modulus of interlamellar phase as a function of the density of LJ bonds between top chain beads and the rest of chain beads at  $T = 300\text{K}$ . Different symbols represent results for systems with different sizes,  $d$ , of the interlamellar region: circles for  $d = 10\text{ nm}$ , squares for  $d = 8\text{ nm}$  and triangles for  $d = 6\text{ nm}$ .

#### 5.5.4 The mechanical property of semicrystalline polymers above $T_g$

##### Young's modulus vs. the number of chains per unit volume

According to the entropy spring theory,[59] when amorphous polymer is at a temperature above  $T_g$  – the elastomer state, the mechanical stiffness is mostly driven by the entropy reduction of stretched polymer chains. In our simulations, we found that the Young's modulus of semicrystalline polymer is only dependent on the density of *long chains* inside the amorphous interlamellar region. Here *long chains* refer to those chains whose length is longer than approximately 30 polymer beads. Figure 5.32 shows a chain length distribution of all chains inside the interlamellar region, including chain tails, chain loops, and chain bridges. The straight crystal bridge chain length of this polymer system in the  $z$  direction is about 70 beads. As can be seen from the figure, the peak in

the  $a$  interval of chain lengths indicates that there is a large number of chains inside the interlamellar region which are much shorter than half the length of the straight crystal bridge. Majority of the short chains are tight chain loops which make up around 70% of the short chain population. During the interlamellar deformation, these short chains don't deform much. Most of the deformation comes from the longer chains which are located in the  $b$  interval in Figure 5.32. Therefore, the entropy reduction contribution from the short chains can be ignored.

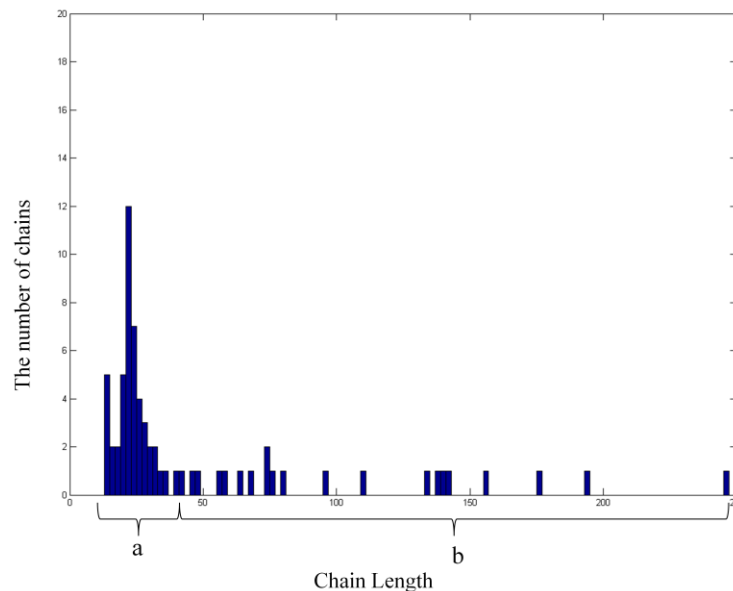


Figure 5.32 Chain length distribution (including all types of chains: loops, bridges, and tails). Chains in the interval  $a$  are recognized as short, while chains in the interval  $b$  are recognized as long. The temperature of the system is  $T = 390\text{K}$ .

By excluding the short chains, we found that the Young's modulus of semicrystalline polymer in the elastomer state is a linear function of the number of long chains per unit volume (see Figure 5.33). This is in agreement with Ward's entropy theory about the amorphous polymer above  $T_g$ . Besides, it is also found that narrower interlamellar regions have stronger Young's modulus at temperatures above  $T_g$ . This is mainly



the polymer chains, although the LJ interaction also gives some contribution. Only the torsion potential does not contribute to the stress change during crystal deformation.

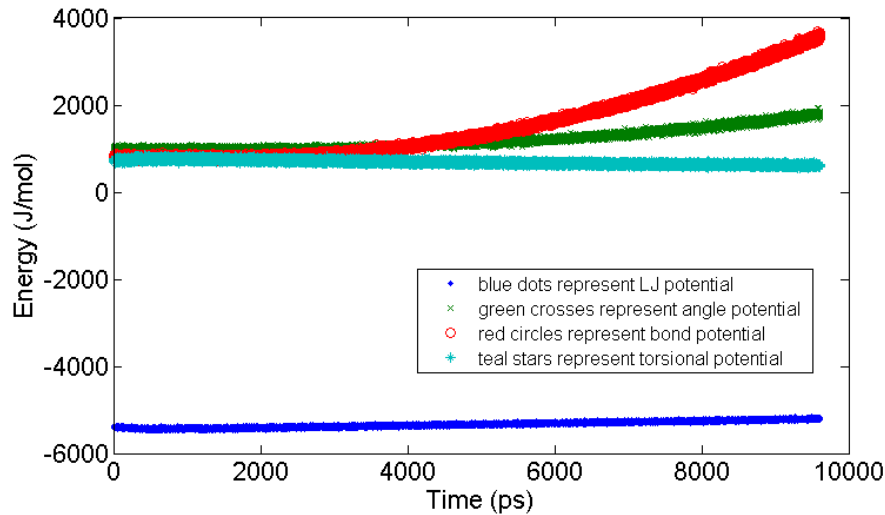


Figure 5.34 Separate contributions of different interatomic potentials to the total potential energy change during the tensile pulling test of the a crystal lamella at  $T = 300\text{K}$

Figure 5.35 illustrates the Young's modulus of a crystal lamella as a function of the number of chains at temperature  $T = 300\text{K}$ . The crystal lamella thickness is  $d = 10\text{ nm}$ . The number of chains inside the same size crystal lamella decreased from 48 to 1, and the x-y cross section area is kept constant as the crystal lamella which contains full 48 chains. The Young's modulus of crystal the lamellae at z-axis could increase from 312 MPa to 16500 MPa. The linear relationship between Young's modulus of crystal lamellar and the number of crystal chains indicates that the elasticity of individual chain obey Hooke's law. If we compare the previous Young's modulus of amorphous interlamellar phase with the Young's modulus of crystal lamellar at the same size, the modulus of the crystal lamellar is much larger than the modulus of the amorphous phase. This is why the main deformation comes from the interlamellar region when

semicrystalline polymer is under stress. We also find that a single straight polymer chains can support as much stress as the whole interlamellar region we studied above. Therefore, if there are straight chains (the straight chain bridges) inside the amorphous interlamellar, the Young's modulus of such an amorphous interlamellar phase could be considerably reinforced.

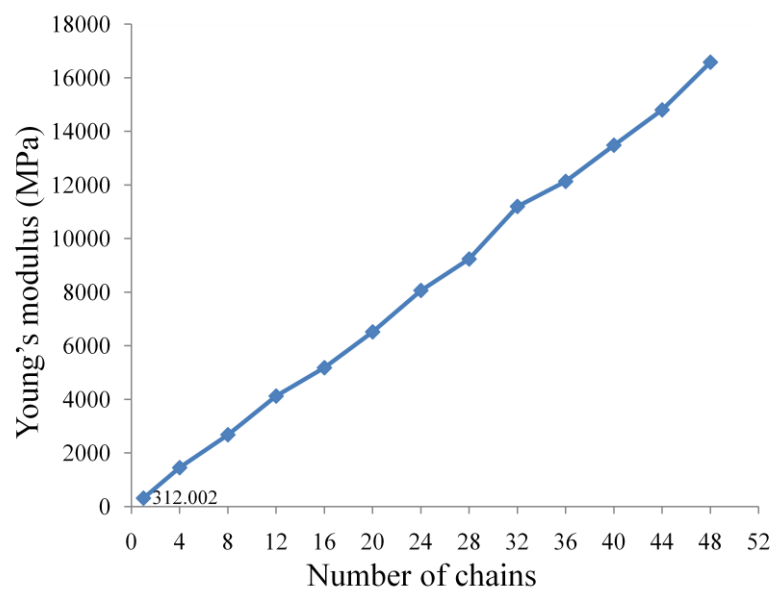


Figure 5.35 Young's modulus of crystal lamellae as a function of the number of crystal chains at temperature  $T = 300\text{K}$ . The crystal thickness is  $d = 10\text{ nm}$ .

## 5.6 Conclusions

An atomistic model has been presented to characterise both the morphology and mechanical behaviour of the interlamellar phase of semicrystalline polymers. The interlamellar phase of semicrystalline polymers consists of chain loops, chain tails and several loose chain bridges and shows a amorphous polymer nature. By analysing the potential energy change during the interlamellar phase deformation process, it was

observed that internal energy increased in both the glassy state and rubbery state of the amorphous interlamellar phase. This indicates that the amorphous interlamellar phase above the glass transition temperature is not the ideal elastomer. Moreover, the internal energy change during polymer deformation only involved the LJ potential energy change (the intra-chain interaction). No polymer chain stretching (which would trigger the inter-chain interaction potential change: bond potential, angle potential) was observed.

It was also found that the mechanical stiffness of the interlamellar phase under  $T_g$  is mainly governed by the LJ interaction friction along the polymer backbone. Therefore, good polymer chain entanglement enhances the LJ interaction friction and increases the Young's modulus. Although the amorphous interlamellar phase is not the ideal elastomer when the temperature is above the glass transition temperature, it also shows elastomer behaviour above  $T_g$  because the number of long chains inside the amorphous interlamellar phase is proportional to its Young's modulus. If tie-chains (straight chain bridges) exist inside the amorphous interlamellar phase, the modulus of semicrystalline polymers could be considerably reinforced.

## **Chapter 6      A Molecular Model for Mechanical Behaviour of a Degrading Polymer Undergoing Chain Cleavage**

### ***6.1 Introduction to semicrystalline biodegradable polymers***

The field of biodegradable polymers is a fast growing area of polymer science because of the interest in such compounds for surgical and pharmacological use. Since the introduction of the first biodegradable suture material made by synthetic biodegradable polymers in the 1960s [73], the experimental and clinical use of synthetic biodegradable polymers has grown rapidly in the fields of orthopaedics and traumatology as fracture fixation devices, in the pharmaceutical industry as drug delivery devices and, most recently, as scaffolds for tissue engineering [74],[75],[76]. Biodegradable polymers are often natural or synthetic polymers that degrade over time and eventually disappear after being introduced into a living organism. This biodegradation can be achieved either physically (disintegration, dissolution) or chemically (polymer chain scission, erosion). The list of polymers evaluated with respect to the concept of biodegradable polymer is growing rapidly [77]. However, the number of synthetic polymers having reached the stage of clinical and commercial applications is still small. Among them, poly(glycolic acid) (PGA) is a very important semicrystalline polyester with good mechanical, degradative and biocompatibility properties. PGA and its copolymer have been mainly used as a temporary support device that provides an artificial mechanical support when the original tissue bed is broken or weakened by disease, injury or surgery; for example, the bone fixation device or suture [41]. This type of device should be able to take the load instead of the tissue and gradually transfer it back as the tissue heals. As the biodegradable bone fixation implant starts to degrade, the Young's modulus of this

fixation device should start to decrease as well. If the Young's modulus of the device reduces too fast, then the healing bone would take too much load and would be placed in danger. By contrast, if the Young's modulus reduces too slowly, the bone would be weakened by the well-known stress-shielding effect [41]. Therefore, the adjustment of the degradation rate to suit the healing environment is one of the major challenges in design. Currently, most bone fixation devices are overdesigned for safety purposes, with extra high molecular weights and degrees of crystallinity. The degradation rate is, therefore, too slow [78]. This is mainly owing to the poor understanding of the mechanical behaviour of semicrystalline PGA during degradation.

Although significant progress towards understanding PGA biodegradation has been achieved through *in vitro* experimental studies and *in vivo* clinical investigation, a coherent picture of how the mechanical behaviour evolves as PGA degrades is still not clear because of lack of important information relating to the property of the semicrystalline interlamellar region at the nano-scale level.

The current understanding about PGA and its degradation mechanism can be summarised into the following points:

a) Common PGA is a semicrystalline polymer which exhibits an elevated degree of crystallinity, around 40-55%, has a glass transition temperature between 35-40 °C and its melting point is reported to be in the range of 225-230 °C. Chatani and co-workers[79] determined the crystal lamellar structure of PGA by x-ray diffraction; the dimensions of the orthorhombic unit cell are  $a = 5.22 \text{ \AA}$ ,  $b = 6.19 \text{ \AA}$ , and  $c$  (the fiber axis) =  $7.02 \text{ \AA}$ . Two macromolecular chains in Planar zig-zag conformation passing through the unit cell permit tight molecular packing. The size of the crystal lamellar is usually several nanometres, same as the amorphous interlamellar phase.

b) After the PGA polymer device is planted inside the tissue, the degradation mechanism of PGA is believed to proceed through two main stages: during the first stage, owing to the hydrophilic property of PGA chain, the water almost immediately penetrates through PGA amorphous region, but not the crystalline zone. The reason is that the structure of the amorphous region retains quite a large volume of free space between amorphous polymer chains so that water molecules can diffuse through easily. The crystalline region is highly packed with a densely ordered crystalline structure; little or no water penetrates there. As a result, the water molecules preferentially attack the ester bonds of a PGA polymer chain in the amorphous phase, and convert the long polymer chains into short polymer chains, and eventually water-soluble chain fragments. When most of the amorphous regions have been removed by hydrolysis, the second stage of degradation starts with the hydrolytic degradation of the crystalline lattice. By the start of the second stage, the polymer has already lost almost all its tensile strength due to the weak connection between the crystal lamellars. Therefore, the second stage is recognized as the later stage of degradation with little significance. The first stage of PGA degradation is much more important to understand because it is responsible for most of the tensile load.

c) It has been found that the Young's modulus reduction lags behind the degradation.[80] During the first few weeks of degradation, the Young's modulus of PGA decreases very slowly. After a certain point, however, the Young's modulus starts to drop much more quickly. Many other biodegradable polymers, like poly (lactic acid) (PLA) and its copolymer, also exhibit this kind of behaviour: the Young's modulus reduction lags behind the reduction in the average molecular weight.[81] Most research results suggest that the average molecular weight reduction is almost linear with the polymer degradation rate, which indicates the random chain scission.[82]

d) Apart from random chain scissions, there are also end chain scissions. End chain scissions occur at the end position of a polymer chain; random scissions take place at any random ester bond of a polymer chain. Because the end chain scission only reduces one monomer in a polymer chain, its contribution to the average molecular weight reduction can almost be neglected.[82] The end chain scissions only affect the later stage of polymer degradation where the proportion of chain ends is high. However, as already stated above, the late stage is of little interest in the investigation of the mechanical properties of biodegradable polymers.

To further understand the mechanical behaviour of PGA during the degradation at the nano-scale, it is almost impossible to use only experimental techniques. The explanation of many experimental results relies heavily on the hypothetical theoretical models. In Peterlin's model,[83] it is assumed that all the crystal lamellars inside semicrystalline PGA are strongly linked together by the so-called "tie-chains" in the amorphous phase. These tie-chains are supposed to pass through several crystal and amorphous regions and they are responsible for transmitting all the tensile loads to the crystalline regions. Ultimately, these tie-chains dominate the Young's modulus of a semicrystalline PGA. By contrast, in Ward's[84] study, they argue that the interlamellar region in the semicrystalline PGA is completely amorphous. Thus, it is the amorphous regions that transmit the tensile loads to the crystalline regions. At present, there is limited information regarding the real nano-scale amorphous interlamellar phase. Thus the need for a description of interlamellar amorphous phase at atomic level during degradation is urgent. Recently, Pan and co-workers [85] developed a mathematical model to explain that the Young's modulus of semicrystalline biodegradable polymers lags behind its biodegradation progress. Figure 6.1 shows that this model proposes two concepts: that an isolated cleavage in a long polymer chain do not affect the entropy resistance to

deformation and that short polymer chains do not contribute the entropy resistance to deformation. This chapter will also further examine the entropy spring theory using the MD models.

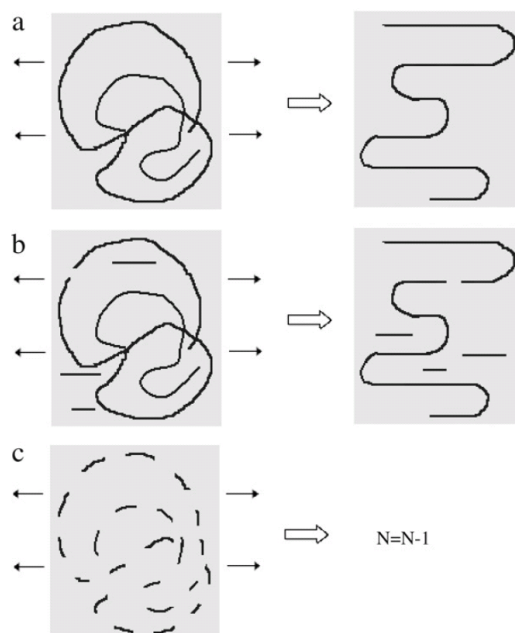


Figure 6.1 Schematic demonstration of the entropy spring model showing an initially intact polymer chain embedded in many other polymer chains, which are represented by the shaded background. (a) The entropy of the polymer chains is reduced during deformation as the long molecules become more ordered, giving an elastic resistance to the deformation. (b) Neither an isolated cleavage nor very short chains affect the entropy resistance to deformation. (c) Sufficient chain cleavages break down the polymer chain, which no longer contributes entropy resistance to deformation [85].

## 6.2 A molecular model for the mechanical behaviour of a degrading polymer

To build an explicit molecular dynamics model for a biodegradable polymer such as PGA requires the calibration of all the parameters in the coarse-grained MD potentials. No such calibration is available in the literature as far as the author is aware. The calibration is a lengthy process which is beyond the time limit of this project. In this project we take the advantage of the similarities between PE and PGA.

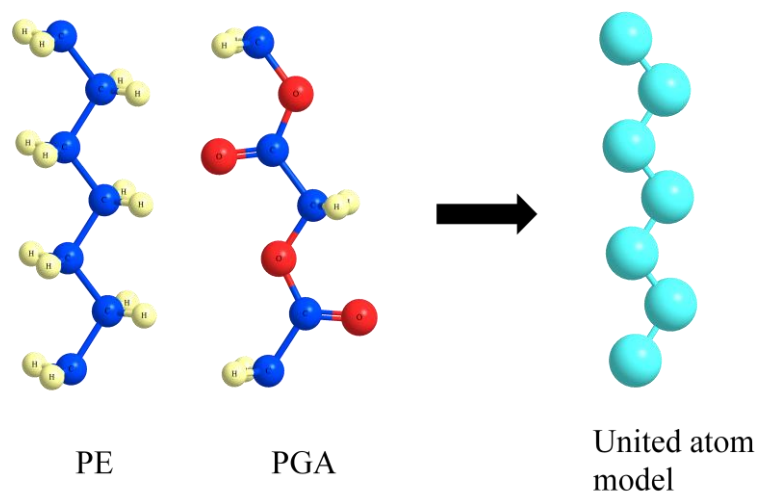


Figure 6.2 shows that both PE and PGA chains have zig-zag formation, and both of them could be simplified into a very similar zig-zag structure of united atom model, if we consider the C=O group in the PGA and the CH<sub>2</sub> group in the PGA and PE as a single “united atom”.

Both PE and PGA are semicrystalline polymers that consist of alternative polymer crystal lamellars and amorphous interlamellar regions. The crystal structures of PE and PGA are very similar as well. Both PE and PGA polymer crystals are aligned by zigzag chains (Figure 6.2) and show a very high degree of elastic anisotropy in the chain axis direction according to Ward [84].

Owing to the lack of information about the united atom model of PGA in the literature, its direct modelling is difficult. To build a united atom model of PGA from *ab initio* is again beyond the scope of this thesis. Therefore, because of the similarities between PE and PGA, we decided to mimic PGA’s mechanical behaviour during its degradation by carrying out the MD simulation of the united atom model of PE during its degradation. We are not claiming that all PE degradation simulation results should be consistent with the PGA model, but we are aiming to understand the PE-like polymer’s mechanical behaviour change and its mechanism during degradation. Therefore, we can still borrow

the semicrystalline PE structure from the previous chapter as the initial configuration of the PE degradation model. The initial configuration of this model is composed of two polymer crystals and the amorphous interlamellar phase (Figure 6.3). Because most hydrolytic degradation takes place in the amorphous interlamellar region, the two polymer crystal lamellars remain rigid and inert.

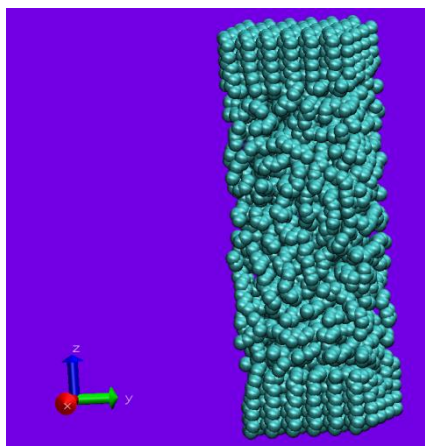


Figure 6.3 The atomistic picture of the semicrystalline polymer interlamellar domain (the amorphous chains between two small polymer crystals).

### **The degradation method of semicrystalline interlamellar phase**

The real degradation process of a PGA polymer could take up to several months, which is impossible to model with molecular dynamics simulation. However, we can use molecular dynamics to determine the properties of a system in a given state of degradation, i.e. with a given number of broken chains. Therefore, we can induce degradation in the molecular simulation by making random chain scissions within the interlamellar region and then allowing the system to relax to its equilibrium state. The main difference from the real degradation process is the absence of recrystallization, in

the molecular simulation, since this process is also too slow. The recrystallization does occur during the PGA degradation according to the literature. Nevertheless, since our aim is to investigate the mechanical behaviour of amorphous interlamellar region during degradation, we do not expect recrystallization to have any significant effect on this investigation. Even though new crystal lamellae may appear in the system due to recrystallization, the amorphous region still dominates the mechanical properties of a semicrystalline polymer.

The random chain scissions could be executed by randomly removing a covalent bond from a random chain. The two beads connecting this covalent bond will then become two new chain tails. In the case of the united atom model used in this study, such scission will result in a very strong repulsive force between the chain tails, since at the moment of scission they are located at a distance of the covalent bond length (about 0.15 nm), while their interaction is described by the LJ potential with the length parameter about 0.4 nm. To avoid such a repulsion in our model, the polymer chain degradation is modelled by randomly removing a three bead segment from a random chain.(figure 6.4) In this fashion, the new LJ interaction between two new tails is more realistic. The mass loss of these three beads could be simply understood as one random chain scission plus three chain end scissions. Three chain end scissions will produce three soluble monomers which will diffuse away.

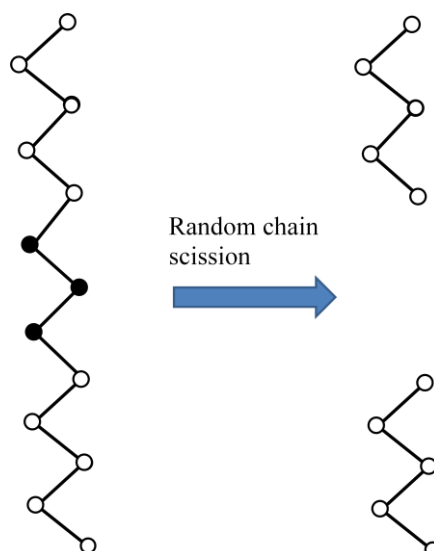


Figure 6.4 Random chain scission is carried out by removing a three-bead segment.

The random chain scissions are made in the amorphous interlamellar region during a constant temperature MD simulation run. Both crystal lamellae are kept rigid and fixed. One random chain scission is made by randomly removing a three bead segment from a random chain after every 2000 MD steps. After a significant number of chain scissions, short oligomer fragments will appear in the system; since such fragments are expected to be soluble, they should be removed from the simulated system.. Many articles [86] mention that short soluble oligomers would diffuse away from the polymer system during PGA degradation, although the exact maximum length of a soluble oligomer is not known. In our simulation, any oligomer fragment whose length is smaller than 10 beads is recognized as soluble and removed from the system. It is important to point out that, unlike the real system, our simulated system does not contain water molecules or monomers. According to the literature, the friction between simple molecules and polymer chains can be modelled by Langevin dynamics. Therefore, the Langevin thermostat used for constant temperature multi-scale method (*the stadium damping* which elaborated in the previous chapter) also serves as a beads friction purpose.

After every 10 chain scissions, the state of the system was saved. With the total of about 100 chain scissions performed in the entire degradation process, 9 to 10 degradation points were saved to do further equilibration and tensile test. During the equilibration process lasting about 12 ns, the bottom crystal lamella was kept rigid and fixed; the top lamella was kept rigid, but allowed to move in the z direction subject to the total force exerted by the amorphous region. In this way, the amorphous region could be under stress free condition after the equilibration process. After the equilibration, the MD Young's modulus test was performed on each degraded system by deforming the interlamellar amorphous phase.

### **6.3 Results and discussions**

The PGA's glass transition temperature was about 30 - 40°C, which is very close to human body temperature. We also set the modelling temperature close to the glass transition temperature (about 360-380K):  $T = 390\text{K}$ . Another low temperature which is below the glass transition temperature  $T = 300\text{K}$  is also investigated.

#### **6.3.1 Morphology change in the interlamellar phase during degradation**

During polymer degradation, the alteration of the polymer chain morphology in the interlamellar region is monitored. Initially, the amorphous interlamellar phase is composed by bridge chains, loop chains and tail chains. As the degradation proceeds, the long bridge chains and long loop chains have a greater probability to be attacked by random chain scissions transforming both of them into tail chains. As can be seen from

Figure 6.5, the number of tails increases while the numbers of bridges and loops decrease initially. The reduction in the number of loops halts at some point of degradation because there remain mostly short tight loop chains near the crystal lamellae, which are less probable to be attacked by the random chain scissions. After the consumption of long bridges and loops, the raise of the number of tails also stops. The *chain fragment* is a new chain type generated by the random chain scissions of tail chains. Fragments are different from tails because they are not connected to the crystal lamellae with covalent bonds and interact with their surroundings only with the LJ potential. At the beginning of the degradation process, when the number of tails is small and random chain scissions attack mostly the loop and bridge chains, the generation of chain fragments is slow. After the depletion of long bridge and long loop chains and creation of sufficiently large number of tails, the random chain scissions mainly take place in the tails or the fragments themselves, which considerably increase the rate of fragments production. Long fragments are trapped inside the interlamellar region, while the short chain fragments, whose length is shorter than 10 beads, are considered soluble and removed from the amorphous region, causing increasing mass loss.

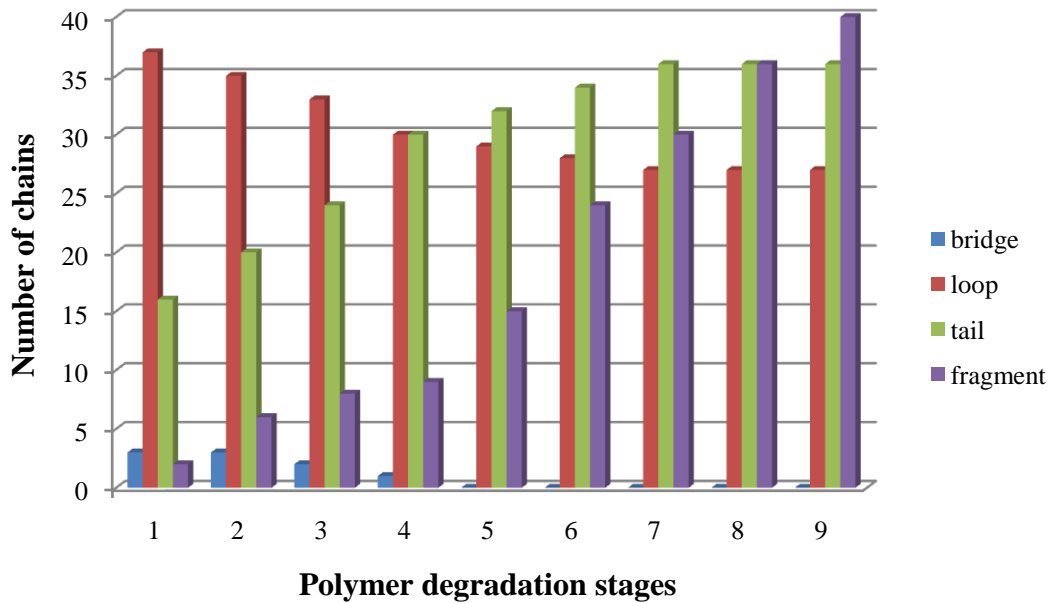


Figure 6.5 The interlamellar chain composition at nine different degradation stages. Stages are numbered from 1 to 9, with larger numbers corresponding to larger degrees of polymer degradation at  $T = 390\text{K}$ .

### 6.3.2 Mass loss

The mass loss in the interlamellar region during degradation is tracked by counting the total number of polymer beads remaining inside the region. The main cause of the mass loss is the generation of the soluble chain fragments in the later stages of the degradation. As can be seen in Figure 6.6, the mass loss is very slow at the beginning. After about 40 chain scissions, the total mass in the interlamellar region drops much faster due to the removal of the short soluble chain fragments. This phenomenon agrees well with the experimental results.[87]

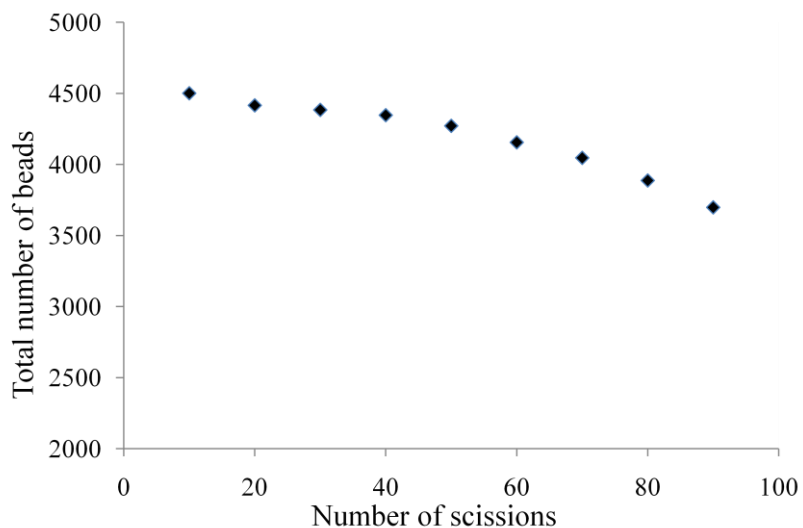


Figure 6.6 Mass loss during polymer degradation.

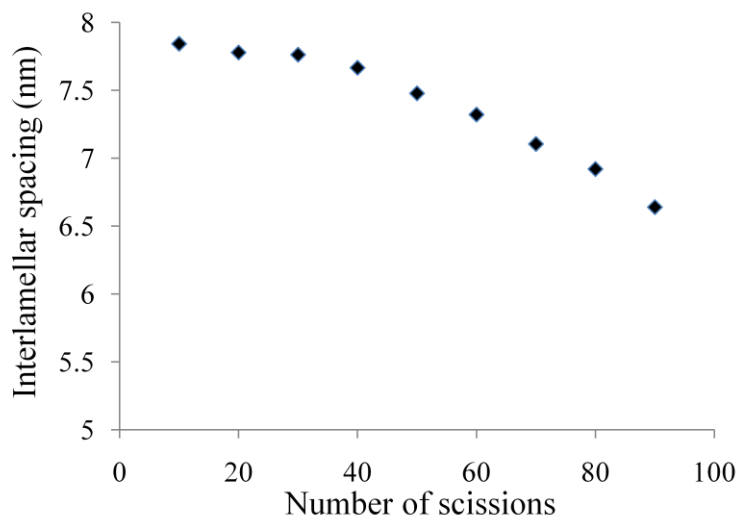


Figure 6.7 Thickness change of the interlamellar space as a function of the degradation process.

The mass loss also triggers the shrinkage of the interlamellar region. Figure 6.7 tracks the thickness change of the interlamellar region during degradation. The thickness change profile is very similar to the mass loss profile. This means that the removal of the short soluble chain fragments makes two crystal lamellars collapse toward each

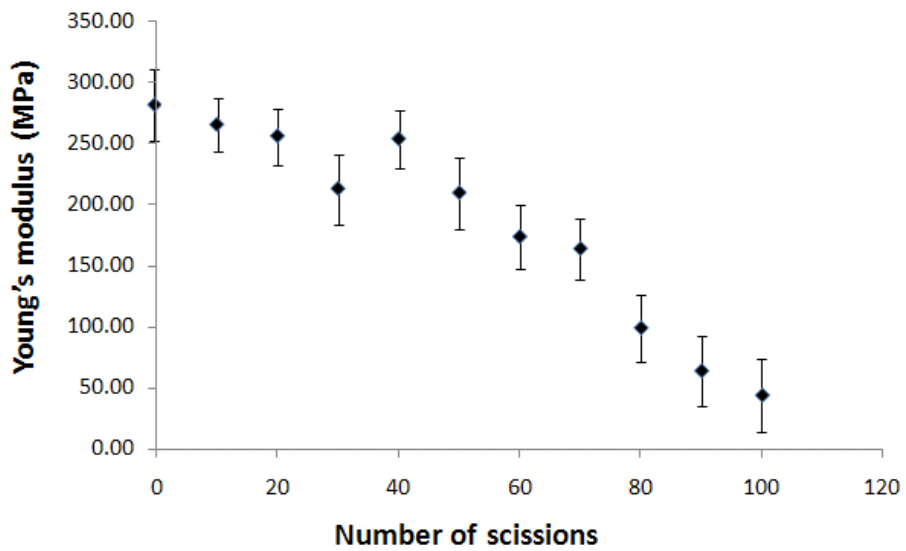
other. The shrinkage of the interlamellar region could be a very good explanation for the pores and cracks found in the real PGA degradation sample.[87]

### **6.3.3 Mechanical property change of interlamellar region during degradation above $T_g$**

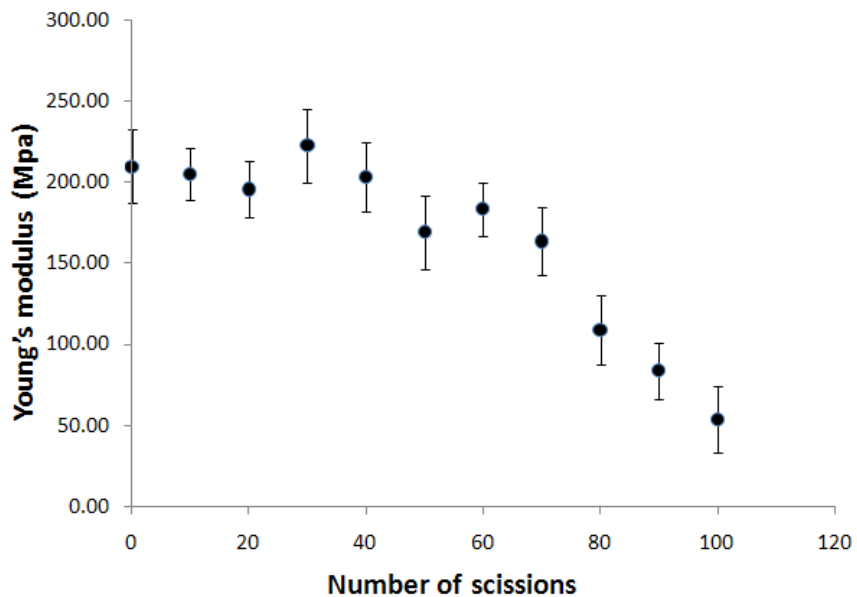
Figure 6.8 (a) and (b) illustrate the Young's modulus change of the semicrystalline phase with different thickness as a function of the number of random chain scissions at  $T = 390\text{K}$ , which is above the estimated glass transition temperature  $T_g$ . In both cases the initial Young's modulus is maintained during the early stages of degradation, although the thinner interlamellar region appears to show an earlier drop of the Young's modulus. These findings agree well with both experimental results of PGA degradation[88][89] and Pan's entropy spring model[85].

In both PGA in vitro degradation experiment and Pan's entropy spring model, Young's modulus is maintained during the first few weeks of the degradation process. This phenomenon is in contrast with elastomer's entropy theory by Ward[59]. Most long chains are attacked by the random chain scissions at the beginning of the degradation. The number of long chains should decrease very fast initially. According to Ward's elastomer's entropy theory, the Young's modulus should decrease as well. Pan's entropy spring model further complements Ward's entropy theory. It states that when a long polymer chain is attacked by an isolated chain scission, the total entropy of the two newly generated chains does not change. This is because the entire configuration of the two newly generated chains does not differ significantly from the configuration of the original chain: They remain trapped by all other polymer chains surrounding them. In Pan's model, they call this a "no-rise" rule. As an illustration, Figure 6.9 shows one

long polymer chain embedded inside the interlamellar phase after it degraded into two new chains. Two newly generated chain ends (marked in yellow circle) still stay close to each other after 5 nanoseconds equilibration which indicates that polymer chains rearrangement is very difficult inside the polymer matrix.



(a)



(b)

Figure 6.8 Young's modulus of biodegradable polymer as a function of the number of chain scissions at  $T = 390\text{K}$ : (a) the interlamellar thickness  $d = 6 \text{ nm}$ . (b) the interlamellar thickness  $d = 8\text{nm}$ .

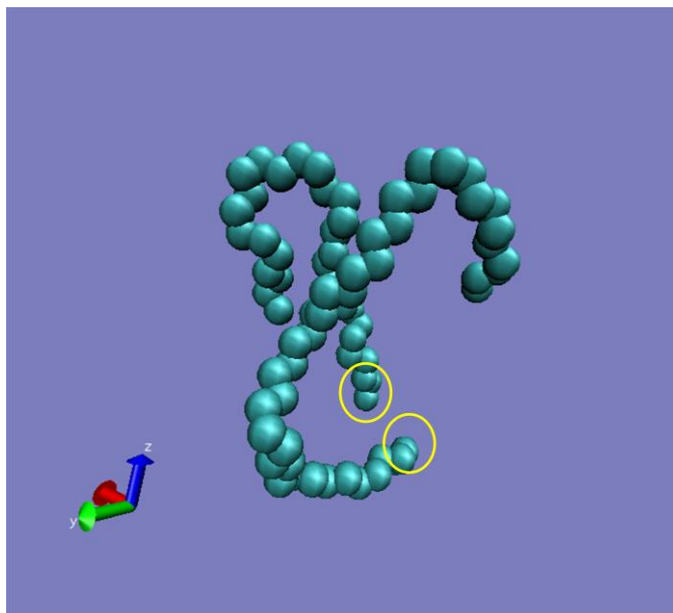


Figure 6.9 One long polymer chain embedded inside the interlamellar phase after it degraded into two new chains (all other chains are represented by shadow area, Those small chain fragments is connected with the same colour chain, this happens because of the PBC condition.) Two newly generated chain ends (inside the yellow circles) still stay close to each other after 5 ns equilibration process

The Young's modulus drop is owing to the generation of the short polymer chains. Another assumption made by Pan's entropy spring model is that the short chains do not contribute to the entropy change during deformation. The thinner interlamellar regions generally contain shorter polymer chains. Therefore, it is reasonable that short polymer chains will appear early in the thinner interlamellar regions. As a result, the Young's modulus drop will occur earlier in the thinner interlamellar region. Thinner interlamellar regions could be considered as a contributing factor to the high crystallinity in the semicrystalline polymer. The real biodegradation experiment of biodegradable polymers often reveals that higher crystallinity leads to early drop of the Young's modulus of

semicrystalline polymer.[90] The early drop of Young's modulus in thinner interlamellar phase may be a good explanation of this phenomenon.

### **6.3.4 Mechanical property change of interlamellar region during degradation below $T_g$**

The mechanical property change of interlamellar region during degradation below  $T_g$  is investigated by carrying out the degradation of a semicrystalline interlamellar phase of thickness  $d= 8$  nm at  $T = 300$ K. Figure 6.10 illustrates the Young's modulus change as a function of the number of chain scissions. The Young's modulus drops quickly with the increasing number of random chain scissions.

This phenomenon is explained by two reasons. First one is the concept of degree of entanglement which was fully explained in the previous chapter. As we already know, the Young's modulus of semicrystalline polymer in a glassy state is mainly dominated by the LJ bonds between polymer chains, which is an indication of how well the polymer chains entangle with each other. All the polymer chains connected to the crystal lamellae transmit their polymer beads' LJ interaction forces to their crystal lamellae. When a chain fragment is taken off a chain connected to a crystal lamella, this chain fragment also takes away all the LJ interaction forces contributing to that crystal lamellar. It could be concluded that random chain scissions quickly reduce the entanglement of amorphous chains. Another reason is the decrease of interlamellar density. Even though this decrease is small, it still contributes to the reduction of the density of LJ bonds.

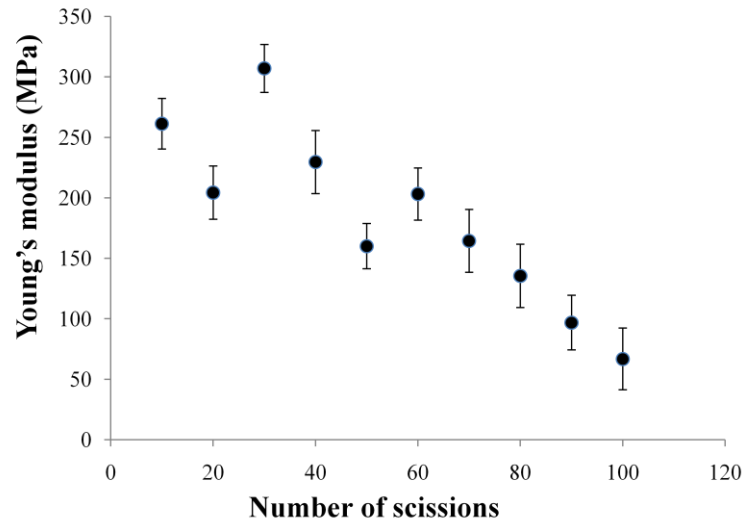


Figure 6.10 Young's modulus of biodegradable polymer with the interlamellar thickness  $d = 8$  nm as a function of the number of chain scissions at temperature  $T = 300\text{K}$  which is below the glass transition temperature

## **6.4 Conclusions**

This chapter investigates the mechanisms behind the mechanical behaviour change of semicrystalline PGA's biodegradation by carrying out the MD simulation of the degradation of the united atomistic model of the semicrystalline Polyethylene whose polymer morphology and polymer chain structure are very similar to PGA.

It is found that the mechanical stiffness of interlamellar phase below  $T_g$  is mainly governed by the LJ interaction friction along the polymer backbone. Therefore, good polymer chain entanglement enhances the LJ interaction friction and increases the stiffness. The results of this study further support Pan's entropy spring theory by showing the Young's modulus drop lags behind the biodegradation process at temperatures above the glass transition temperature. For the amorphous interlamellar phase below the glass transition temperature, the Young's modulus drops quickly as the chain scissions quickly reduce the polymer chain entanglement.

## Chapter 7 Conclusions

In this work, the behaviour of nano-structured materials that is controlled by the interface is studied using molecular dynamics. The four objectives of this thesis were: (1) to investigate the sintering behaviour of nanoparticle; (2) to investigate the evolution of bamboo-like nanowires; (3) to study the mechanical property of the interlamellar phase of semicrystalline polymers; and (4) to study the mechanical property of the interlamellar phase of biodegradable polymers. All the four objectives have been achieved satisfactory and presented in this thesis. The major contributions of this work to the understanding of materials behaviour can be summarised as follows:

- ❖ A multi-scale MD simulation code capable of modelling a variety of nanostructured materials has been created. This MD code was initially developed to model 2D fcc nanocrystals to address the evolution of nanoparticle sintering. When studying the evolution of bamboo-like nanowires, this MD code was further extended to modelling 3D fcc nanocrystals at a constant temperature. At the same time, a multi-scale concept was introduced into this MD code so that the majority part of the bulk crystals could be modelled as a rigid phase. This multi-scale MD simulation reduces the computational time without compromising modelling accuracy because the interfaces fully modelled and the interaction between the bulk and the interfaces is maintained. In the second stage of this work, the multi-scale MD simulation code was developed to model semicrystalline polymers. The main difference between polymer and polycrystal is the polymer chain, which consists of polymer beads and covalent bonds. Three coarse grained potential functions – covalent bond potential, angle

potential and torsional potential – along with the new neighbour list method were introduced into the code to model the polymer chains. Furthermore, an MC algorithm was incorporated created to generate the initial configuration of the amorphous interlamellar phase.

- ❖ We found that the surface diffusion and GB diffusion are the main mass transport mechanisms in both fcc nanoparticle interaction and fcc nanowire evolution. Both diffusion processes are sensitive to temperature, with a higher temperature increasing the diffusion coefficient. The surface diffusion seems to contribute more under low temperatures, while the GB diffusion dominates under high temperatures. GB migration also occurs at at temperatures.
- ❖ The elimination of low angle GB was observed for both nanoparticle interaction and nanowire evolution. At the nano-scale level, because of the large volume fraction of high energy interfaces, materials have a stronger tendency to reduce their energies. This tendency can help nanocrystals to eliminate the low angle GB by reorienting their crystallographic orientations to form a low energy perfect bulk crystal during nanoparticle sintering. For the evolution of bamboo-like nanowires, a perfect bending nanocrystal was formed at a low temperature after eliminating the low angle GB. Dislocation slip planes were found which nucleate from the convex or concave points of this bending structure at high temperatures. Once the dislocation slip had been introduced into the nanowire, plastic deformation reduces the length of the nanowire and thereby the total surface energy.
- ❖ High angle GBs were found to be stable in nanowires with relatively large diameters (about 7 nm) at low temperatures. However, the high angle GB in the nanowires with small diameters (5 nm) showed that a new hcp grain can be

nucleated and grow from the triple point where the GB meets the surface boundary. The diffusion coefficient of the high angle GB at high temperatures is very fast. Obvious grain coarsening and invasion were found at high temperatures with high angle GBs.

- ❖ The stiffness of the amorphous interlamellar phase was found to be much weaker than the polymer crystals as expected. For the complete amorphous interlamellar phase in the semicrystalline polymer, it was found that its stiffness under  $T_g$  is mainly governed by the LJ interaction along the polymer backbone. Therefore, good polymer chain entanglement enhances the LJ interaction and increases stiffness. Although the amorphous interlamellar phase is not the ideal elastomer when the temperature is above the glass transition temperature, it also shows that the elastomer behaviour above  $T_g$  is because the number of long chains inside the amorphous interlamellar phase is proportional to its Young's modulus. If tie-chains (straight chain bridges) exist inside the amorphous interlamellar phase, the modulus of semicrystalline polymers can be considerably reinforced.
- ❖ For biodegradable semicrystalline polymers, this research further proved entropy spring theory due to Pan by showing the Young's modulus drop significantly lags behind the biodegradation process at a temperature above the glass transition temperature. For the amorphous interlamellar phase under the glass transition temperature, the Young's modulus drops quickly as the chain cleavage quickly reduce polymer chain entanglement.

## Reference

- [1] D. Rapaport, *The Art of Molecular Dynamics Simulation*, Second Edition, 2004, p. 350 pp.
- [2] A. C. F. C. J. Pan, *Acta metall. mater.* 43 (1995) 1395-1406.
- [3] S. Balijepalli, G. C. Rutledge, *Macromolecular Symposia* 133 (1998) 71-99.
- [4] H. Gleiter, *Progress in Materials Science* 33 (1989) 223-315.
- [5] K. E. Gonsalves, S. P. Rangarajan, J. Wang, *Chemical synthesis of nanostructured metals, metal alloys, and semiconductors*, 2000, p. 1-56.
- [6] R. M. German, *Sintering Theory and Practice*, John Wiley & Sons, Inc., New York, 1996.
- [7] H. N. Ch'ng, J. Pan, *Acta Materialia* 55 (2007) 813-824.
- [8] H. Zhu, R. S. Averbach, *Materials Science & Engineering, A: Structural Materials: Properties, Microstructure and Processing A204* (1995) 96-100.
- [9] P. Zeng, S. Zajac, P. C. Clapp, J. A. Rifkin, *Materials Science & Engineering, A: Structural Materials: Properties, Microstructure and Processing A252* (1998) 301-306.
- [10] J. S. Raut, R. B. Bhagat, K. A. Fichthorn, *Nanostructured Materials* 10 (1998) 837-851.
- [11] K. Tsuruta, A. Omeltchenko, R. K. Kalia, P. Vashishta, *Europhysics Letters* 33 (1996) 441-446.
- [12] C. Herring, *Journal of Applied Physics* 21 (1950) 301-303.
- [13] W. D. Kingery, *Journal of Applied Physics* 30 (1959) 301-306.
- [14] R. L. Coble, *Journal of Applied Physics* 32 (1961) 787-792.
- [15] M. F. Ashby, *Acta Metallurgica* 22 (1974) 275-289.
- [16] I. W. Chen, X. H. Wang, *Nature (London)* 404 (2000) 168-171.
- [17] D. Janezic, F. Merzel, *Journal of Chemical Information and Computer Sciences* 35 (1995) 321-326.
- [18] J. E. C. Lennard-Jones, *Proceedings of the Physical Society* 43 (1931) 461.
- [19] W. G. Hoover, Ladd, A.J.C, Moran, B. , *Phys. Rev. Lett.* 48 (1982) 1818.
- [20] J. Rankin, B. W. Sheldon, *Materials Science & Engineering, A: Structural Materials: Properties, Microstructure and Processing A204* (1995) 48-53.
- [21] J. A. Barker, D. Henderson, F. F. Abraham, *Physica A: Statistical Mechanics and Its Applications (Amsterdam, Netherlands)* 106A (1981) 226-238.
- [22] G. M. Odegard, T. S. Gates, L. M. Nicholson, K. E. Wise, *Composites Science and Technology* 62 (2002) 1869-1880.
- [23] J. Wang, B. L. Karihaloo, H. L. Duan, *Bulletin of the Polish Academy of Sciences: Technical Sciences* 55 (2007) 133-140.
- [24] W. E. Kingston, Editor, *The Physics of Powder Metallurgy*, 1951, p. 404 pp.
- [25] Herring, *Surface tension as a motivation for sintering*, McGraw- Hill, New York, 1955.

- [26] C. Herring, *The Physics of Powder Metallurgy*, McGraw-Hill, New York, 1951.
- [27] W. W. Mullins, *Journal of Applied Physics* 28 (1957) 333-339.
- [28] H.-J. Fecht, M. Werner, Editors, *The Nano-Micro Interface: Bridging the Micro and Nano Worlds*, 2004, p. 327 pp.
- [29] D. Raabe, J. Ge, *Scripta Materialia* 51 (2004) 915-920.
- [30] P. Yang, *MRS Bulletin* 30 (2005) 85-91.
- [31] B. Sun, Z. Suo, A. C. F. Cocks, *Journal of the Mechanics and Physics of Solids* 44 (1996) 559-581.
- [32] K. T. Miller, F. F. Lange, *Acta Metallurgica* 37 (1989) 1343-1347.
- [33] S. Qu, V. Shastri, W. A. Curtin, R. E. Miller, *Modell. Simul. Mater. Sci. Eng.* 13 (2005) 1101-1118.
- [34] B. R. Brooks, R. E. Brucoleri, B. D. Olafson, D. J. States, S. Swaminathan, M. Karplus, J. *Comput. Chem.* 4 (1983) 187-217.
- [35] D. Holland, M. Marder, *Adv. Mater. (Weinheim, Ger.)* 11 (1999) 793-806.
- [36] L. Lifshitz, *Statistical Physics Part 1*, New York, 1980, p. P 362.
- [37] K. L. Merkle, *Interface Sci.* 2 (1995) 311-345.
- [38] D. E. Spearot, M. A. Tschopp, K. I. Jacob, D. L. McDowell, *Acta Mater.* 55 (2007) 705-714.
- [39] Y. Qi, P. E. Krajewski, *Acta Mater.* 55 (2007) 1555-1563.
- [40] L. Li, J. L. Shao, S. Q. Duan, J. Q. Liang, *New Journal of Physics* 12 No pp given.
- [41] B. D. Ratner, A. S. Hoffman, F. J. Schoen, J. E. Lemons, Editors, *Biomaterials Science, An Introduction to Materials in Medicine*, 2nd Edition, 2004, p. 851 pp.
- [42] R. d. P. Daubeny, C. W. Bunn, C. J. Brown, *Proceedings of the Royal Society of London, Series A Mathematical, Physical and Engineering Sciences* 226 (1954) 531-542.
- [43] W. R. Busing, *Macromolecules* 23 (1990) 4608-4610.
- [44] Y. Chatani, *Kobunshi* 25 (1976) 550-553.
- [45] C. W. Bunn, *Transactions of the Faraday Society* 35 (1939) 482-491.
- [46] A. Keller, *Faraday Discussions of the Royal Society of Chemistry* 68 (1979) 145-166, 147 plates.
- [47] L. Mandelkern, *Accounts of Chemical Research* 23 (1990) 380-386.
- [48] L. Mandelkern, *Chemtracts Macromolecular Chemistry* 3 (1992) 347-375.
- [49] G. R. Strobl, M. Schneider, *Journal of Polymer Science, Polymer Physics Edition* 18 (1980) 1343-1359.
- [50] R. R. Eckman, P. M. Henrichs, A. J. Peacock, *Macromolecules* 30 (1997) 2474-2481.
- [51] G. R. Strobl, W. Hagedorn, *Journal of Polymer Science, Polymer Physics Edition* 16 (1978) 1181-1193.
- [52] B. Crist, J. C. Nicholson, *Polymer* 35 (1994) 1846-1854.

- [53] R. M. Christensen, K. H. Lo, *Journal of the Mechanics and Physics of Solids* 27 (1979) 315-330.
- [54] S. D. Gardner, C. U. Pittman, Jr., R. M. Hackett, *Composites Science and Technology* 46 (1993) 307-318.
- [55] E. A. DiMarzio, C. M. Guttman, *Polymer* 21 (1980) 733-744.
- [56] R. Seguela, *Journal of Polymer Science, Part B Polymer Physics* 43 (2005) 1729-1748.
- [57] F. Zuo, J. K. Keum, X. Chen, B. S. Hsiao, H. Chen, S.-Y. Lai, R. Wevers, J. Li, *Polymer* 48 (2007) 6867-6880.
- [58] F. W. Billmeyer, Jr., *Textbook of Polymer Science*. 3rd Ed, 1989, p. 276 pp.
- [59] I. M. Ward, *An Introduction to the Mechanical Properties of Solid Polymers*, Second Edition, 2004, p. 360 pp.
- [60] W. Paul, D. Y. Yoon, G. D. Smith, *Journal of Chemical Physics* 103 (1995) 1702-1709.
- [61] K. Bolton, S. B. M. Bosio, W. L. Hase, W. F. Schneider, K. C. Hass, *Journal of Physical Chemistry B* 103 (1999) 3885-3895.
- [62] P. J. In't Veld, G. C. Rutledge, *Macromolecules* 36 (2003) 7358-7365.
- [63] N. Waheed, M. S. Lavine, G. C. Rutledge, *Journal of Chemical Physics* 116 (2002) 2301-2309.
- [64] M. J. Ko, N. Waheed, M. S. Lavine, G. C. Rutledge, *Journal of Chemical Physics* 121 (2004) 2823-2832.
- [65] I. Zuniga, K. Rodrigues, W. L. Mattice, *Macromolecules* 23 (1990) 4108-4114.
- [66] M. L. Mansfield, *Macromolecules* 16 (1983) 914-920.
- [67] G. R. Strobl, Editor, *The Physics of Polymers: Concepts for Understanding their Structures and Behavior*, 1996, p. 500 pp.
- [68] P. V. K. Pant, D. N. Theodorou, *Macromolecules* 28 (1995) 7224-7234.
- [69] P. J. Flory, D. Y. Yoon, K. A. Dill, *Macromolecules* 17 (1984) 862-868.
- [70] G. C. Rutledge, *Journal of Macromolecular Science, Physics B* 41 (2002) 909-922.
- [71] J. Han, R. H. Gee, R. H. Boyd, *Macromolecules* 27 (1994) 7781-7784.
- [72] K. Van Workum, J. J. de Pablo, *Nano Letters* 3 (2003) 1405-1410.
- [73] J. C. Middleton, A. J. Tipton, *Biomaterials* 21 (2000) 2335-2346.
- [74] S. Ramakrishna, J. Mayer, E. Wintermantel, K. W. Leong, *Composites Science and Technology* 61 (2001) 1189-1224.
- [75] K. Van de Velde, P. Kiekens, *Polymer Testing* 21 (2002) 433-442.
- [76] J. F. Mano, R. A. Sousa, L. F. Boesel, N. M. Neves, R. L. Reis, *Composites Science and Technology* 64 (2004) 789-817.
- [77] D. F. Williams, *Biomaterials Science: An introduction to Materials in Medicine* by Buddy D. Ratner, 2005, p. 5093.

- [78] F. Alan Barber, B. F. Elrod, D. A. McGuire, L. E. Paulos, *Biomaterials* 21 (2000) 2623-2629.
- [79] Y. Chatani, K. Suehiro, Y. Okita, H. Tadokoro, K. Chujo, *Makromolekulare Chemie* 113 (1968) 215-229.
- [80] A. R. Katz, R. J. Turner, *Surgery, gynecology & obstetrics* 131 (1970) 701-716.
- [81] H. Tsuji, *Recent Research Developments in Polymer Science* 4 (2000) 13-37.
- [82] S. M. Li, H. Garreau, M. Vert, *Journal of Materials Science Materials in Medicine* 1 (1990) 131-139.
- [83] C. C. Chu, *Journal of Applied Polymer Science* 26 (1981) 1727-1734.
- [84] H. Montes de Oca, I. M. Ward, *Polymer* 47 (2006) 7070-7077.
- [85] Y. Wang, X. Han, J. Pan, C. Sinka, *Journal of the mechanical behavior of biomedical materials* 3 14-21.
- [86] C.-j. Kim, *Controlled Release Dosage Form Design*, 2000, p. 310 pp.
- [87] S. Shawe, F. Buchanan, E. Harkin-Jones, D. Farrar, *Journal of Materials Science* 41 (2006) 4832-4838.
- [88] B. X. Fu, B. S. Hsiao, G. Chen, J. Zhou, I. Koyfman, D. D. Jamiolkowski, E. Dormier, *Polymer* 43 (2002) 5527-5534.
- [89] X. Xu, T. Liu, S. Liu, K. Zhang, Z. Shen, Y. Li, X. Jing, *Journal of Materials Science Materials in Medicine* 20 (2009) 1167-1173.
- [90] H. Tsuji, Y. Ikada, *Polymer Degradation and Stability* 67 (1999) 179-189.

## Appendix

### Publications

1. **Ding, Lifeng;** Davidchack, Ruslan L.; Pan, Jingzhe. A molecular dynamics study of sintering between nanoparticles. *Computational Materials Science*(2009), 45(2), 247-256.
2. **Ding, Lifeng;** Davidchack, Ruslan L.; Pan, Jingzhe. A molecular dynamics study of the behaviour of polycrystalline nanowire. To be submitted to *Computational Material Science*
3. **Ding, Lifeng;** Davidchack, Ruslan L.; Pan, Jingzhe. A molecular dynamics study of biodegradable semicrystalline polymer. To be submitted to *Biomechanics*.

## Appendix A - End-bridging (EB) MC move algorithm

This appendix presents details of the end-bridging MC move algorithm

The end-bridging geometric problem to be analyzed is depicted in Figure A-1. In the EB move  $p$  is the attacking end of the tail chain 1 and  $k, l, m$  beads is the trimer to be excised from the victim bridge *chain 2*. The attacking end  $p$  is bridged to bead  $j$  of *chain 1* by inserting the trimer  $k, l, m$ .

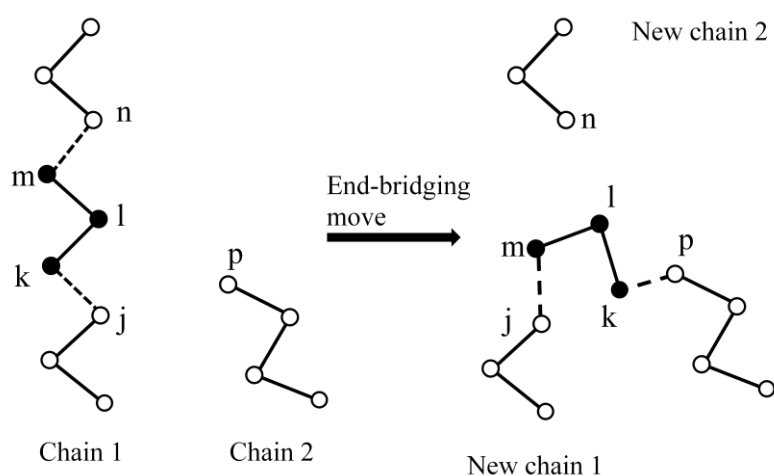


Figure A-1. End-bridging MC move (a three-atom segment of a bridge or loop chain is excised by cutting the two bonds connecting them, and then reconfigured to connect another nearby tail branch by creating two new bonds).

Therefore, the whole end-bridge move could be divided into two steps. The first step, find a trimer for all the chain end inside the interlamellar phase. The second step is rebridging the trimer  $m, l, k$  while still keep all the bond length and bond angle the same as they were in *chain 1*.

The first step is to find the rebridging chain pairs. For every chain end  $p$ , a corresponding bead  $j$  locating at either bridge chain or loop chain should be found. Then the neighbour atoms  $k, l, m$  is the trimer we are looking for. The condition for this  $j$  is that the distance between  $j$  and  $p$  should be smaller than the maximum distance over four bonds. Thus, a scan is performed for every chain end to include all the available trimers and these trimers are stored as a trimer list for each chain end. All the chain end and their trimer lists are tested for the rebridging step in order to increase the end-bridging succeeding rate. Not all the end-bridging attempt are successful, it depends on the attempt probability. This will be discussed further.

The second step is the rebridging step. Basically, it could be addressed as a geometric problem: Given two dimmers in space, connect them with a trimer, such that the resulting heptamer has prescribed bond lengths and bond angles. In the following, we will refer to this problem as the geometric problem of trimer bridging, as noted by Pant and Theodorou.[68] geometrically, the general problem of constructing a bridging trimer can be formulated by considering figure A-2. Given the two dimmers  $(r_0, r_1)$  and  $(r_5, r_6)$  in space, the goal is to join them by a trimer  $(r_2, r_3, r_4)$ , such that all the bond lengths and bond angles are conserved.

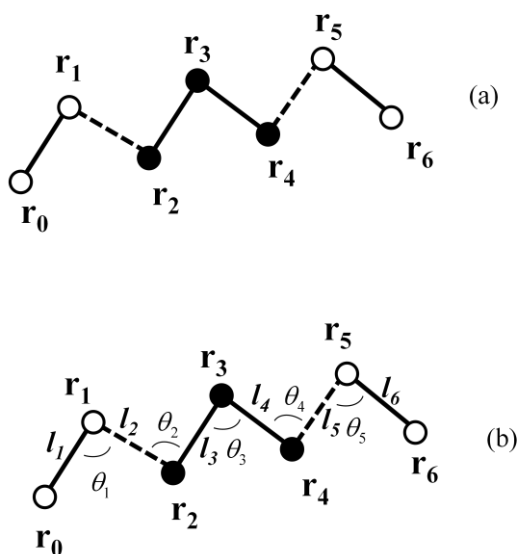


Figure A-2 Bridging of two dimmers with a trimer. (a) Trimer  $(r_2, r_3, r_4)$  which bridges dimmers  $(r_0, r_1)$  and  $(r_5, r_6)$ . (b) Bond lengths and bond angles that are specified in the bridging construction.

In order to determine the coordinates of this trimer  $(r_2, r_3, r_4)$ , we have to solve nine degrees of freedom: the nine components of the tree trimer bead positions  $(r_2, r_3, r_4)$ . On the other hand, we have nine different constrains must be conserved:  $l_2, l_3, l_4, l_5, \theta_1, \theta_2, \theta_3, \theta_4, \theta_5$ . Therefore, it is possible to determine the coordinates of this timer by casting nine different equations in nine unknowns.

However, solving these nine equations is not an easy task. Pant and Theodorou.[68] developed a method with less complication. Basically, they try to reduce this nine unknowns problem to a problem of three equations in three unknown angular degrees of freedom. Firstly, the nine constrain  $(l_2, l_3, l_4, l_5, \theta_1, \theta_2, \theta_3, \theta_4, \theta_5)$  is translated into another form  $(l_2, l_3, l_4, l_5, \theta_1, l_{13}, \theta_3, l_{35}, \theta_5)$ . The angles  $\theta_2$  and  $\theta_4$  are replaced by  $l_{13}$ : the distance between *beads* 1 and 3,  $l_{35}$ : the distance between *beads* 3 and 5. The nine components of the trimer  $(r_2, r_3, r_4)$ 's positions are then described by six bridging  $(l_2, l_5, \theta_1, l_{13}, l_{35}, \theta_5)$  along with three unknown angular variable. With  $r_0$  and  $r_1$  fixed in space

and  $l_2$  and  $\theta_1$  specified, the locus of  $r_2$  is a circle  $C_2$  lying in a plane normal to the line connecting  $r_0$  and  $r_1$ , with its center on that line. Similarly, with  $r_5$  and  $r_6$  fixed in space and  $l_5$  and  $\theta_5$  specified, the locus of  $r_4$  is a circle  $C_4$  lying in a plane normal to the line connecting  $r_6$  and  $r_5$ , with its center on that line (see Figure A-3). To describe the positions of  $r_2$  and  $r_4$  along  $C_2$  and  $C_4$ , respectively, it is convenient to introduce two fixed reference points, the rotation angle  $\phi_L$  is defined as the dihedral angle between planes  $(r_L, r_0, r_1)$  and  $(r_0, r_1, r_2)$ . Similarly, with the introduction of the second reference point,  $r_R$ , the rotation angle  $\phi_R$  is defined as the dihedral angle between planes  $(r_5, r_6, r_R)$  and  $(r_4, r_5, r_6)$ . By varying the dihedral angles  $\phi_L$  and  $\phi_R$ , one causes  $r_2$  and  $r_4$  to sweep out their loci  $C_2$  and  $C_4$ , respectively. The reference position  $r_L$  and  $r_R$  is take  $r_L = r_{-1}$  and  $r_R = r_7$  (positions of skeletal beads preceding  $r_0$  and following  $r_6$  along the chain).

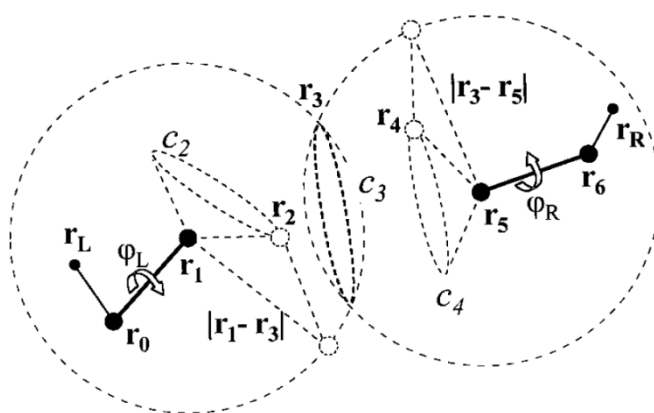


Figure A-3 Schematic of the trimer bridging geometric solution. Shaded atoms are stationary. Fixed, but otherwise arbitrary, reference positions  $r_L$  and  $r_R$  are used to define torsion angles  $\phi_L$  and  $\phi_R$  on the left (L) and right (R) sides of the bridge, respectively. Rotations of  $\phi_L$  and  $\phi_R$  sweep out the loci of  $r_2$  and  $r_4$  (short dashed circles  $C_2$  and  $C_4$ ), respectively. The lengths of segments  $(r_1, r_3)$  and  $(r_3, r_5)$  constitute the radii (long dashed lines) of spheres centered at  $r_1$  and  $r_5$ , respectively; these segment lengths are known from the chain bonding geometry. Position  $r_3$  must lie on the intersection (heavy dashed circle  $C_3$ ) of these two spheres. Points  $r_2$ ,  $r_3$ , and  $r_4$  on  $C_2$ ,  $C_3$ , and  $C_4$  which satisfy constraints trimer define solutions to the EB problem.

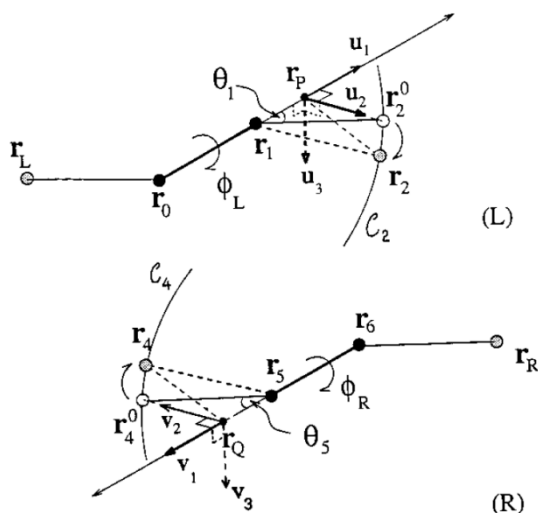


Figure A-4 Frames of reference for the left- (L) and right-(R) sides of the trimer bridging problem. The position  $r_2$  is expressed in frame  $[u_1, u_2, u_3]$  with origin  $r_p$ . The position  $r_4$  is expressed in frame  $[v_1, v_2, v_3]$  with origin  $r_Q$ . Angles  $\theta_1$  and  $\theta_5$  are the bond angle supplements at vertices  $r_1$  and  $r_5$ , respectively. All solid straight lines in the figure are coplanar.

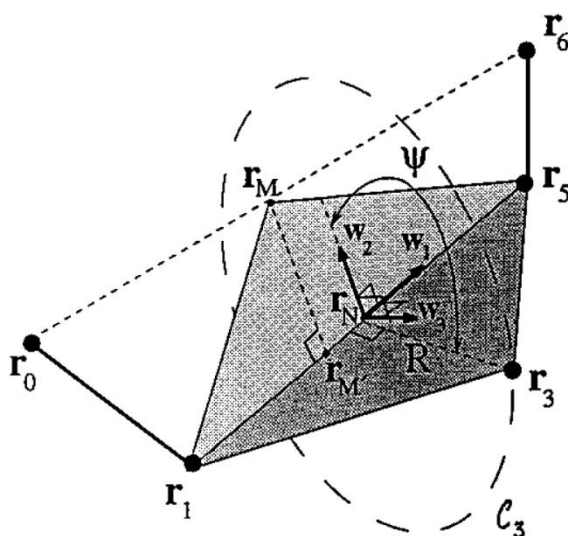


Figure A-5 Frame of reference for describing the central trimer atom position. The position  $r_3$  is expressed in the frame  $[w_1, w_2, w_3]$  with origin  $r_N$ , where  $r_N$  is the projection of  $r_3$  onto the  $(r_1, r_5)$  axis. Unit vector  $w_2$  is parallel to  $(r_M, r_M')$ , where  $r_M$  is the midpoint of  $(r_0, r_6)$  and  $r_M'$  is the projection of  $r_M$  onto the  $(r_1, r_5)$  axis. The position of  $r_3$  on its locus is defined by the dihedral angle  $\varphi$  between planes  $\{r_1, r_M, r_5\}$  and  $\{r_1, r_3, r_5\}$ . The locus of  $r_3$  is shown as the long-dashed circle  $C_3$ , centered at  $r_N$ , of radius  $R$ , lying in a plane perpendicular to  $(r_1, r_5)$ .

A locus for  $r_3$  is determined as follows: for fixed  $l_{13}$ ,  $r_3$  lies on the surface of a sphere of radius  $l_{13}$  centered at  $r_1$ . Similarly, for fixed  $l_{53}$  (because the  $l_4$ ,  $l_5$ ,  $\theta_4$  are fixed),  $r_3$  lies on the surface of a sphere of radius  $l_{53}$  centered at  $r_5$ . Therefore,  $r_3$  belongs to the intersection of two known spheres, i.e., on a circle  $C_3$  with its center on the line connecting  $r_1$  and  $r_5$  (figure A-5). The exact position of  $r_3$  on  $C_3$  is determined by one angular variable. Here, this is chosen as the dihedral angle  $\varphi$  between planes  $(r_3, r_1, r_5)$  and  $(r_M, r_1, r_5)$  with  $r_M = (r_0 + r_6)/2$  (see figure A-5). Requiring that  $r_2, r_3, r_4$  lie on  $C_2, C_3, C_4$ , respectively, amounts to an elimination of the six constraints from the nine equations in nine unknowns describing the trimer bridging problem. The three constraints remain, and could be used to determine three unknown angular variables  $\phi_R$ ,  $\phi_L$  and  $\varphi$ . Thus, the trimer bridging problem is reduced to the following general geometric problem: given three circles,  $C_2, C_3, C_4$  in space, determine one point on each circle  $r_2 \in C_2$ ,  $r_3 \in C_3$ , and  $r_4 \in C_4$ , such that the distances  $|r_3 - r_2|, |r_4 - r_3|, |r_2 - r_4|$  between the three points have prespecified values ( $l_2, l_3$  and  $\sqrt{l_3^2 + l_4^2 + 2l_3l_4 \cos \theta_3}$ , respectively).

Analytical expressions for  $r_2(\phi_L)$ ,  $r_3(\varphi)$ , and  $r_4(\phi_R)$  can be developed through the introduction of appropriate local coordinate frames.

To express  $r_2$  analytically in terms of  $\phi_L$ , we define a right-handed coordinate frame  $[u_1, u_2, u_3]$ , as shown in Figure A-4. In this figure,  $r_P$  is a projection of  $r_2$  onto the axis of bond 1 and  $r_2^0$  is a point of intersection of  $C_2$  with the plane  $(r_L, r_0, r_1)$ , corresponding to the position of  $r_2$  for which  $\phi_L = 0$ . The unit vectors  $u_1$  and  $u_2$  are directed along  $r_1 - r_0$  and  $r_2^0 - r_P$ , respectively.  $u_3$  is determined according to the right-handed rule

Similarly, to express  $r_4$  analytically in terms of  $\phi_R$ , we define a right-handed coordinate frame  $[v_1, v_2, v_3]$ , as shown in Figure A-4. Here,  $r_Q$  is the projection of  $r_4$  on the axis of bond 6.  $r_4^0$  is a point of intersection of  $C_4$  with the plane  $(r_5, r_6, r_R)$ , corresponding to  $\phi_R = 0$ , and the unit vectors  $v_1$  and  $v_2$  are directed along  $r_Q - r_5$  and  $r_4^0 - r_Q$ , respectively.

$C_3$ , the locus of  $r_3$  (figure A-5), is a circle of known radius  $R$  centered at  $r_N$ , where  $r_N$  is the projection of  $r_3$  onto the axis connecting  $r_1$  and  $r_5$ . A right handed local coordinate frame  $[w_1, w_2, w_3]$  is defined with origin at  $r_N$ , with  $w_1$  directed along  $r_5 - r_1$  and  $w_2$  lying in the plane  $(r_1, r_5, r_M)$  and pointing toward  $r_M$ .

With the above definitions, the analytical expressions for  $r_2, r_3, r_4$  in terms of  $\phi_L, \varphi, \phi_R$  become

$$r_2 = r_P + l_2 \sin \theta_1 \cos \phi_L u_2 + l_2 \sin \theta_1 \sin \phi_L u_3 \quad (\text{A-1})$$

$$r_3 = r_N + R \cos \varphi w_2 + R \sin \varphi w_3 \quad (\text{A-2})$$

$$r_4 = r_Q + l_5 \sin \theta_5 \cos \phi_R v_2 + l_5 \sin \theta_5 \sin \phi_R v_3 \quad (\text{A-3})$$

Where the unit vector  $u_i$ ,  $w_i$ , and  $v_i$ (see figure A-4) are calculated from the position vectors  $r_L$ ,  $r_0$ ,  $r_1$ ,  $r_5$ ,  $r_6$ ,  $r_R$  as

$$u_1 = \frac{r_1 - r_0}{l_1} \quad (\text{A-4})$$

$$u_2 = -\frac{l_1(r_L - r_0)}{|(r_L - r_0) \times (r_1 - r_0)|} + \frac{(r_L - r_0) \bullet (r_1 - r_0)}{|(r_L - r_0) \times (r_1 - r_0)|} \frac{r_1 - r_0}{l_1} \quad (\text{A-5})$$

$$u_3 = -\frac{(r_L - r_0) \times (r_1 - r_0)}{|(r_L - r_0) \times (r_1 - r_0)|} \quad (\text{A-6})$$

$$w_1 = \frac{r_5 - r_1}{|r_5 - r_1|} \quad (\text{A-7})$$

$$w_2 = \frac{|r_5 - r_1|}{|(r_M - r_1) \times (r_5 - r_1)|} (r_M - r_1) - \frac{(r_M - r_1) \bullet (r_5 - r_1)}{|(r_M - r_1) \times (r_5 - r_1)|} \frac{(r_5 - r_1)}{|r_5 - r_1|} \quad (\text{A-8})$$

$$w_3 = \frac{(r_5 - r_1) \times (r_M - r_1)}{|(r_M - r_1) \times (r_5 - r_1)|} \quad (\text{A-9})$$

$$v_1 = -\frac{r_6 - r_5}{l_6} \quad (\text{A-10})$$

$$v_2 = -\frac{l_6(r_R - r_6)}{|(r_R - r_6) \times (r_6 - r_5)|} + \frac{(r_R - r_6) \bullet (r_6 - r_5)}{|(r_R - r_6) \times (r_6 - r_5)|} \frac{(r_6 - r_5)}{l_6} \quad (\text{A-11})$$

$$v_3 = -\frac{(r_R - r_6) \times (r_6 - r_5)}{|(r_R - r_6) \times (r_6 - r_5)|} \quad (\text{A-12})$$

and the origins of the three coordinate frames are located at

$$r_p = r_1 + l_2 \cos \theta_1 \frac{(r_1 - r_0)}{l_1} \quad (\text{A-13})$$

$$r_N = \frac{r_1 + r_5}{2} + \frac{r_1 - r_5}{2} \left( \frac{|r_3 - r_5|^2 - |r_3 - r_1|^2}{|r_5 - r_1|^2} \right) \quad (\text{A-14})$$

$$r_Q = r_5 + l_5 \cos \theta_5 \frac{(r_5 - r_6)}{l_6} \quad (\text{A-15})$$

As mentioned in the text, the reference point  $r_M$  is defined as

$$r_M = \frac{r_6 + r_0}{2} \quad (\text{A-16})$$

The radius of  $C_3$ , the locus of  $r_3$ , is

$$R = |r_3 - r_1| \sqrt{1 - \left( \frac{|r_5 - r_1|^2 + |r_3 - r_1|^2 + |r_5 - r_3|^2}{2|r_3 - r_1||r_5 - r_1|} \right)^2} \quad (\text{A-17})$$

Where  $|r_3 - r_1| = \sqrt{l_2^2 + l_3^2 + 2l_2l_3 \cos \theta_2}$  and  $|r_5 - r_3| = \sqrt{l_4^2 + l_5^2 + 2l_4l_5 \cos \theta_4}$  have fixed values

Equations A-1, A-2, A-3 can be reduced to one equation in one unknown by applying the bond length and bond angle constraints of the middle trimer.

$$|r_3 - r_2|^2 = l_3^2 \quad (\text{A-18})$$

$$|r_4 - r_3|^2 = l_4^2 \quad (\text{A-19})$$

$$|r_4 - r_2|^2 = l_3^2 + l_4^2 + 2l_3l_4 \cos \theta_3 \quad (\text{A-20})$$

We define

$$a_2 = l_2 \sin \theta_1 \quad (\text{A-21})$$

$$a_4 = l_5 \sin \theta_5 \quad (\text{A-22})$$

Substituting equation A-1 into equation A-18 yields

$$a_L \omega_L^2 + b_L \omega_L + c_L = 0 \quad (\text{A-23})$$

Where

$$\omega_L = \tan(\phi_L / 2) \quad (\text{A-24})$$

$$a_L = (r_p - r_3)^2 + a_2^2 - l_2^3 - 2a_2 [(r_p - r_3) \bullet u_2] \quad (\text{A-25})$$

$$b_L = 4a_2 [(r_p - r_3) \bullet u_3] \quad (\text{A-26})$$

$$c_L = (r_p - r_3)^2 + a_2^2 - l_3^2 + 2a_2 [(r_p - r_3) \bullet u_2] \quad (\text{A-27})$$

The root equation is

$$\tan(\phi_L / 2) = \omega_L = \frac{-b_L \pm \sqrt{b_L^2 - 4a_L c_L}}{2a_L} \quad (\text{A-28})$$

Equation A-28 is quadratic in  $\omega_L$ . For given  $r_3(\varphi)$ , it can have two, one(degenerate), or zero real roots. Roots obtained through equation A-28 will be symbolized as  $\phi_L(r_3(\varphi))$ , substitution of such a root into equation A-1, gives  $r_2[\phi_L(r_3(\varphi))] = r_2(\varphi)$ .

Likewise, substituting equation A-3 into equation A-19 yields

$$a_R \omega_R^2 + b_R \omega_R + c_R = 0 \quad (\text{A-29})$$

Where

$$\omega_R = \tan(\phi_R / 2) \quad (\text{A-30})$$

$$a_R = (r_Q - r_3)^2 + a_4^2 - l_4^2 - 2a_4 [(r_Q - r_3) \bullet v_2] \quad (\text{A-31})$$

$$b_R = 4a_4 [(r_Q - r_3) \bullet v_3] \quad (\text{A-32})$$

$$c_R = (r_Q - r_3)^2 + a_4^2 - l_4^2 + 2a_4 [(r_Q - r_3) \bullet v_2] \quad (\text{A-33})$$

The root equation is

$$\tan(\phi_R / 2) = \omega_R = \frac{-b_R \pm \sqrt{b_R^2 - 4a_R c_R}}{2a_R} \quad (\text{A-34})$$

Equation A-34 is quadratic in  $\omega_R$ . For given  $r_3(\varphi)$ , it can have two, one(degenerate), or zero real roots. Roots obtained through equation A-34 will be symbolized as  $\phi_R(r_3(\varphi))$ , substitution of such a root into equation A-3, gives  $r_4[\phi_R(r_3(\varphi))] = r_4(\varphi)$ .

Substituting the solution of equation A-23 and equation A-24 into the third constraint equation A-20 yields the function

$$F(\varphi) = |r_4(\varphi) - r_2(\varphi)|^2 - l_3^2 - l_4^2 - 2l_3l_4 \cos \theta_3 \quad (\text{A-35})$$

$\varphi$  is a solution to the bridging problem when  $F(\varphi) = 0$ .

In general, this function is highly nonlinear and it may have up to four branches due to equation A-23 and equation A-24 may contribute two roots for  $\phi_R$  and  $\phi_L$ . Therefore, it may have many different solutions. In another words, given two dimmers in space, there would be many ways to connect them with a trimer, such that the resulting heptamer has prescribed bond lengths and angles.

In order to obtaining these solutions, a numerical technique is employed to identify all the roots  $\varphi$  of the function  $F(\varphi) = 0$ . Before starting the numerical analysis, the feasibility conditions of the trimer bridging is examined. The simplest among them is based on the fact that  $r_3$  lies on the intersection of two spheres, one centered at  $r_1$  with radius  $r_3 - r_1$  and one centered at  $r_5$  with radius  $r_3 - r_5$ . For the existence of such an intersection

$$|r_5 - r_1| \leq |r_3 - r_1| + |r_3 - r_5| \quad (\text{A-36})$$

If the dimmers  $(r_0, r_1)$  and  $(r_5, r_6)$  form a bridging gap which violates equation A-36.  $F(\varphi)$  does not exist for any  $\varphi$ .

Another feasibility conditions of the trimer bridging problem are derived from the discriminants of the quadratic equations from which  $\phi_R(r_3(\varphi))$  and  $\phi_L(r_3(\varphi))$  are determined; the discriminants must be non-negative for real geometric solutions to exist.

After checking the feasibility, a “brute-force” sweep through the entire  $\varphi$  space  $(-\pi, \pi)$  is performed: in this work the entire  $\varphi$  space  $(-\pi, \pi)$  is divided into 720 small intervals. The values of both of ends of every interval  $(a, b)$  are put into the function  $F(\varphi)$ , we get results  $(F(a), F(b))$ . A second sweep is performed with the mesh displaced by a differential amount, allowing for a finite difference estimation of the gradient  $(F'(a), F'(b))$ . The value of  $F(\varphi)$  and sign of the gradient at each interval ends are used to identify intervals that may contain a root. Three different situations may exist:

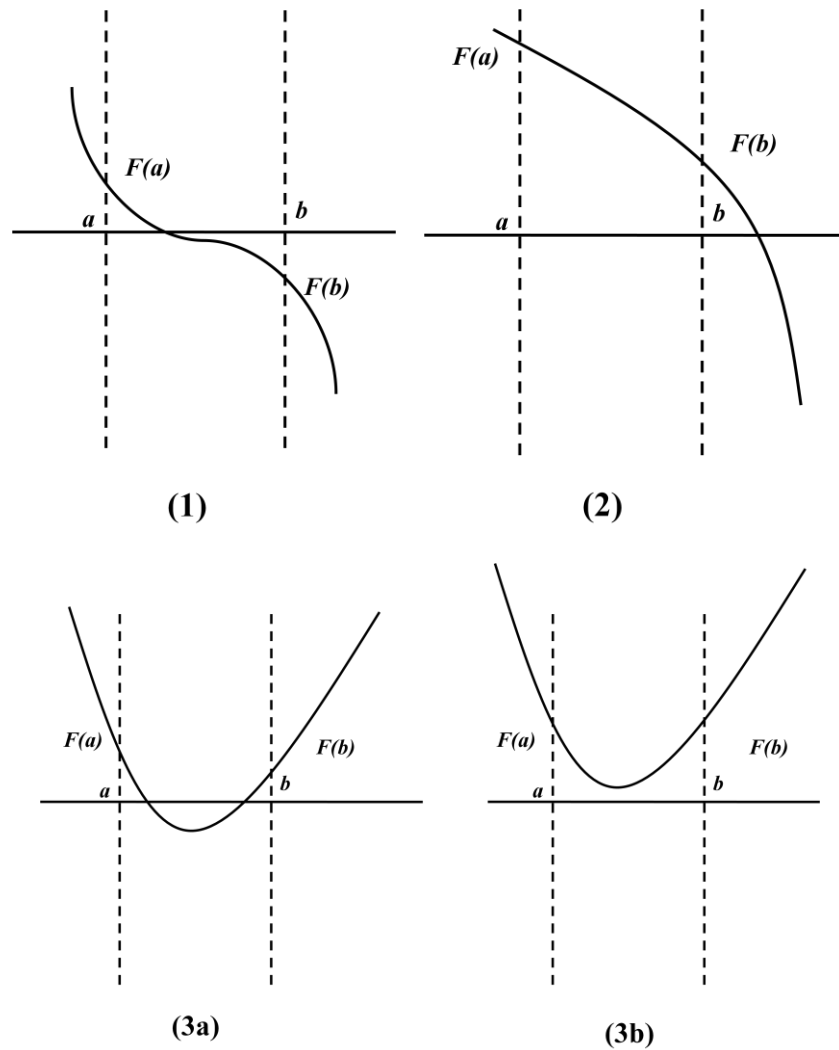


Figure A-6. Three different situations of the value of  $F(\varphi)$  and sign of the gradient at each interval ends are used to identify intervals that may contain a root.

If  $F(a) * F(b) \leq 0$ , that is the situation 1 in figure A-6 (1) which have root

If  $F(a) * F(b) > 0$  and  $F'(a) * F'(b) > 0$ , that is the situation 2 in figure A-6 (2) which have no root

If  $F(a) * F(b) > 0$  and  $F'(a) * F'(b) < 0$ , that might be the situation 3a or 3b in figure A-6 which may contain more than one root. Under this circumstance, this interval is further divided into 10 smaller intervals and repeat above procedure until match situation 1 and 2.

For the intervals which may contain root, they are searched exhaustively using a weighted bisection method. The bisection proceeds until a tolerance limit is reached.

## Appendix B - End-reptation (EP) algorithm

This appendix presents details of the end-reptation MC move algorithm

The end-reptation geometric problem to be analyzed is depicted in Figure B-1. In the end-reptation move, bead  $m$  is excised from the *Chain 1*, and attach to another *Chain 2* end, meanwhile keep the same bond length and bond angle, but chose a random torsional angle, therefore, if we consider bead  $m$  as  $r_2$ , bead  $p$  as  $r_1$ , bead  $p$ 's another two neighbour  $r_0$  and  $r_L$ . It is the same situation to determine the position of  $r_2$  as in end-bridging move.

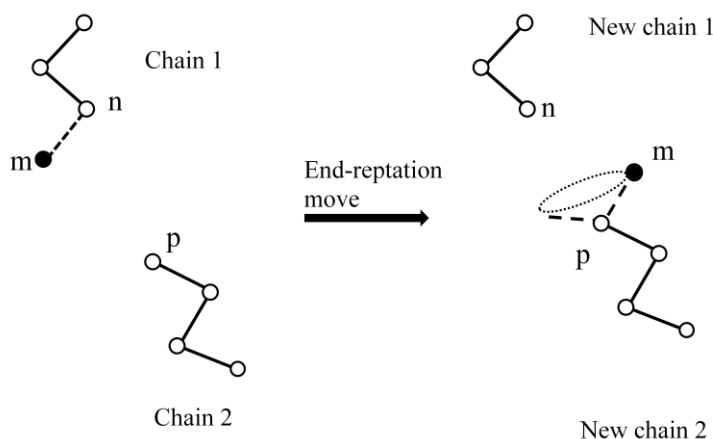


Figure B-1. End- reptation MC move (a end bead ( $m$ ) of a chain tail is excised, and then reconfigured to connect another tail branch).

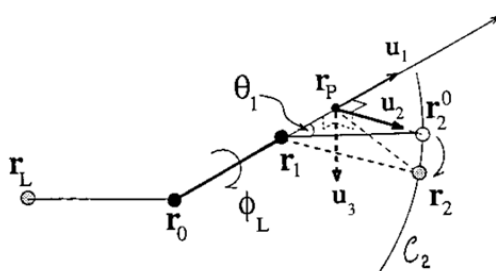


Figure B-2 The position  $r_2$  is expressed in frame  $[u_1, u_2, u_3]$  with origin  $r_p$ . The position  $r_4$  is expressed in frame  $[v_1, v_2, v_3]$  with origin  $r_p$ . Angles  $\theta_1$  are the bond angle supplements at vertices  $r_1$ , respectively. All solid straight lines in the figure are coplanar.

Again, to express  $r_2$  analytically in terms of a random  $\phi_L$ , we define a right-handed coordinate frame  $[u_1, u_2, u_3]$ , as shown in Figure B-2. In this figure,  $r_p$  is a projection of  $r_2$  onto the axis of *bond 1* and  $r_2^0$  is a point of intersection of  $C_2$  with the plane  $(r_L, r_0, r_1)$ , corresponding to the position of  $r_2$  for which  $\phi_L = 0$ . The unit vectors  $u_1$  and  $u_2$  are directed along  $r_1 - r_0$  and  $r_2^0 - r_p$ , respectively.  $u_3$  is determined according to the right-handed rule

$$r_2 = r_p + l_2 \sin \theta_1 \cos \phi_L u_2 + l_2 \sin \theta_1 \sin \phi_L u_3 \quad (\text{B-1})$$

$$u_1 = \frac{r_1 - r_0}{l_1} \quad (\text{B-2})$$

$$u_2 = -\frac{l_1(r_L - r_0)}{|(r_L - r_0) \times (r_1 - r_0)|} + \frac{(r_L - r_0) \bullet (r_1 - r_0)}{|(r_L - r_0) \times (r_1 - r_0)|} \frac{r_1 - r_0}{l_1} \quad (\text{B-3})$$

$$u_3 = -\frac{(r_L - r_0) \times (r_1 - r_0)}{|(r_L - r_0) \times (r_1 - r_0)|} \quad (\text{B-4})$$

## Appendix C – Linear regression method

This appendix presents details of linear regression method

In linear regression, the model specification is that the dependent variable,  $y_i$  is a linear combination of the parameters (but need not be linear in the independent variables). For example, in simple linear regression for  $n$  data points there is one independent variable:  $x_i$ , and two parameters,  $\beta_0$  and  $\beta_1$ :

$$\text{straight line: } y_i = \beta_0 + \beta_1 x_i + \varepsilon_i \quad i = 1, \dots, n. \quad (\text{C-1})$$

In multiple linear regression, there are several independent variables or functions of independent variables. For example, adding a term in  $x_i^2$  to the preceding regression gives:

$$\text{parabola: } y_i = \beta_0 + \beta_1 x_i + \beta_2 x_i^2 + \varepsilon_i, \quad i = 1, \dots, n. \quad (\text{C-2})$$

This is still linear regression; although the expression on the right hand side is quadratic in the independent variable  $x_i$ , it is linear in the parameters  $\beta_0$ ,  $\beta_1$  and  $\beta_2$ .

In both cases,  $\varepsilon_i$  is an error term and the subscript  $i$  indexes a particular observation. Given a random sample from the population, we estimate the population parameters and obtain the sample linear regression model:

$$y_i = \hat{\beta}_0 + \hat{\beta}_1 x_i + e_i \quad (\text{C-3})$$

Where  $\hat{\beta}_0, \hat{\beta}_1$  read “ $\beta$  hat”, denotes the predicted value. The term  $e_i$  is the residual.

$$e_i = y_i - \hat{y}_i \quad (\text{C-4})$$

One method of estimation is ordinary least squares. This method obtains parameter estimates that minimize the sum of squared residuals,  $SSE$ :

$$SSE = \sum_{i=1}^N e_i^2 \quad (\text{C-5})$$

Minimization of this function results in a set of normal equations, a set of simultaneous linear equations in the parameters, which are solved to yield the parameter estimators,  $\hat{\beta}_0, \hat{\beta}_1$ .

In the case of simple regression, the formulas for the least squares estimates are

$$\hat{\beta}_1 = \frac{\sum(x_i - \bar{x})(y_i - \bar{y})}{\sum(x_i - \bar{x})^2} \quad (\text{C-6})$$

$$\hat{\beta}_0 = \bar{y} - \hat{\beta}_1 \bar{x} \quad (\text{C-7})$$

Where  $\bar{x}$  is the mean (average) of the  $x$  values and  $\bar{y}$  is the mean of the  $y$  values. The derivation of these formulas is omitted here. Under the assumption that the population error term has a constant variance, the estimate of that variance is given by:

$$\hat{\sigma}_\varepsilon^2 = \frac{SSE}{N - 2} \quad (\text{C-8})$$

This is called the mean square error (MSE) of the regression. The standard errors of the parameter estimates are given by

$$\hat{\sigma}_{\beta_0} = \hat{\sigma}_\varepsilon \sqrt{\frac{1}{N} + \frac{\bar{x}^2}{\sum(x_i - \bar{x})^2}} \quad (\text{C-9})$$

$$\hat{\sigma}_{\beta_1} = \hat{\sigma}_\varepsilon \sqrt{\frac{1}{\sum(x_i - \bar{x})^2}} \quad (\text{C-10})$$

Under the further assumption that the population error term is normally distributed, the researcher can use these estimated standard errors to create confidence intervals and conduct hypothesis tests about the population parameters.